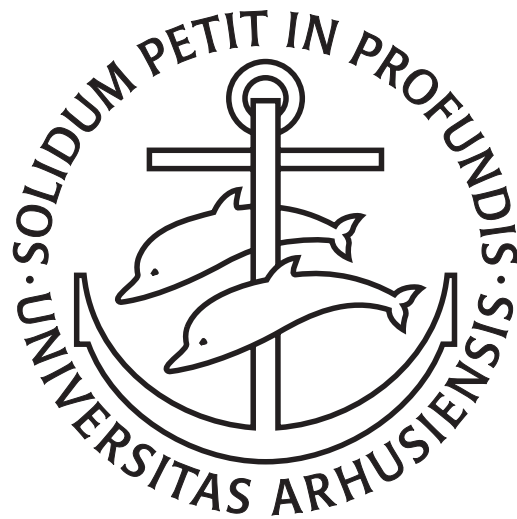


Electron Scattering on Positive and Negative Ions Studied in Heavy-Ion Storage Rings



Klaus Seiersen

Department of Physics and Astronomy
University of Aarhus, Denmark

September 2003

Preface

This thesis has been submitted to the Faculty of Science at the University of Aarhus, Denmark, in order to fulfill the requirements for the PhD degree. The work presented in this thesis has been carried out at the Department of Physics and Astronomy at the University of Aarhus under the supervision of Dr. Lars H. Andersen. The thesis describes experimental studies of electron-ion collisions, which have been performed at the heavy-ion storage ring ASTRID and the electrostatic storage ring ELISA, both at the University of Aarhus. The experiments have been performed during my time in the research group, which I joined in August 1999. My work was funded by The Faculty of Science, the Aarhus Center for Atomic Physics (ACAP) and the IHP Program of the EU under contract No. HPRN CT-2000-00142.

The present work has been published in the articles found in the list of publications on page iii. Furthermore, I have participated in the following schools and conferences:

- *EU Network meetings* in Leiden, The Netherlands (November 2000), in Prague, The Czech Republic (October 2001) and in Louvain-la-Neuve, Belgium (October 2002).
- *European Conference on Dynamics of Molecular Collisions* (MOLEC) XIII in Jerusalem, Israel (September 2000) and XIV in Istanbul, Turkey (September 2002).
- *The Vth Femtochemistry Conference* in Toledo, Spain (September 2001).
- *Euro Summer School: Dynamics of Molecular Collisions*, Rehovot, Israel (September 2000).
- *Annual meetings of the Danish Physical Society* in June 2000 and May 2002 (poster prize recipient).
- *Nordic summer school on Spectroscopy and Collision Dynamics with Highly Charged Ions*, Abisko, Sweden (May 2000).
- *PhD Winter School in Physics*, Sandbjerg, Denmark (January 2000).

Acknowledgments

During my time as a PhD student I have enjoyed the help, support and company of a great number of people.

First of all, I would like to express my gratitude to my supervisor, Lars H. Andersen. He has taught me a very big part of what I today know about experimental physics, and his clear and concise explanations have made it easy to get acquainted with new subjects. Also, his ability to use criticism (irrespective of how righteous it might be) in the most constructive way has formed the basis of the good relationship we have today.

Marie J. Jensen was a PhD student and C. P. Safvan was a Postdoc in the group when I joined in 1999, and they have both taught me a lot about the experiments in the group. They have been a great joy to work with, and Marie in particular has been a good friend both in and outside the lab. Henrik Bluhme has also been a great friend since my first years at the university. As a lab instructor in 1995, he introduced me to my first physics experiments at the university, and in 2002 Henrik joined our research group as a Postdoc. I have, however, had some problems convincing him that he is not the king of the lab, and this task will probably take some effort yet before success is achieved. Helle Krogh, Jytte Bak, Annette Svendsen, Severine Boyé and Iben Bloch Nielsen are present and former members of the group who have contributed to the good atmosphere of the work place.

Steen Brøndsted Nielsen has also been a pleasure to have in the group, and he is thanked for fruitful discussions on molecular structure.

During my PhD study I have chosen not to visit a foreign laboratory for an extended period of time. Instead, I have had the joy of working with visiting scientists at the ASTRID storage ring. Both Oded Heber from the Weizmann Institute of Science in Israel and the research group of Brian Mitchell from the Université de Rennes in France have been frequent visitors in Århus. Also, we have had several visits from *e.g.* the CRYRING facility in Stockholm, and these have resulted in several new friendships.

I would like to thank the staff at ASTRID for their invaluable assistance during the experiments. Niels Hertel, Søren Pape Møller and Jørgen S. Nielsen have all contributed with many hours in the control room, often during evenings and weekends. Also, Ulrik V. Pedersen is thanked for his tireless support during ELISA experiments. His skillful and pleasant company has been a significant asset to us. Finn Abildskov has been a great help to us, especially during absolute ion current measurements at ASTRID, where we more than once have required his services beyond normal working hours.

No experimental physicist can do without technical construction and workshop assistance, and in that respect I would like to acknowledge the help of Kåre Iversen, Karsten Rasmussen, Jens Vestergaard, Robert Steensgaard, the entire workshop and the electronics department. Also, Egon Jans has been a great help in preparing ion sources. You have all been appreciated company both in and outside the laboratory.

Annette Skovgaard is gratefully acknowledged for proofreading English manuscripts prepared during my time at the university. Also, a big thanks to Henrik, Henrik and Niels, who helped proofread parts of this thesis.

During my eight years at the Department of Physics and Astronomy I have had the pleasure of being at a fabulous work place, where plenty of social events ranging from parties, picnics, Christmas dinners and the Friday Bar to quizzes, running and bowling supplement the professional environment in an excellent way. I have met many great people whom have become some of my best friends. Thank you all - you know who you are.

Finally, I would like to acknowledge financial support from the Danish National Research Foundation through ACAP and from the EU Network of which we are members.

Klaus Seiersen
Århus, September 17 2003

List of publications

The present work is based on the following articles:

- I. K. Seiersen, J. Bak, H. Bluhme, M. J. Jensen, S. B. Nielsen and L. H. Andersen: “*Electron-impact detachment of O_3^- , NO_3^- and SO_2^- ions*”, Phys. Chem. Chem. Phys. **5**, 4814 (2003).
- II. K. Seiersen, A. Al-Khalili, O. Heber, M. J. Jensen, I. B. Nielsen, H. B. Pedersen, C. P. Safvan and L. H. Andersen: “*Dissociative recombination of the cation and dication of CO_2* ”, Phys. Rev. A **68**, 022708 (2003).
- III. K. Seiersen, O. Heber, M. J. Jensen, C. P. Safvan and L. H. Andersen: “*Dissociative recombination of dications*”, J. Chem. Phys. **119**, 839 (2003).
- IV. L. H. Andersen, J. Bak, S. Boyé, M. Clausen, M. Hovgaard, M. J. Jensen, A. Lapierre and K. Seiersen: “*Resonant and nonresonant electron impact detachment of CN^- and BO^-* ”, J. Chem. Phys. **115**, 3566 (2001).
- V. L. H. Andersen, R. Bilodeau, M. J. Jensen, S. B. Nielsen, C. P. Safvan and K. Seiersen: “*Coulomb and centrifugal barrier bound dianion resonances of NO_2^-* ”, J. Chem. Phys. **114**, 147 (2001).

Moreover, I have contributed to the following papers:

- VI. O. Witasse, O. Dutuit, J. Lilensten, R. Thissen, J. Zabka, C. Alcaraz, P.-L. Blelly, S. W. Bougher, S. Engel, L. H. Andersen and K. Seiersen: “*Correction to ‘Prediction of a CO_2^+ layer in the atmosphere of Mars’*”, Geophys. Res. Lett. **30**, 1360 (2003).
- VII. J. B. A. Mitchell, C. Rebrion-Rowe, J. L. Le Garrec, G. Angelova, H. Bluhme, K. Seiersen and L. H. Andersen: “*Branching ratios for the dissociative recombination of hydrocarbon ions. I: The cases of $C_4H_9^+$ and $C_4H_5^+$* ”, Int. J. Mass Spec. **227**, 273 (2003).
- VIII. O. Witasse, O. Dutuit, J. Lilensten, R. Thissen, J. Zabka, C. Alcaraz, P.-L. Blelly, S. W. Bougher, S. Engel, L. H. Andersen and K. Seiersen: “*Prediction of a CO_2^+ layer in the atmosphere of Mars*”, Geophys. Res. Lett. **29**, 1263 (2002).
- IX. M. J. Jensen, H. B. Pedersen, C. P. Safvan, K. Seiersen, X. Urbain and L. H. Andersen: “*Dissociative recombination and excitation of H_3^+* ”, Phys. Rev. A **63**, 052701 (2001).
- X. M. J. Jensen, R. C. Bilodeau, C. P. Safvan, K. Seiersen, L. H. Andersen, H. B. Pedersen and O. Heber: “*Dissociative recombination of H_3O^+ , HD_2O^+ , and D_3O^+* ”, Astrophys. J. **543**, 764 (2000).

Outline of thesis

The thesis is organized as follows:

- **Chapter 1**

This chapter is a general introduction to both the motivation that binds the present work together and to science in general.

- **Chapter 2**

This chapter deals with the experimental equipment and techniques that are applied in the experiments presented in this thesis. Specifically, the two storage rings ASTRID and ELISA and their respective electron targets are presented. Moreover, the sources for the production of the studied ions and the experimental methods involved in measurements with the described apparatus are described.

- **Chapter 3**

As a PhD student I have worked with electron scattering on negatively charged ions. We have measured electron impact detachment of several both atomic and molecular ions, and the results from these experiments are presented in this chapter.

- **Chapter 4**

This chapter deals with experiments on doubly-charged positive ions that have been performed during my time at the department. We have measured dissociative recombination and dissociative excitation rate coefficients for three different ions and compared them to rate coefficients of the corresponding singly-charged ions, one of which is also presented in this chapter.

- **Chapter 5**

The electron target ETRAP for the storage ring ELISA has been tested and installed into the ring during my time in the group. This chapter presents some of the first test results and the first experimental measurement using the apparatus.

- **Chapter 6**

This chapter gives a summary of the presented work.

- **Chapter 7**

This chapter is a Danish summary for non-scientist.

- **Appendices**

Several appendices have been included at the end of the thesis. In these, a number of the theoretical expressions used throughout the thesis are derived. This is done in appendices in an attempt to let the reader keep as much of an overview of the work as possible. References between the equations and the relevant appendices are clearly marked in the thesis. Moreover, one appendix contains a list of abbreviations used in this thesis.

The outline is also sketched graphically in Fig. 1.

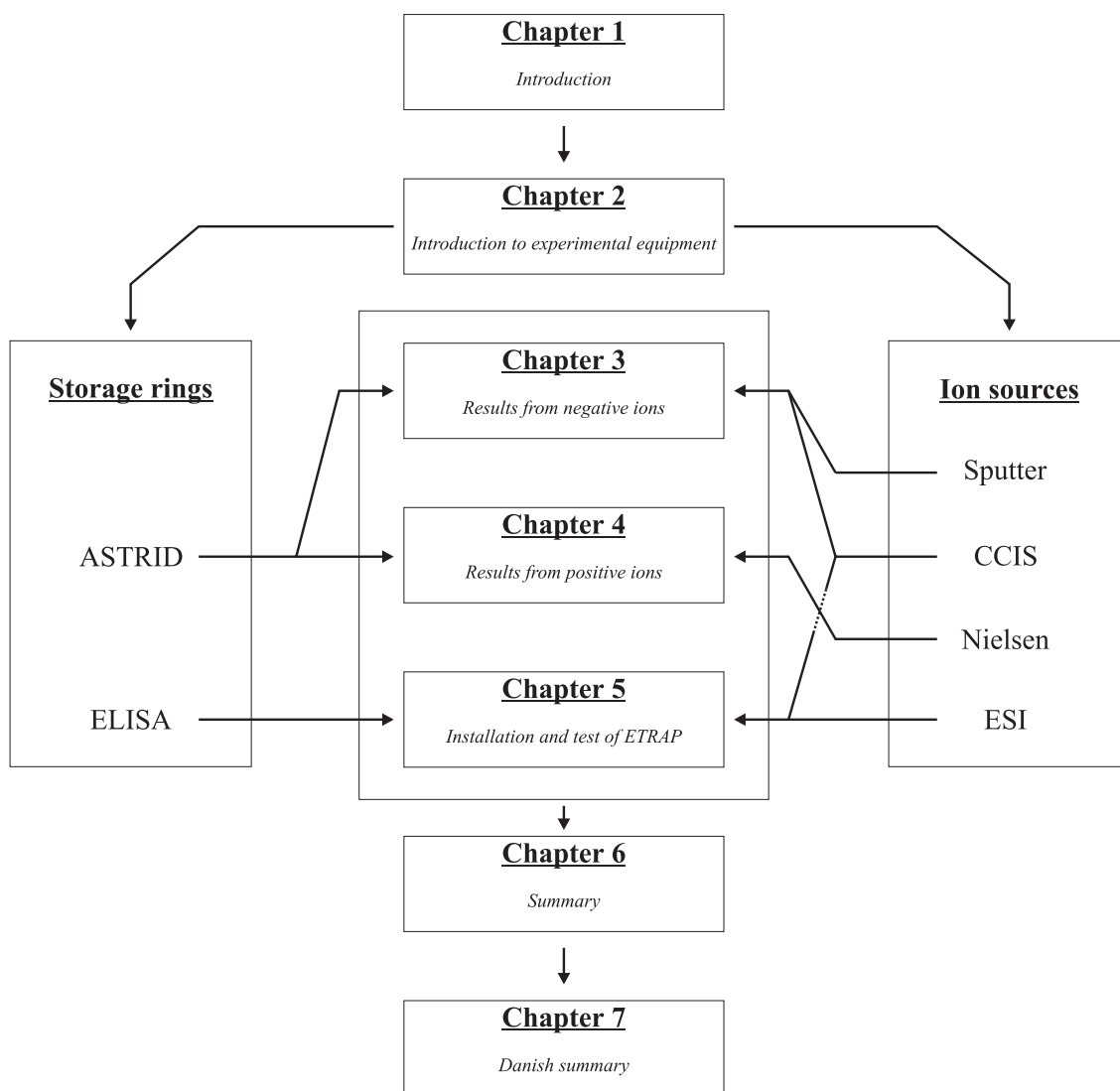


Figure 1: Schematic outline of the thesis.

Contents

1	Introduction	1
2	Experimental equipment and techniques	3
2.1	Introduction	3
2.2	The ASTRID heavy-ion storage ring	7
2.2.1	The storage ring	7
2.2.2	The electron target	8
2.2.3	Experimental procedures	19
2.3	The ELISA electrostatic storage ring	21
2.3.1	The storage ring	21
2.3.2	The electron target	24
2.3.3	Experimental procedures	26
2.4	Ion sources	27
2.4.1	The Aarhus negative ion sputter source	27
2.4.2	Cold cathode ion source	28
2.4.3	Nielsen type ion source	31
2.4.4	Electrospray ionization	31
2.4.5	Comparison and diagnostics	33
2.5	Conclusion	36
3	Electron scattering on negative ions	37
3.1	Introduction	37
3.1.1	General introduction	37
3.1.2	Historical overview	38
3.2	Theoretical overview	39
3.3	Experimental results	43
3.3.1	S^- and Cl^-	43
3.3.2	CN^- and BO^-	45
3.3.3	O_3^-	47
3.3.4	NO_2^-	50
3.3.5	NO_3^-	51
3.3.6	SO_2^-	53
3.4	Comparison of anion cross-sections	54
3.5	Conclusion	54
4	Electron scattering on positive ions	57
4.1	Introduction	57
4.1.1	General introduction	57

4.1.2	Historical overview	59
4.2	Theoretical overview	60
4.3	Experimental results	63
4.3.1	CO_2^+ and CO_2^{2+}	63
4.3.2	N_2^{2+}	68
4.3.3	CO^{2+}	70
4.3.4	Comparison of monocation and dication results	72
4.4	Conclusion	72
5	Installation and test of ETRAP	75
5.1	Introduction	75
5.1.1	General introduction	75
5.1.2	Historical overview	76
5.2	The electron target	77
5.3	Results	79
5.4	Conclusion	82
6	Summary	85
7	Dansk resumé	87
A	Space charge potential	91
B	Toroid correction	95
B.1	The relative energy in the toroid regions	95
C	Rate coefficients	97
C.1	The absolute rate coefficient	97
C.2	The thermal rate coefficient	98
D	List of abbreviations	99

Chapter 1

Introduction

We have probably all experienced the perfect idyll of standing on the seashore enjoying the Sun setting below the distant horizon while rays of sunlight reflect in the soft waves of the surface. What we rarely consider is the fact that we are not only standing on the shore of an ocean, we are also standing on the bottom of an ocean; not an ocean of water, but a vast ocean of oxygen and nitrogen - the atmosphere of Earth!

And just as the light from the Sun reflects in the surface of the water, so it interacts with the upper atmosphere, continuously ionizing the atomic and molecular constituents of the air, whereby a plasma of positive and negative ions mixed together with free electrons is created. Within this plasma, frequent electron scattering processes occur, reactions where the free electrons either recombine with positive ions that are subsequently dissociated, or induce electron detachment and sometimes dissociation of negative ions. Consequently, the electron-ion processes control both the charge density and the chemical composition of the upper atmosphere.

Scientists have the privilege of probing the frontier of human knowledge in a grand battle against the unknown. Some are motivated by a specific problem of practical (and perhaps economic) relevance, while many others have nothing but a fundamental urge to seek out knowledge of the world in which we live.

"My goal is simple. It is complete understanding of the universe, why it is as it is and why it exists at all." Stephen William Hawking.

Science is both an art and a craft. It is a method of understanding the beautiful combination of simplicity and complexity of the Universe, and it is a tool for wresting the deepest secrets of Nature using more and more sophisticated experimental equipment and techniques together with advanced theoretical insight.

"Equipped with his five senses, man explores the universe around him and calls the adventure science." Edwin Powell Hubble.

Science is accumulative: our knowledge builds on results from millenia of exploring our surroundings. In the words of Isaac Asimov, "*there is not a discovery in science, however revolutionary, however sparkling with insight, that does not arise out of what went before*", or to quote another Isaac,

"If I have seen further than others, it is because I have stood on the shoulders of giants." Sir Isaac Newton.

This work is fundamental research, work that is expected to be studied and used in different situations by scientist in the future, scientists who wish to understand and model the world in which we live. The work explores what happens, when positive and negative molecular ions collide with electrons of low energy. What are the reaction cross-sections, and do the molecules break up after the collisions? If so, which channels are open and what are their branching ratios? The work is relevant to a vast number of plasmas, from combustion science and fusion plasma through the upper atmospheres of Earth and other planets to the comas of comets and the chemistry of interstellar matter of outer space.

Study of molecular structure and dynamics is also of much more fundamental importance. Experiments are used as a test of theoretical models, and the combined experimental and theoretical knowledge will in the future be applied to molecules of ever increasing complexities. Biophysics is now a rapidly growing research subject, and physicists are beginning to probe the border between gas-phase and solvation, and even biomolecules themselves are becoming the focus of experiments.

This picture is sketched in Fig. 1.1, which also includes examples of ions mentioned in the present work. Traditionally, physicists have concentrated on the upper left area, the gas-phase ions, chemists on the lower right solvated species, and molecular biologists on the upper right *in vitro* biomolecules, systems of increasing order of complexity.

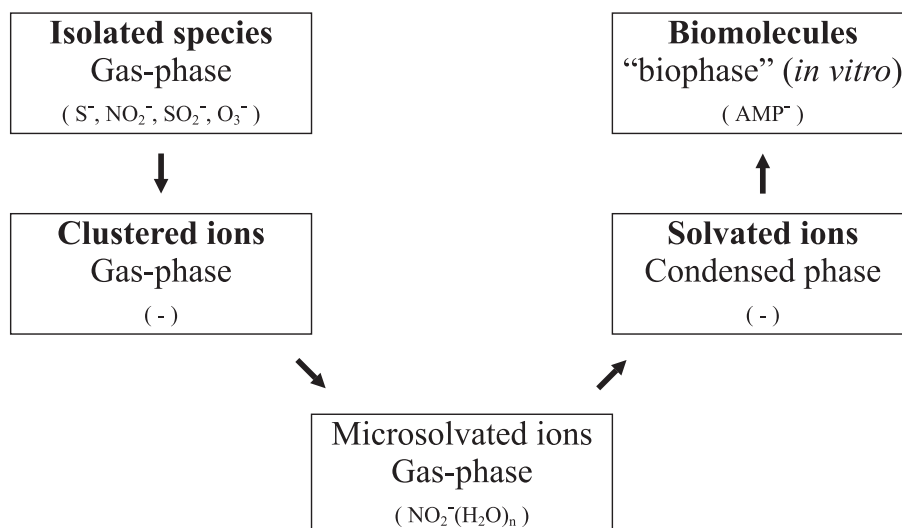


Figure 1.1: The road towards complexity.

The present work studies atomic, diatomic and small polyatomic molecules in the gas-phase, i.e. the upper left area of Fig. 1.1. In chapter 5, the first steps towards electron scattering experiments on biomolecules using storage rings are presented. While writing this, my colleagues in our research group have taken these experiments much further, in reality opening up a new research field. We have thus bridged the gap from studying the simplest of all ionic systems to some of the most complex systems constituting the basis of life:

”A physicist is just an atom’s way of looking at itself.” Niels Bohr.

Chapter 2

Experimental equipment and techniques

This chapter describes the experimental equipment and the experimental techniques, which form the basis of the present work. Initially, the two Danish storage rings ASTRID and ELISA are presented, and the experimental procedures involved during measurements with this equipment are described. A section about ion production concludes the chapter.

2.1 Introduction

Our knowledge about Nature and the universe in which we live has always come from experiments. The young child learning about the world does it through experiments; touching, shaking, biting, pulling, any object within reach to wrest it of its secrets. The tools of the experimental physicist is quite more advanced, often including expensive apparatus of very high complexity. Our knowledge about a given problem will typically increase with the development of new experimental techniques, and *the experiment* is thus of the utmost importance to the accumulated knowledge of mankind.

In this thesis, I will present experimental measurements of electron-ion collisions, particularly the reactions of dissociative recombination (DR) of positive ions and electron-impact detachment of negative ions. The apparatus employed in these experiments, *i.e.* the ion sources, accelerator systems and electron targets, is presented in this section. First, an overview of the techniques applied in recombination studies is presented, and this is followed by a technical description of the equipment used in this work.

Afterglow

One of the first methods used in studies of charged atomic and molecular ions was the afterglow technique, which has been under continuous development since the late 1920's [1]. Afterglow studies the decay of a plasma by monitoring charge densities and/or emitted photons as a function of time after the creation of the plasma and thereby allowing recombination rate coefficients to be extracted. The first laboratory measurements of dissociative recombination were made in 1949 by Biondi and Brown [2], who placed a volume of gas in a quartz container inside a microwave cavity. A microwave pulse ionized the gas, and the density of electrons was then monitored as a function of time in the decaying plasma. Early afterglow experiments are reviewed in Ref. [3].

Different techniques have been applied to monitor the plasma decay. Initially, Biondi and Brown measured the change in charge density by measuring the changing resonance frequency of the microwave cavity that enclosed the plasma. Other experiments measure the electron and ion densities in the plasma by using a small conducting probe in the plasma (called a Langmuir probe) and a mass spectrometer, respectively. The microwave technique provides an average electron concentration in the confined plasma, while a Langmuir probe yields an absolute electron density at a point in the plasma. Neglecting diffusion loss of plasma charges, the latter can be used directly to determine recombination coefficients.

Contrary to the first *stationary afterglow* experiments, later experiments used the *flowing afterglow* technique, where the plasma drifts along a neutral buffer gas down a drift tube. The charge densities are then measured using a movable Langmuir probe and a mass spectrometer, and this is done as a function of position, *i.e.* as a function of time. The widely used abbreviation FALP is used for flowing afterglow in combination with a Langmuir probe (see *e.g.* Ref. [4]). Other experiments have in addition utilized a VUV spectrometer to identify neutral fragments produced by plasma processes, thereby making extraction of branching ratios from the reactions possible.

Plasma afterglow experiments are generally rather complicated since they involve interacting plasmas and buffer gasses, which may interfere with the reaction of interest through various different reactions. The procedure of extracting pure DR data relies on knowledge of all other reactions occurring in the experiment. However, the afterglow glow technique is still today employed in many laboratories, and later in this thesis results of the present work will be compared to both stationary and flowing afterglow measurements.

Crossed and merged beams

The afterglow techniques measure reaction rates, but if one wants to measure cross-sections as a function of collision energy, well-defined beams of electrons and ions must be used. It is probably the appearance of theoretical predictions of cross-sections rather than rate coefficients that appealed to experimentalists from the atomic physics community. Experimental development accelerated, and the first experiments of this *crossed-beams* type were particle-impact ionization experiments, where a beam of *e.g.* electrons or ions were directed into a chamber containing a volume of gas, and in later experiments the chamber was replaced by a collimated gas jet. Soon experiments with crossed ion-ion beams and ion-electron beams were initiated, a development that leaped forward in the 1950's [5, 6].

The crossed-beams setup has several advantages over the afterglow technique. Afterglow experiments suffers from the fact that the complex plasma may contain several both atomic and molecular ions, but the application of a mass-selected ion beam solved this problem. Moreover, by using beams the reactant particle densities can be measured, and the products can be easily detected.

Crossed-beams experiments have often been implemented using two perpendicular beams, but several experimentalists have also used inclined beams. A further development of this is the *merged-beams* technique, where the two beams are actually overlapping on a common axis and propagating in the same direction. Though the first attempt to conduct a merged-beams¹ experiment was published in 1929 [7], the first successful applications

¹The technique was also called the *superimposed beams* or the *overtaking beams* technique in the beginning.

of the technique took place in the 1960's and 1970's [8, 9, 10].

The principal advantage of the merged-beams setup over the crossed-beams technique is the possibility of studying electron-ion collisions near 0 eV collision energies. The relative impact energy in electron-ion collisions is determined by the relative velocity between the two beams. In the merged-beams setup, one can achieve zero relative energy by combining parallel beams of equal velocities, while there in the crossed-beams setup always will be a non-zero velocity component. Moreover, the merged-beams setup allows for a long interaction region, which can yield a larger signal from low-intensity beams, and the possibility of using high ion beam energies makes control and detection of particles easy. The merged-beams technique is reviewed in Ref. [11].

Storage rings

A storage ring is a device in which a beam of charged particles is confined in a vacuum system by means of magnetic and/or electric fields. Storage rings were initially developed for storage of high-energy particles intended for particle physics experiments, and these rings had circumferences from about 100 meters to several kilometers. In the last 15 to 20 years storage rings have also been introduced to atomic physics and intermediate-energy physics with great success, and especially the combination of storage rings and the merged-beams technique has proven quite successful.

There are many advantages to this marriage of experimental techniques. The long storage time allows for beam cooling, since ions are typically stored for several seconds before measuring commences, and radiatively active ions will thus have time to decay to lower degrees of excitation. Also, cooling techniques like electron cooling [12] and laser cooling [13] can be applied and thereby reduce the ion beam phase-space volume (emittance), resulting in ion beams of small momentum spread, low divergence and small cross-sectional area. At the ASTRID storage ring, electron cooling can be applied to the ion beam, but this has not been done in any of the present experiments. Instead, the electron cooler is utilized as an electron target in collision experiments.

The storage ring is designed to keep the ion beam confined even during acceleration of the beam, which requires the magnets to ramp up as the energy is increased. This requires a good and stable control of the electromagnets, which in turn makes the storage ring very flexible with respect to changing the mass, energy and charge of the stored ions. At ASTRID, experienced operators are normally in charge of storing and accelerating the ions, but an easy-to-use control system actually permits the experimental physicists themselves to switch from one ion to another and storing that.

The high storage energy possible in a storage ring is especially suitable for merged-beams experiments, where low collision energies are required. As an example, a beam of 2 MeV O_2^- ions travel at the same velocity (*i.e.* at a relative energy of 0 eV) as a beam of 34 eV electrons, which is possible to produce in high intensities. Moreover, the circulation of the ion beam that occurs in storage rings increases the effective ion current, and also the neutral reaction products are easily detected in energy-sensitive solid-state detectors located after the bending magnets. At the high storage energies, these detectors exhibit detection efficiencies of 100%. To summarize, the advantages of using storage rings for atomic physics are:

- Long storage lifetime
- Possibility to efficiently cool the ion beam

- Flexibility with respect to ion mass, charge, energy, etc.
- Well-suited for merged-beams experiments
- High signal intensity
- Easy detection

Storage rings have contributed significantly to the field of experimental atomic and molecular physics since the early 1990's. As an example, the subject of dissociative recombination, which is also studied in this thesis (Chapter 4), has been discussed in a series of conferences starting in Canada in 1988. The first two conferences never treated storage ring experiments, but about a third of the contributions to the third conference were storage ring related. To quote the introductory contribution in the proceedings of the third conference:

"Since the previous meeting of this series in May 1992, the study of dissociative recombination (DR) is living a second youth due to a new generation of experiments using ion storage rings." A. Suzor-Weiner and I. F. Schneider in Ref. [14], page 1.

A review of atomic and molecular physics using heavy-ion storage rings can be found in Ref. [15]. The latest development in the field of storage rings is the construction of electrostatic rings. Where previous rings utilize electromagnets to produce the fields that deflect the charged particles into their storage orbits, several new rings use electric fields with many new and exciting possibilities, which will be described in section 2.3. To conclude, it can be mentioned that within the last couple of years, storage rings for *neutral particles* have been constructed [16, 17].

Ion sources

This thesis deals with ionized atoms and molecules, and it is naturally a prerequisite for the experiments that the desired ions can be produced. Sources of charged particles have been invented, developed and improved over the last century. It is no easy task to construct an ion source that produces beams of high intensities from any given source material. Different ions require different sources; not only are negative and positive ions often, though not always, produced from different sources, but ion sources also operate on different materials ranging from solids to gases.

Experimental development has resulted in ion sources utilizing very different operating principles like high voltage discharges, hot filament emission, high energy sputtering, charge transfer processes, solid-state evaporation and liquid spray techniques. Sources range from the very simple to the quite complex, and most often numerous parameters are within the experimentalist's control, and all must be optimized to achieve the maximum ion output. Even today, new ion sources are being developed and in 2002 part of a Nobel Prize was awarded to ion source technology.

Even today, some experimentalists consider ion sources more or less "black boxes", *i.e.* equipment whose principle of operation is either unknown or unclear in detail and perhaps too difficult to control towards any given desired output. Indeed, though the fundamental physics behind all ion sources is very well understood and the output of most sources can be at least partly controlled, I have myself spent countless hours on trial-and-error experimentation trying to produce a specific ion or to increase the ion current to a level where an experiment can be performed. In section 2.4, the ion sources applied in the present work are all presented.

2.2 The ASTRID heavy-ion storage ring

The ASTRID² storage ring [18, 19, 20, 21] was built at the Department of Physics and Astronomy at the University of Aarhus in the late 1980's, and the first ion beam was successfully stored in 1990. The same year, the first electron beam was successfully stored, thereby making ASTRID the first and only dual-purpose storage ring, capable of storing both positive and negative heavy-ions and electrons.

2.2.1 The storage ring

The ring has a 10 by 10 meter square geometry with two 45° bending magnets in each of the four corners. The straight sections are equipped with quadrupole magnets for focusing purposes and correction dipole magnets for final beam positioning. Fig. 2.1 presents a schematic diagram of the storage ring.

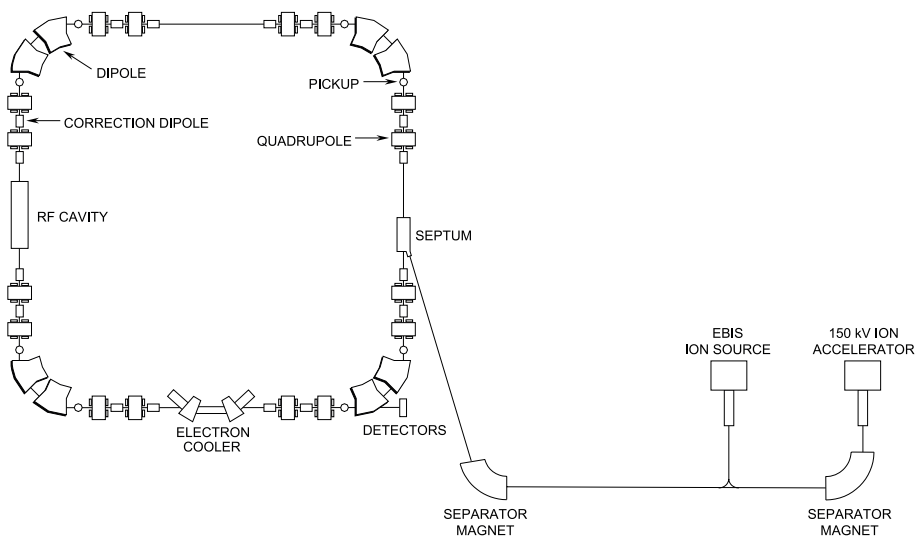


Figure 2.1: Schematic diagram of the ASTRID heavy-ion storage ring. Ions are injected in the right hand side of the ring, circulating counter-clockwise. The electron target (“electron cooler”) is shown in the bottom of the figure, and after the dipole magnet following the electron target a neutral particle detector is shown.

Ions are produced in an ion source mounted on a 200 kV accelerator³ from which they can be extracted out of the source, preaccelerated and mass-selected by an analysis magnet. An EBIS ion source for production of highly-charged ions is also available as a part of the injection system, but this source has not been used for any of the final results presented here. The ions are guided through an injection beam line and injected into the storage ring, where they by means of a radio-frequency acceleration system are further accelerated to the final storage energy. The maximum storage energy, E_{max} , is limited by the magnetic rigidity of the bending magnets, which for ASTRID has a value of $rB \approx 1.93$ Tm [22]. The maximum energy can be calculated from the following formula:

$$E_{max} = 931.5 \left[\sqrt{M_{ion}^2 + 0.3858 Q^2} - M_{ion} \right] \text{ MeV}, \quad (2.1)$$

²ASTRID is an abbreviation of “Aarhus STorage RIng Denmark”.

³Typical acceleration voltage is 150 kV.

where M_{ion} is the ion mass in amu, and Q is the charge of the ion in units of e . As an example, the CO_2^+ ion studied in this thesis was stored at 3.35 MeV, even though the maximum possible energy was 4.08 MeV. To achieve the maximum energy, more time to fine tune the acceleration ramp and the optical elements of the ring would have to be spent. At these high energies, the ion beam lifetimes are limited by collisions with the residual gas in the vacuum system. More than 40 vacuum pumps maintain a mean pressure in the ring in the low 10^{-11} mbar region, and this results in typical beam lifetimes between 1 and 5 seconds.

2.2.2 The electron target

The electron target for collision experiments at ASTRID is provided by an *electron cooler*. This device is mounted in one of the straight sections of ASTRID as depicted in Fig. 2.1. The electron cooler produces a beam of essentially mono-energetic electrons that is merged with the ions in a 0.95 meter interaction region of the storage ring. By ensuring that the electrons are cold, *i.e.* that they have a narrow energy spread, the continuously replaced electrons will act as a heat reservoir for the ion beam. The mutual Coulomb interaction between the electrons and ions will heat the electron beam as the ion energy spread is reduced, and the electron cooler may thus function as a means of cooling the ion beam.

This property has, however, not been applied in any of the experiments of this thesis. Instead, the electron cooler is used as an electron target for collision experiments with a very well-defined relative electron-ion energy. The electron cooler is shown in Fig. 2.2.

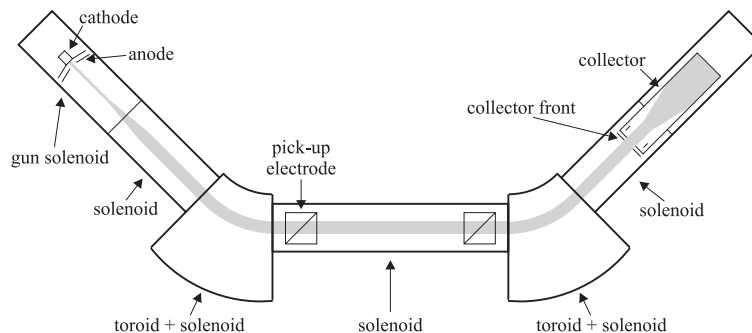


Figure 2.2: Schematic diagram of the electron cooler at ASTRID. Figure captions above the drawing indicate parts inside the vacuum chamber, while figure captions below the drawing are concerned with the magnetic fields. The electrons travel from the cathode in the upper left part of the figure down to the interaction region between the two toroids, and finally up to the collector in the upper right part of the figure.

Electron gun

Electrons are emitted from a BaO coated tungsten cathode of a 1 cm diameter. When heated to about 1200 K, this cathode thermally emits electrons that are then accelerated from the negative acceleration voltage V_{acc} of the cathode towards a grounded anode grid of about 80% transmission. The electron gun is of a modified Pierce geometry [23, 24], *i.e.* the cathode is surrounded by a so-called Pierce shield. This is an electrode configuration which is modeled to such a shape that it together with the potential given by the electron cloud reduces the transverse electric field components on the cathode surface and produces

equipotential lines that are parallel to it [12]. The Pierce shield is lifted to the cathode potential with a small bias voltage added, which in turn results in a rectilinear beam of electrons with an even distribution of the electron density across the beam.

The electron emission is space charge limited, and the magnitude I_e of the extracted electron current is thus given by Child's Law [12]:

$$I_e = P \cdot V_{acc}^a, \quad (2.2)$$

where a is an exponent equal to 1.5. The constant P , called the *perveance*, is determined by the geometry of the electron gun, and it is inversely proportional to the squared cathode-anode distance d :

$$P = \left(\frac{r_0}{d}\right)^2 P_0, \quad (2.3)$$

where $r_0 = 0.5$ cm is the electron beam radius, and:

$$P_0 = \frac{4}{9} \pi \epsilon_0 c \sqrt{e/m_e c^2} \approx 7.3 \times 10^{-6} \text{ A V}^{-3/2}. \quad (2.4)$$

In actual experiments, the exponent a in Eq. 2.2 will normally deviate a little from 1.5. An example of recorded electron currents as a function of acceleration voltages can be seen in Fig. 2.3.

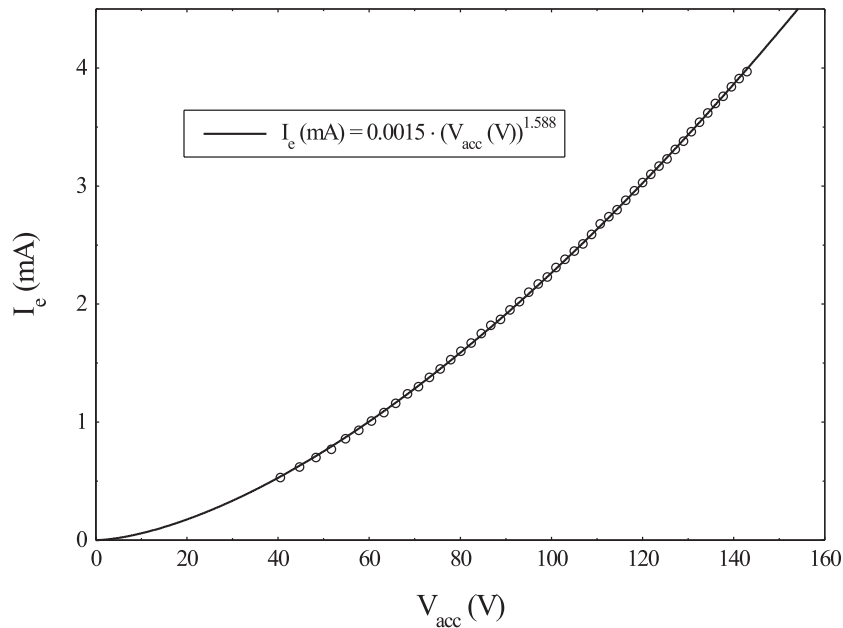


Figure 2.3: Electron current as a function of acceleration voltage recorded during the O_3^- experiment, which is presented in Chapter 3.

The distance d in Eq. 2.3 is variable from outside the vacuum chamber of the electron cooler, and we thus have a means of varying the electron current and thereby to reach a suitable range of currents in a given experiment. Too low an electron current will not produce sufficient reaction signal, while too high a current can have a destructive effect on the stored ion beam. The relevant range of acceleration voltages, V_{acc} , is determined by the energy of the stored ions and the range of relative collision energies that one wishes to explore. Typical electron currents are of the order of a few mA.

Space charge potential

The electron density in the electron cooler is associated with a negative space charge potential, which has a substantial influence on the final electron energy. The electrons emitted from the electron gun are not accelerated from the cathode potential to ground, because the potential difference is reduced by the electron beam space charge potential. The effect is that the electrons are travelling slower than if they were accelerated through the full potential difference, and in the laboratory frame the electron energy E_e^{lab} is given by:

$$E_e^{lab} = \frac{1}{2}m_e v_e^2 = e(V_{acc} + V_{sp}) , \quad (2.5)$$

where m_e and v_e are the electron mass and velocity, respectively, and V_{sp} is the negative space charge potential. This potential is derived in App. A, and it takes the form of:

$$V_{sp}(r) = -K_{sp}(r) \frac{I_e}{\sqrt{E_e^{lab}}} , \quad (2.6)$$

where the factor $K_{sp}(r)$ depends purely on geometrical parameters, and can be shown to vary only slightly as a function of the radius r from the beam axis. In these merged-beams experiments, the ion and electron beams coincide on the axis of the electron cooler. The ion beam is of much smaller spatial extent than the electron beam, and with only the central part of the electron beam participating in the collision experiment, the energy spread due to the radial dependence of the space charge potential does not contribute significantly to the energy resolution of the experiment. It is thus a good approximation to replace $K_{sp}(r)$ in Eq. 2.6 with the *space charge constant* $K = K_{sp}(0)$. By inserting this into Eq. 2.5, we find:

$$E_e^{lab} = e \left(V_{acc} - K \frac{I_e}{\sqrt{E_e^{lab}}} \right) . \quad (2.7)$$

Magnetic fields

The accelerated beam of electrons is guided through the electron cooler by a longitudinal magnetic field supplied by solenoids (see Fig. 2.2). In the regions where the electron and ion beams are merged and separated, toroidal solenoids create relatively weak magnetic fields perpendicular to the electron beam. The light electrons are thus merged with the heavy-ion beam that is left only slightly disturbed in the storage ring. In addition, the electron cooler is fitted in all three straight sections with steering coils capable of producing fields in both dimensions perpendicular to the electron beam.

The electrons emitted from the cathode are guided by the longitudinal magnetic field, which forces the electrons into a *cyclotron motion* around the magnetic field lines. The magnetic flux Φ through a cyclotron orbit of radius r_c in a magnetic field B is given by:

$$\Phi = B\pi r_c^2 , \quad (2.8)$$

and the kinetic energy associated with this motion is:

$$E_{kin}^c = \frac{1}{2}m_e \omega_c^2 r_c^2 , \quad (2.9)$$

where $\omega_c = eB/m_e$ is the cyclotron frequency.

Three-dimensional velocity distribution

The electrons are emitted from a hot cathode in the electron gun, and the velocity distribution of the electrons can be described by a three-dimensional Maxwellian distribution:

$$f(\mathbf{v}_e) = \left(\frac{m_e}{2\pi k T_{cath}} \right)^{3/2} e^{-m_e v_e^2 / 2k T_{cath}} , \quad (2.10)$$

where T_{cath} is the temperature of the electron-emitting cathode.

The velocity distribution described above is valid for electrons emitted from the cathode, but it is not valid for the electrons in the interaction region. This is due to the electron beam transport from the cathode to the interaction region, where the longitudinal and transverse degrees of freedom for the electrons are affected. The result is two-fold: 1) the acceleration of the electron beam from the cathode to the anode causes a kinematic compression of the longitudinal velocity distribution, and 2) an adiabatic expansion of the electron beam reduces the transverse temperature of the beam. The energy spread of the electrons in its moving frame of reference is thus characterized by two different temperatures, a longitudinal temperature T_{\parallel} and a transverse temperature T_{\perp} . The velocity distribution in the moving frame is consequently described by a flattened Maxwellian distribution [25]:

$$f(\mathbf{v}_e) = \frac{m_e}{2\pi k T_{\perp}} e^{-m_e v_{\perp}^2 / 2k T_{\perp}} \sqrt{\frac{m_e}{2\pi k T_{\parallel}}} e^{-m_e v_{\parallel}^2 / 2k T_{\parallel}} , \quad (2.11)$$

where v_{\perp} and v_{\parallel} are the transverse and longitudinal velocities in the moving frame, respectively. The temperatures T_{\parallel} and T_{\perp} are defined by the velocity spread $\sigma = (\langle v^2 \rangle + \langle v \rangle^2)$ according to the equipartition theorem of classical statistical mechanics, which states that the mean value of each independent quadratic term in the energy (*i.e.* $E_{kin} = \frac{1}{2} m \sigma^2$) equals $\frac{1}{2} k T$:

$$\frac{1}{2} k T_{\parallel} = \frac{1}{2} m (\langle v_z^2 \rangle + \langle v_z \rangle^2) , \quad (2.12)$$

and:

$$\frac{1}{2} k T_{\perp} = \frac{1}{2} m (\langle v_x^2 \rangle + \langle v_x \rangle^2) = \frac{1}{2} m (\langle v_y^2 \rangle + \langle v_y \rangle^2) , \quad (2.13)$$

where v_x and v_y are the electron velocity components in the transverse plane, and v_z is the longitudinal electron velocity component.

Longitudinal velocity distribution

When the electron beam is accelerated, the symmetry between the longitudinal and the transverse directions are broken, and the Maxwellian velocity distribution is flattened into that of Eq. 2.11. An acceleration of electrons with a longitudinal temperature T_{cath} to an energy E_0 causes a kinematic compression of the velocity spread corresponding to the temperature [12]:

$$k T_{\parallel} = \frac{(k T_{cath})^2}{4 E_0} . \quad (2.14)$$

For electron energies of $E_0 = 300$ eV, the longitudinal energy spread becomes approximately $10^{-4} \times kT_{cath}$, which is a quite large compression.

There is, however, another and more important contribution to the energy spread. The potential energy stored in the electron-electron interactions will be partly converted into kinetic energy and add to kT_{\parallel} , a process known as *longitudinal-longitudinal relaxation*. This contribution can be added to Eq. 2.14 yielding [26]:

$$kT_{\parallel} = \frac{(kT_{cath})^2}{4E_0} + \frac{2e^2}{4\pi\epsilon_0} n_e^{1/3} . \quad (2.15)$$

For typical electron densities of 10^7 cm $^{-3}$, this additional term amounts to about 0.06 meV which thus dominates the first term of the order of 0.01 meV. As a consequence, T_{\parallel} is essentially independent of the electron energy.

Transverse velocity distribution

There is no acceleration in the transverse direction and thus no kinematic compression of the transverse velocity distribution. Initially, the transverse temperature is determined by the cathode, $T_{\perp} = T_{cath}$, and the energy is stored in the cyclotron motion (Eq. 2.9) around the guiding magnetic field lines. The space charge of the beam gives rise to a small electric field perpendicular to the motion of the electrons, and this combined presence of a magnetic and an electric field results in a motion called a *magnetron motion*, which is superimposed on the cyclotron motion. The energy associated with the magnetron motion is estimated to be 0.01-0.1 eV, and the transverse temperature is therefore expected to be larger than the cathode temperature.

The transverse temperature can be reduced by expanding the electron beam adiabatically, *i.e.* by reducing the confining magnetic field strength slowly without changing the magnetic flux (Eq. 2.8) through the electron cyclotron orbit. This method of transverse cooling in electron coolers was discussed in 1987 [27] and first implemented in CRYRING in Stockholm [28, 29].

In a spatially constant magnetic field, an electron will describe a helical orbit along a magnetic field line, and the Lorentz force will always be directed perpendicular to the guiding line of this orbit. Hence, the transverse and the longitudinal degrees of freedom will be decoupled. In a spatially varying magnetic field, the electron will perform similar motion, but since the field lines are diverging, the Lorentz force experienced by the electron will also have a component along the guiding line, which gives rise to a longitudinal acceleration. This increase in longitudinal energy leads to a decrease of the transverse energy (see Fig. 2.4).

The adiabatic expansion requires the field to vary slowly compared to the frequency of the cyclotron motion. The adiabatic constraint on the expansion can be expressed as the demand that the magnetic flux in the cyclotron orbit (Eq. 2.8) is kept constant, *i.e.* $r_c^2 \propto B^{-1}$. By inserting this and the cyclotron frequency $\omega_c = eB/m_e$ into Eq. 2.9, we see that the cyclotron energy is proportional to the magnetic field B . When the electrons move from the strong magnetic field of the electron gun solenoid to the weaker field of the main solenoid, the kinetic energy associated with the cyclotron motion is reduced by the expansion factor:

$$f_a = \frac{B_{gun}}{B_{solenoid}} . \quad (2.16)$$

As a result, the transverse temperature is decreased by a factor of f_a , which for all present experiments equals 4.5. Simultaneously, the longitudinal temperature increases. The transverse energy is reduced from kT_{cath} to kT_{cath}/f_a , and the effect on the longitudinal degree of freedom can thus be viewed as an increase in the cathode temperature by the amount $(1 - 1/f_a)kT_{cath}$. This increase in longitudinal temperature is negligible compared to the longitudinal-longitudinal heating described in Eq. 2.15.

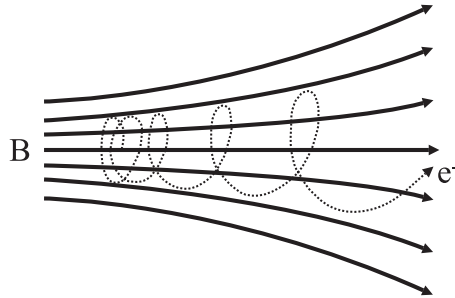


Figure 2.4: Schematic drawing of electron motion in an adiabatically expanding magnetic field. The magnetic force has a longitudinal component, which will convert the transverse electron energy into longitudinal energy.

Another contribution to the energy distribution should be mentioned: the longitudinal temperature becomes quite small compared to the transverse temperature, and the beam is now in an extremely anisotropic state ($T_{\parallel} \ll T_{\perp}$) described by the flattened Maxwellian distribution of Eq. 2.11. Coulomb collisions and other processes will try to force the velocity distribution into thermal equilibrium ($T_{\parallel} \approx T_{\perp}$), whereby the longitudinal energy spread of the beam will increase as the beam thermalizes. This thermal relaxation process is referred to as the *transverse-longitudinal Boersch effect*, and it increases with increasing electron current and decreasing magnetic field. For low electron currents and high magnetic fields, the cyclotron radius r_c becomes much smaller than the average distance between electrons in the beam, and if the longitudinal temperature is sufficiently small, the electron-electron collisions becomes adiabatic and the energy-transfer from the transverse motion to the longitudinal motion becomes strongly suppressed. This is the case for the electron cooler at ASTRID, and T_{\parallel} is thus determined by the longitudinal-longitudinal relaxation [30, 31, 32].

With a cathode operating at a temperature of about 1200 K, the thermally emitted electrons near the cathode will have an energy spread of about $\frac{3}{2}kT_{cath} \approx 0.16$ eV. After acceleration and adiabatic expansion at ASTRID, the energy spreads are $kT_{\perp} \approx 22$ meV and $kT_{\parallel} = (1.0 \pm 0.5)$ meV. The latter value is the result of an experimental determination of the electron temperature extracted from measurements of narrow resonance widths in dielectronic recombination rate coefficients [25]. The measurement also yielded $kT_{\perp} = (135 \pm 10)$ meV, but this was determined before adiabatic expansion of the electron beam was employed at ASTRID.

It should finally be mentioned that other methods of cooling the electron beam have been suggested, *e.g.* the use of a cold photo-cathode as an electron source, where electrons are emitted by irradiating a cooled GaAs crystal with an intense, near-infrared laser light beam [33]. Presently, however, only hot-cathode electron guns have been employed in the electron coolers of heavy-ion storage rings.

Electron density

By using the electron current measured in the collector of the electron cooler and the laboratory energy of the electrons, the electron density can be calculated according to the following equation:

$$n_e [\text{cm}^{-3}] = 3.35 \cdot 10^7 \cdot \frac{I_e [\text{mA}]}{f_a \cdot (r_0 [\text{cm}])^2 \cdot \sqrt{E_e^{lab} [\text{eV}]}} , \quad (2.17)$$

where r_0 is the cathode radius, I_e the magnitude of the electron current, f_a is the expansion factor, and E_e^{lab} is the electron energy of Eq. 2.7.

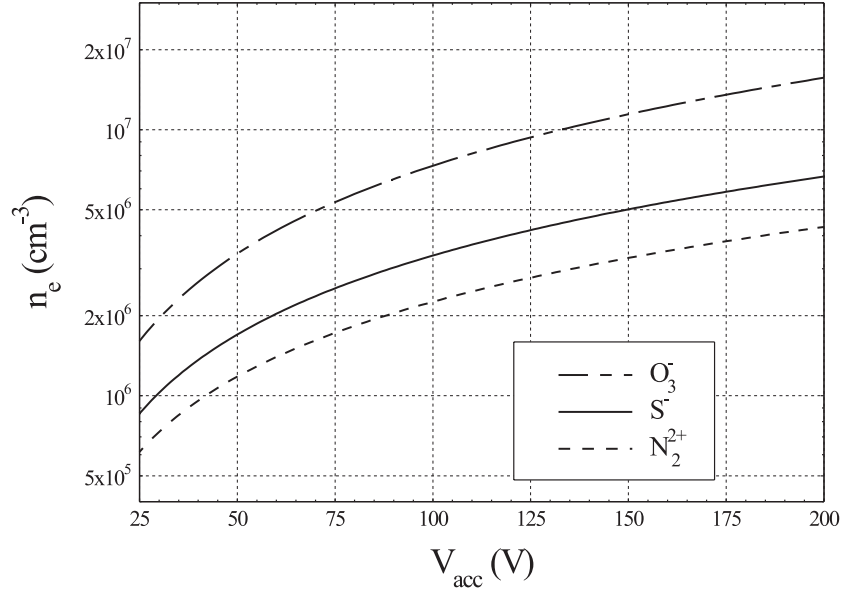


Figure 2.5: Electron densities calculated from Eq. 2.17 using data from real experiments, the results of which will be presented in the following chapters.

The electron density is dependent on the relevant ion and electron energies and the electron gun perveances applied in each experiment. A graph of three different electron densities from experiments to be presented in the following chapters are shown in Fig. 2.5 as a function of the electron acceleration voltage. These densities in the range from 10^6 to 10^7 cm^{-3} are typical for all the experiments in this thesis.

Relative energy and resolution

Electron-ion collisions can be studied experimentally as a function of the relative collision energy by varying the electron energy and keeping the ion energy constant. For two parallel beams of electrons and ions, the relative collision energy, E_{rel} , is calculated from the beam energies of the electrons and ions in the laboratory frame, E_e^{lab} and E_i respectively, through the following equation:

$$E_{rel} = \frac{1}{2} m_e (v_i - v_e)^2 = \left(\sqrt{\frac{m_e}{M_{ion}}} E_i - \sqrt{E_e^{lab}} \right)^2 , \quad (2.18)$$

where M_{ion} is the ionic mass. The quantity E_i is directly measurable, while E_e^{lab} has to be obtained by solving Eq. 2.7 iteratively using measured values of V_{acc} and I_e . The space

charge constant K can be determined experimentally utilizing the fact that dissociative recombination cross-sections reach a maximum at $E_{rel} = 0$. From Eq. 2.18 we can then find E_e^{lab} , and by measuring the values of V_{acc} and I_e at which the maximum cross-section is observed, the space charge constant can be found from Eq. 2.7.

The energy spread of the electrons is an essential parameter of the experiments, especially if narrow structures in the cross-sections are searched. Generally, the main contribution to the energy resolution is attributed the target electrons since the energy spread of the stored ion beam is quite small. It is therefore desirable to produce an electron beam that has a narrow velocity distribution as described above.

For a given detuning velocity $\Delta = |\mathbf{v}_{ion} - \mathbf{v}_e|$, the electron velocity distribution in the rest frame of the ions is:

$$f(\mathbf{v}_e, \Delta) = \frac{m_e}{2\pi kT_{\perp}} e^{-m_e v_{\perp}^2 / 2kT_{\perp}} \sqrt{\frac{m_e}{2\pi kT_{\parallel}}} e^{-m_e (v_{\parallel} - \Delta)^2 / 2kT_{\parallel}}. \quad (2.19)$$

The detuning velocity defines the detuning energy through the relation $E_d = \frac{1}{2}m_e\Delta^2$, which for parallel ion and electron beams means $E_d = E_{rel}$. We can now perform a change of variables from longitudinal velocity to electron energy $E_e = \frac{1}{2}m_e(v_{\perp}^2 + v_{\parallel}^2)$ and the distribution of electron energies in the ion rest frame can then be determined by integrating over the transverse velocities:

$$f(E_e, E_d) = \int f(\mathbf{v}_e, \Delta) \left(\frac{dv_{\parallel}}{dE_e} \right) dv_{\perp}. \quad (2.20)$$

This distribution function gives the distribution of relative collision energies encountered in the electron-ion scattering experiments. $f(E_e, E_d)$ is shown in Fig. 2.6 for three different detuning energies. Each graph plots the distribution function for both an unexpanded beam ($kT_{\perp} = 100$ meV) and an adiabatically expanded beam ($kT_{\perp} = 25$ meV). The longitudinal temperature is constant ($kT_{\parallel} = 0.5$ meV) for all three graphs.

The energy spread, $\delta E_e(E_d)$, as a function of the detuning energy can be estimated from the expression:

$$\begin{aligned} E_e - E_d &= \frac{1}{2}m_e(v_{\perp}^2 + v_{\parallel}^2) - \frac{1}{2}m_e\Delta^2 \\ &= \frac{1}{2}m_e v_{\perp}^2 + \frac{1}{2}m_e(v_{\parallel} - \Delta)^2 + 2\sqrt{\frac{1}{2}m_e(v_{\parallel} - \Delta)^2 E_d}. \end{aligned} \quad (2.21)$$

We now convert each term in this expression into temperatures by using the equipartition theorem:

$$\delta E_e(E_d) = kT_{\perp} + \frac{1}{2}kT_{\parallel} + \sqrt{2kT_{\parallel}E_d}. \quad (2.22)$$

As is apparent from Fig. 2.6, the energy resolution at low detuning energies is dominated by the transverse temperature, while the longitudinal temperature dominates at high detuning energies.

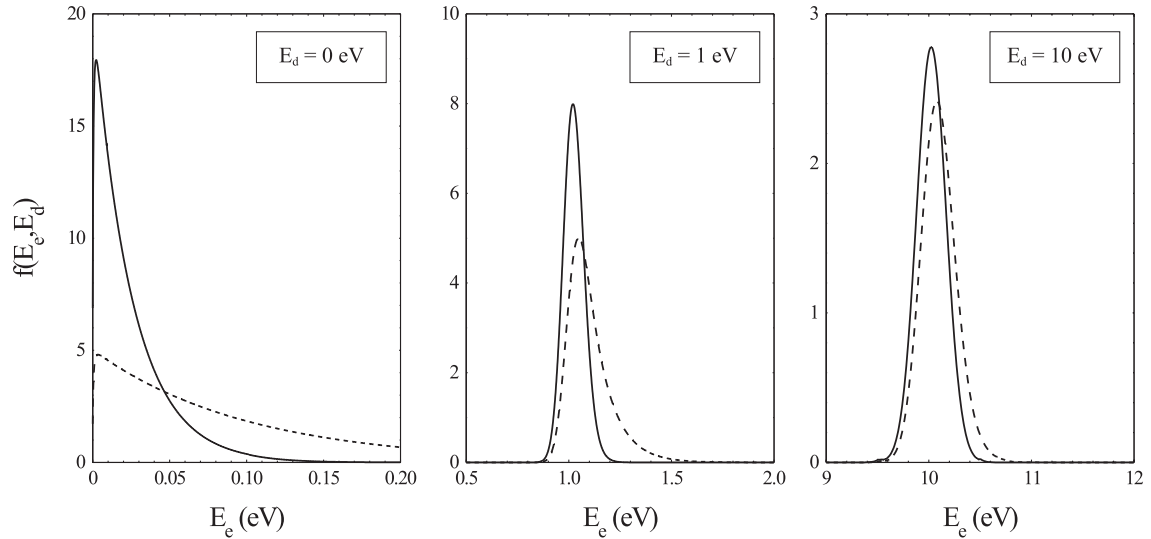


Figure 2.6: The electron energy distribution $f(E_e, E_d)$ in the ion rest frame plotted for three different detuning energies E_d . The longitudinal temperature is $kT_{\parallel} = 0.5$ meV, while each figure shows the distribution for two different transverse temperatures: i) an unexpanded beam with $kT_{\perp} = 100$ meV (dashed curve), and ii) an expanded beam with $kT_{\perp} = 25$ meV (solid curve).

Contribution from toroidal solenoids

The relative electron-ion velocities in the toroid regions, where the beams are merged and separated, are different from the velocities inside the interaction region. In the central part of the electron cooler, where the ion and electron velocity vectors are parallel, the relative energy is defined by Eq. 2.18, whereas in the toroid regions (see Fig. 2.7) a range of higher relative energies are encountered. This produces a small toroid contribution to the rate coefficients that we measure, but the data presented in this article are all corrected for this using an iterative procedure [34].

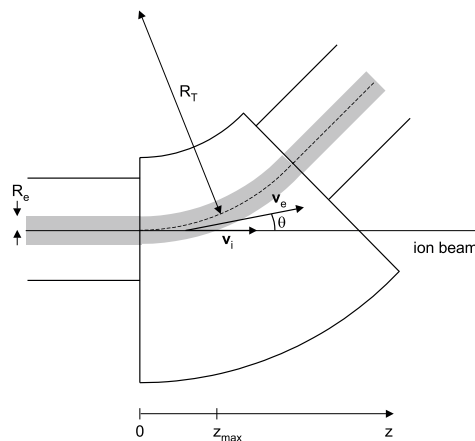


Figure 2.7: Close-up of a toroid magnet region within the electron cooler.

The radius of the electron beam is much larger than the radius of the ion beam, and we can thus assume that the ions are completely surrounded by electrons. We can then find the following equation for the relative energies encountered in the toroid regions (see

App. B):

$$E_{rel}^{lab}(z) = E_{rel} + 2\sqrt{E_{cool}E_e^{lab}} \left(1 - \frac{\sqrt{R_T^2 - z^2}}{R_T} \right), \quad (2.23)$$

where z is the longitudinal position within the toroid region, $R_T = 40$ cm the radius of curvature of the toroid magnet, and $E_{cool} = \frac{m_e}{M_{ion}}E_{ion}$ is the electron energy in the laboratory frame, for which the electrons and ions travel with the same velocity, a situation required for electron cooling of the ion beam.

The measured rate coefficient $\langle v\sigma \rangle_{meas}$ at a given relative energy is then given by:

$$\langle v\sigma \rangle_{meas}(E_{rel}) \cdot L = \langle v\sigma \rangle(E_{rel}) \cdot L + 2 \int_0^{z_{max}} \langle v\sigma \rangle(z) dz \quad (2.24)$$

where $z_{max} = \sqrt{(R_T + R_e)^2 - R_T^2}$ is the longitudinal position corresponding to the highest relative energy E_{max} encountered in the toroid region.

The magnitude of the toroid contribution can be seen in Fig. 2.8, where two different measured rate coefficients are shown both before and after correction for toroid contribution. The top figure consists of actually measured data of electron scattering on SO_2^- (to be presented in detail in Chapter 3), while the bottom part of the figure shows a model rate coefficient typical of dissociative recombination of cations.

Diagnostics

It is of the utmost importance that the electron beam is well-steered and free of trapped charges and because of this, several diagnostics techniques are applied prior to an experiment. During each measurement, the electron current is determined as a function of the acceleration voltage, and the result should follow the relation of Eq. 2.2. Deviations from this have actually been detected once, and a problem with the chopper supply (which was not properly grounded) was located.

If the beam is not steered properly through the interaction region and into the collector, it might hit surfaces of the vacuum system and thereby cause an increase in the mean vacuum pressure and an emission of secondary electrons. The latter will be trapped in the longitudinal magnetic field where they can drift into the interaction region and cause false electron-ion scattering events. In front of the electron beam collector, an extra electrode is located (“collector front” in Fig. 2.2), and by continuously monitoring that the full electron beam current enters the collector, with no current on the collector front, we can ensure that the entire beam is steered into the collector. We can further use the two sets of vertical and horizontal pick-up electrodes in the electron cooler to verify that the electron beam is well-aligned on the axis of the interaction region.

Another source of error is the possible trapping of ions in the electron beam. The degree of trapping can be examined by monitoring the time-evolution of the signal from the pick-up electrodes on an oscilloscope while passing a chopped electron beam through the interaction region. The electrons induce a signal on the electrodes, and if any additional charge accumulates in the interaction region while the electron beam is on, this will be observed as a change in the signal.

An elaborate description of electron cooler theory can be found in Ref. [12].

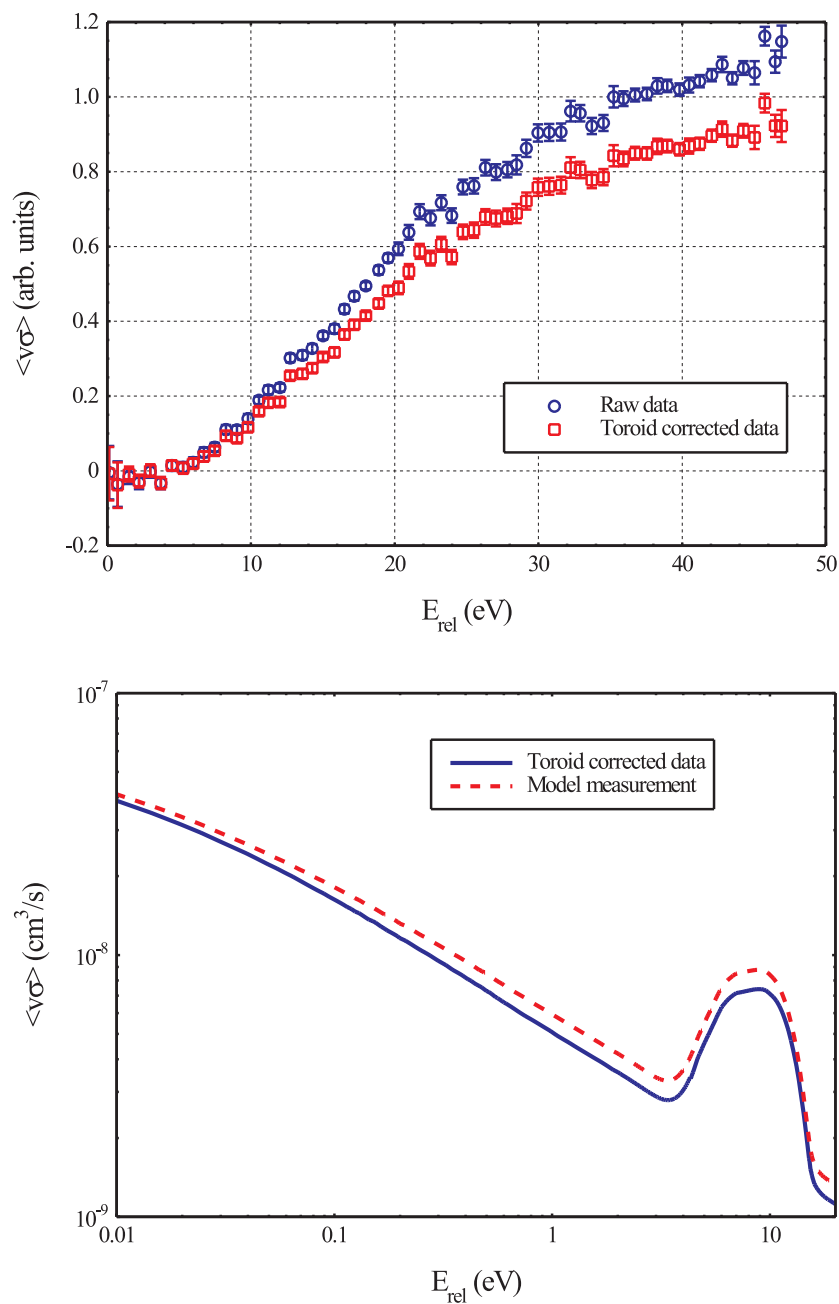


Figure 2.8: Toroid contributions in electron scattering on negative ions (top figure) and in dissociative recombination of positive ions (bottom figure). The top figure shows data from electron scattering on SO_2^- , which will be presented in Chapter 3. The *raw data* are the actual measurement, while the *toroid corrected data* is the rate coefficient when the toroid contribution has been removed using the iterative procedure describe in Eq. 2.24. The bottom figure shows a typical dissociative recombination rate coefficient (*model measurement*) and the corresponding toroid corrected data.

2.2.3 Experimental procedures

Experiments are performed by producing, storing and accelerating the ions, bombarding them with electrons of a particular energy and extracting the rate coefficients from the measured number of reactants and products. In short, the number of reactants are obtained through measurements of electron and ion currents, while the number of products are counted from a surface-barrier type solid-state detector (SSD), which is positioned right after the bending magnet following the interaction region. Neutral fragments created in the electron cooler will pass unaffected through the bending magnet, and when the fragments impact upon the detector they will result in a signal proportional to the energy carried by the particles. If a molecular ion is neutralized in ASTRID, the resulting neutral fragments will result in an SSD peak corresponding to the energy of the stored ion beam. If, however, the molecular ion dissociates into both neutral and charged fragments, only the neutral particles will reach the SSD, thus yielding a peak of only a fraction of the full beam energy. An example of such a *pulse height spectrum* from the SSD is shown in Fig. 2.9, where an ion beam of O_3^- has produced a spectrum with peaks corresponding to one, two and three neutral oxygen atoms.

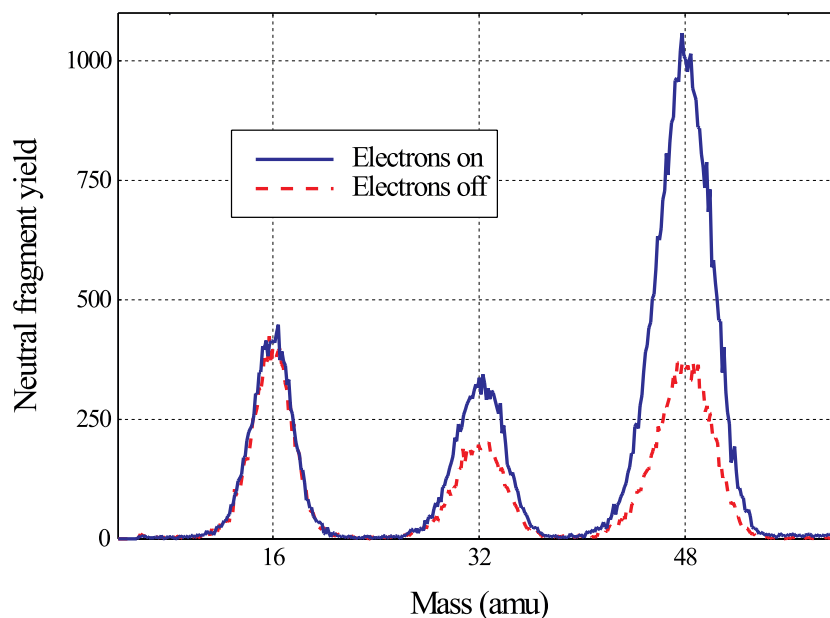


Figure 2.9: Output from the energy-sensitive solid-state detector obtained with storage of O_3^- . Neutral fragments impacting upon the detector result in a signal proportional to the energy carried by the particles. The spectrum shows the signal for both background-induced and electron-induced reactions. This spectrum was recorded during an experiment, which will be presented in Chapter 3.

In front of the SSD we have the opportunity to insert an *imaging detector*, which consists of a multi-channel or multi-sphere plate (MCP/MSP) positioned in front of a phosphorus screen. Any particle that hits this detector will cause a burst of electrons to be emitted from the channel plate to the phosphorus screen, which will light up in a green flash⁴. The imaging detector is used both as a beam detector during storage of a new ion beam

⁴The imaging technique is, by the way, the exact same technique applied in night vision goggles. The only difference is the extra presence of a photocathode, which converts the sparse number of night-time photons into electrons that then result in a green image on the phosphorus screen.

in ASTRID and as an ion beam positioning tool right before undertaking measurements for the purpose of obtaining good overlap between electron and ion beam. In the latter case, the ion beam is initially positioned visually using the neutral fragment signal on the imaging detector, and finally by optimizing on the signal-to-noise ratio of the SSD detector.

To distinguish between neutral fragments created by electron-impact and those created in collisions with residual gas (background signal), the electron beam is chopped by alternating the electron gun anode voltage between ground and -3 kV. The background signal is highly dependent on the residual gas pressure in the storage ring, and the chopping frequency (typically about 20 Hz) is thus chosen to be faster than the response time of the vacuum system.

The data acquisition system at ASTRID divides an electron scattering measurement into a number of time *samples* that again consist of a number of chopper periods (see Fig. 2.10). Typically, a measurement consists of 20 samples that are distributed over the entire measuring period of a duration from 5 to 10 seconds.

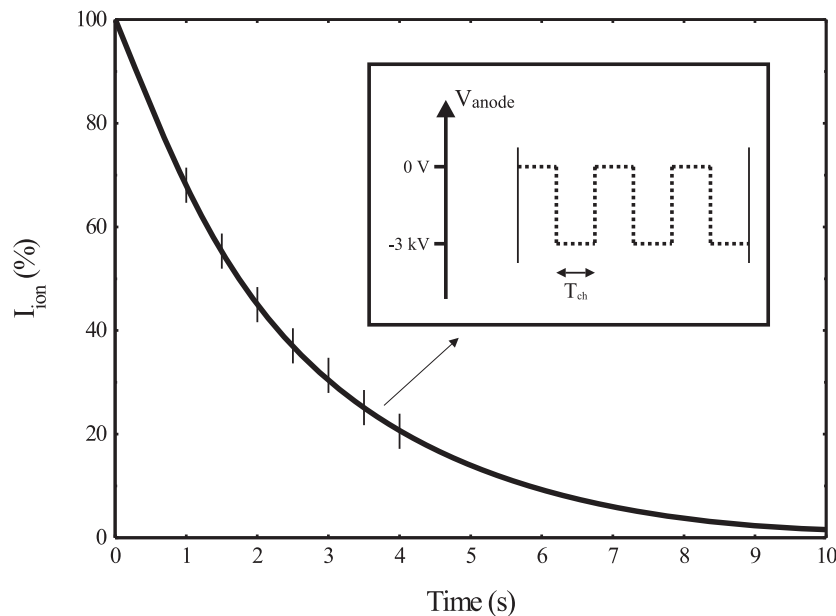


Figure 2.10: Schematic diagram of the timing of an electron scattering experiment. The graph shows the ion current as a function of time after injection into ASTRID. In this example, the measurement is divided into 6 samples with 3 chopper periods each.

If the ion current in the ring is very high, we will normally experience dead-time and pile-up effects in the detection system. The latter is quite easy to detect by examining the SSD spectrum, because pile-up creates peaks in the spectrum at positions corresponding to the double energy of the true fragment peaks⁵. To avoid these problems, one can wait for the stored ion current to decrease to an acceptable level. Moreover, our analysis software has an option where we can choose which time sample numbers we wish to include in the analysis. By starting from a late sample, data with pile-up effects can be discarded. All data presented in this thesis have been cleaned of pile-up effects.

⁵This is one of the very few instances in science, where a researcher has problems with too much signal.

The absolute rate coefficient for a given process can be written in terms of measurable quantities as (see App. C.1):

$$\langle v\sigma \rangle = \frac{N_s - N_b f}{N_{ion}} \frac{v_i}{n_e L \epsilon}, \quad (2.25)$$

where v is the relative velocity, σ the cross-section, v_i the ion velocity, n_e the electron density, L the length of the interaction region and ϵ ($= 1$) the detection efficiency. N_s and N_b are the rates of neutrals (of a given peak in the SSD spectrum) recorded with the electron beam on and off, respectively. Since N_s and N_b are not recorded simultaneously, the factor $f = e^{T_{ch}/\tau}$, where $1/(2T_{ch})$ is the chopping frequency and τ is the ion beam lifetime⁶, is inserted to correct for the exponential decay of the ion beam. N_{ion} is the rate of ions through the electron cooler and this can be extracted from the ion beam current measured by a current transformer. A relative rate coefficient is obtained as a function of energy by replacing N_{ion} with the rate of neutrals produced from collisions with the residual gas. The absolute rate coefficient (Eq. 2.25) is then measured at a single collision energy E_{rel} , and this is used to put the relative rate coefficient on an absolute scale.

When extracting the cross-section σ from a measured rate coefficient $\langle v\sigma \rangle$, the electron velocity distribution $f(\mathbf{v}_e, \Delta)$ as given in Eq. 2.19 must be considered. Since $m_e \ll M_{ion}$, the spread in relative energies is dominated by the electron energy distribution. The rate coefficient is then the velocity-weighted cross-section averaged over the electron velocity distribution:

$$\langle v\sigma \rangle = \int v_e \sigma(v_e) f(\mathbf{v}_e, \Delta) d\mathbf{v}_e. \quad (2.26)$$

The rate coefficient is converted to cross-section by dividing with the average electron velocity, $\sigma = \langle v\sigma \rangle / \sqrt{2E_{rel}/m_e}$. Significant deviations from the true cross-section will occur only for energies lower than $\approx kT_{\perp}$, where the finite energy resolution of the electron beam is of importance. This is relevant for the rate coefficients for electron scattering on positive ions, to be presented later in this thesis, while the rate coefficients for the negative ions are unaffected by it.

2.3 The ELISA electrostatic storage ring

ELISA⁷ is the second storage ring built at the Department of Physics and Astronomy in Århus [35, 36]. It differs significantly not only from ASTRID, but also from other conventional magnetic storage rings, due to the electrostatic fields used for the charged particle deflection. The dipole and quadrupole magnets of ASTRID are in ELISA replaced by electrostatic dipole and quadrupole steering elements.

2.3.1 The storage ring

In a magnetic storage ring, the charged particles are deflected by the magnetic Lorentz force caused by a magnetic field B that is perpendicular to the direction of motion. This force causes a centripetal acceleration, v^2/r , which makes the particles move in a circular orbit with a radius of curvature r :

⁶The beam lifetime is here defined as the time it takes for the number of ions to decrease to $1/e$ of the initially injected number.

⁷ELISA is an abbreviation of “ELectrostatic Ion Storage ring, Aarhus”.

$$F = qvB = m\frac{v^2}{r}, \quad (2.27)$$

where q , m and v are the charge, mass and velocity, respectively, of the particles. The velocity of the particles is determined by the kinetic energy E , which again is determined by the acceleration voltage V_{acc} :

$$E = \frac{1}{2}mv^2 = qV_{acc}. \quad (2.28)$$

By isolating the velocity from Eq. 2.28 and inserting it into Eq. 2.27, we get the equation of motion for a charged particle in a magnetic field:

$$\frac{m}{q} = \frac{B^2 r^2}{2V_{acc}}. \quad (2.29)$$

It is thus the mass-to-charge ratio of the particles that determines the required magnetic field which bends the direction of motion of the particles in the stored orbit. At ASTRID the radius of curvature in the bending dipoles is $r \approx 1.2$ m and the magnetic rigidity is $rB_{max} \approx 1.93$.

In an electrostatic storage ring, the bending force is applied by an electric field \mathcal{E} , which causes deflection through the electrostatic Lorentz force:

$$F = q\mathcal{E} = m\frac{v^2}{r}. \quad (2.30)$$

This equation is only valid if the electric field is perpendicular to the velocity vector of the ions, which is the case for the field between plane-parallel bending electrodes. Initially, the bending electrodes of ELISA were spherical, the result of which was a coupling between the longitudinal and transverse motions. This deviation from a circular motion was, however, small and could be neglected. Later on, the bending electrodes were changed to a cylindrical geometry, which was due to an observation that the spherical electrodes caused the ion beam lifetime to decrease significantly with increasing beam intensity. This is believed to have been due to the focusing effect of the spherical electrodes, which caused a narrow waist in the beam where the ionic space charge forced the beam to blow-up. This problem has been reduced with the cylindrical electrodes.

Now, the velocity from Eq. 2.28 can be inserted into Eq. 2.30, and the equation of motion in an electric field is found:

$$r\mathcal{E} = 2V_{acc}. \quad (2.31)$$

The ring is thus mass-independent⁸, which is one of the primary differences from conventional storage rings. This also makes it quite simple to switch between stored ions of different mass, since the only parameters that need changing is the ion source analysis magnet and a timing parameter related to the injection procedure.

A schematic diagram of ELISA can be seen in Fig. 2.11. The ring has a race-track shape with a 160° cylindrical electrostatic deflector in each end supplying the required electrostatic bending field. In each straight section the ring is fitted with electrostatic steering electrodes for vertical and horizontal correction and pairs of electrostatic quadrupoles for

⁸Notice that at ELISA all ion sources currently employ magnetic analysis when selecting a specific ion from the ion beam, and this sets a mass limit to the ions that can be injected into ELISA.

focusing purposes. All electrodes close to the ion beam are gold-plated in order to avoid surface oxide layers to develop.

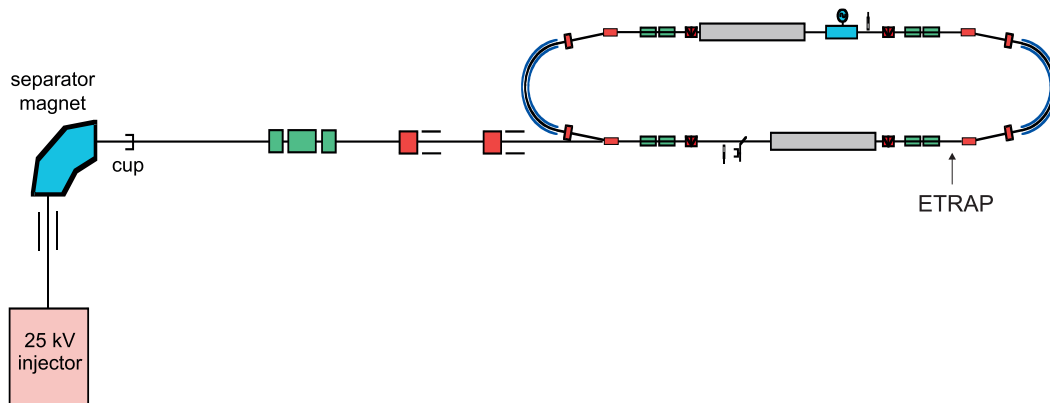


Figure 2.11: Schematic diagram of the electrostatic ion storage ring ELISA. The position of the electron target ETRAP is indicated.

The latest development at ELISA is the installation of an electron target named ETRAP. The position of this target is indicated in Fig. 2.11. The target is a magnetically confined electron beam that crosses the ion beam in a 90 degree angle. This target has been installed and tested during my PhD work, and this particular part of ELISA will be presented in Chapter 5.

The advantages of ELISA are many. As mentioned it is mass-independent, which makes it very easy to change between different ions, and in general it is actually quite easy to operate due to only a few optical elements being present in the ring. This also means that it is possible to store very weak beams of *e.g.* ionic biomolecules and clusters, because the parameters of operation can be determined for a stronger ion beam before changing to the weak beam. Also, the lack of electromagnets means no hysteresis and remanent field effects, and no cooling water will have to be supplied to the ring. Moreover, there are no magnetic fields in the interaction regions of an electrostatic storage ring, and this may be of significant importance in some experiments [37].

Every storage ring needs a very low vacuum to guarantee a long lifetime of the ion beam. Ultra-high vacuum is achieved by baking the ring, but due to the small size of ELISA, this can actually be done by mounting an insulating box around the entire ring, thus baking all of ELISA and not only the beamline. This box can also be used to cool the storage ring, as some experiments require a reduction of black-body radiation. The box is simply mounted, and liquid nitrogen is sprayed over the storage ring⁹. Temperature control from room temperature down to about -55 °C has been demonstrated [37, 38]. This temperature control is primarily possible because of the small size of ELISA, but the compact size is also important when studying slow biomolecules or similar heavy ions, because the revolution frequency for these species is still quite high.

Finally, it is not unimportant that the ring is much cheaper to build than a traditional storage ring. To summarize, the advantages of ELISA are:

- Mass-independent; easy change of ion
- Few optical elements; simple to operate

⁹At a rate of some 20 liters per hour.

- No hysteresis and remanent fields
- No cooling water
- Smaller size; possibility of cooling and heating the ring
- Good vacuum
- No magnetic fields in the interaction regions
- Cheaper

The main disadvantage of ELISA is that it operates at much smaller storage energies than *e.g.* the ASTRID storage ring. The maximum storage energy of ELISA is 25 keV, whereas the typical injection energy at ASTRID is 150 keV for singly-charged ions. At ASTRID, the injection is even followed by further acceleration, yielding final storage energies of several MeV. It should, however, be possible to build electrostatic storage rings of much higher storage energy than that of ELISA.

ELISA was the first electrostatic storage ring built¹⁰, but an electrostatic storage ring has recently been build in Tokyo [39]. This ring is very similar to ELISA, but a merged-beams setup has been chosen for the electron target, and the bending electrodes were constructed with cylindrical geometry from the beginning. Also, the Manne Siegbahn Laboratory in Stockholm is currently developing a new electrostatic storage ring named the Double Electrostatic Storage Ion Ring ExpEriment (DESIREE), which *e.g.* will make merged-beam studies of charge exchange between internally cooled positive and negative molecular ions possible. Finally, it should be mentioned that other groups are developing electrostatic traps in which electron scattering experiments can be performed. As an example of this can be mentioned that of the group of Daniel Zajfman at the Weizmann Institute of Science in Israel. Their work is described in Refs. [40, 41], and together with ELISA this equipment bridges the gap between traditional ion traps [42] and large magnetic storage rings [43].

2.3.2 The electron target

As mentioned, the electron target ETRAP at ELISA is a crossed-beams setup, and though a detailed description of the apparatus is saved for Chapter 5, this section will briefly outline the main differences between the crossed- and merged-beams setup. The physics of the electron beam in ETRAP is basically identical to that of the electron cooler at ASTRID, though the ETRAP beam is not adiabatically expanded. This is in principle possible to do, however.

The electrostatic storage ring in Japan uses a merged-beams setup for the electron target, and this could also have been the choice for ELISA. ELISA is, however, a low energy storage ring intended for experiments with heavy molecular ions, and the electron energies required for reaching zero relative energy in the merged-beams setup (Eq. 2.18) will be close to zero. As the electron currents that can be extracted from the cathode is close to zero at low acceleration voltages, the main advantage of the merged-beams setup (the possibility to study near-zero energy collision) is lost. It is also the intention to study collisions at ELISA using the so-called *imaging technique*, where neutral reaction products are detected using a position sensitive detector for the purpose of determining the kinetic

¹⁰Actually, an electrostatic test storage ring was constructed in the mid-1950's at Brookhaven, but this ring never produced any physics results.

energies of the fragments. In this case a very short interaction length is an advantage. A disadvantage of the crossed-beams setup is, as mentioned, the radial dependence of the space charge potential, which can be avoided in the merged-beams setup, where the ion beam overlaps with the electron beam on the common center axis.

Relative energy

The relative collision energy in a crossed-beams setup differs somewhat from that of the merged-beams setup (Eq. 2.18):

$$E_{rel} = E_e^{lab} + \frac{m_e}{M_{ion}} E_{ion} , \quad (2.32)$$

where E_e^{lab} is the electron energy in the laboratory reference frame, while M_{ion} and E_{ion} are the mass and energy, respectively, of the ions. This equation is meaningful only if the electron energy stored in the transverse motion is much smaller than that of the longitudinal electron energy, but this condition is fulfilled in ETRAP.

Space charge potential in crossed-beams

The energy distribution of the crossed-beams setup is fundamentally different from that of the merged-beams setup. As discussed on page 10, the space charge potential of an electron beam is a function of the distance from the axis of the beam. In the merged beams setup, the ion beam is centered on the axis of a much wider electron beam, and the space charge potential is approximated by a constant $K = K_{sp}(0)$. In the case of a crossed-beams experiments, the ion beam will experience the full range of different longitudinal electron energies induced by the space charge potential as it traverses the perpendicularly moving electron beam.

At each value of the radius r , the electron energy distribution can be described by the flattened Maxwell distribution of Eq. 2.11. The longitudinal energy distribution in the laboratory frame can be written as:

$$f(r, E_{\parallel}) dr dE_{\parallel} = \frac{1}{2\sqrt{\pi kT_{\parallel}}} e^{-\left(\sqrt{E_{\parallel}} - \sqrt{E(r)}\right)^2 / kT_{\parallel}} \frac{1}{\sqrt{E_{\parallel}}} dr dE_{\parallel} , \quad (2.33)$$

where $E(r)$ is the electron energy around which the energy distribution is centered. This can be found iteratively from the equation:

$$E(r) = e \left(V_{acc} - K_{sp}(r) \frac{I_e}{\sqrt{E(r)}} \right) . \quad (2.34)$$

Examples of the longitudinal energy distribution at two given radii are shown in Fig. 2.12. The calculation assumes an electron current of $I_e = 1.78$ mA at an acceleration voltage of 40 V, and a longitudinal temperature of $kT_{\parallel} = 0.5$ meV.

It can be seen that the energy spread at a given radius is much smaller than the energy difference between $E(r)$ for different values of r . The energy resolution is therefore limited by the radial dependence of the space charge potential, and the total longitudinal velocity distribution can be found by calculating an average over r :

$$f(E_{\parallel}) dE_{\parallel} = \frac{1}{\pi R_e^2} \int_0^{R_e} f(r, E_{\parallel}) 2\pi r dr dE_{\parallel} . \quad (2.35)$$

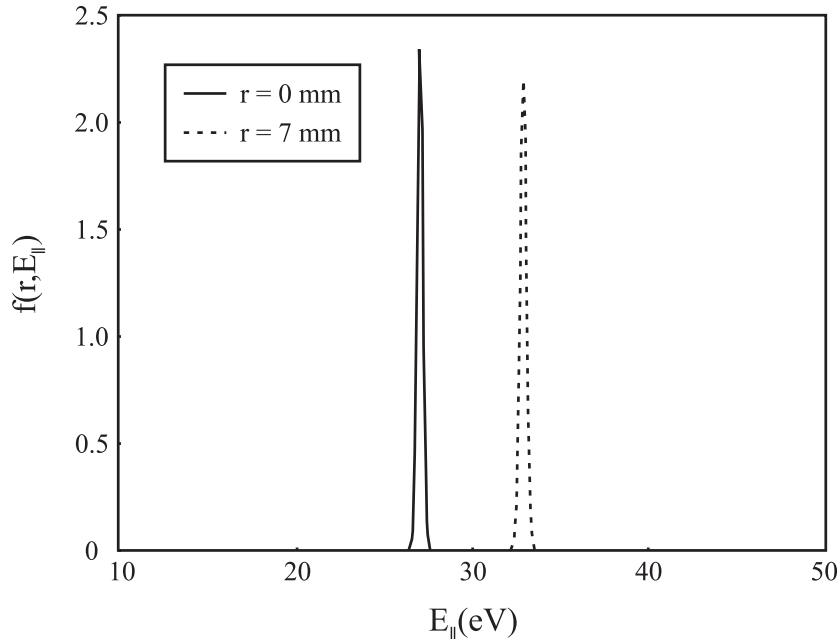


Figure 2.12: Calculated longitudinal energy distributions in the laboratory frame for two different values of r corresponding the center and the outer edge of the electron beam.

2.3.3 Experimental procedures

Measurements at ELISA are performed in a manner quite similar to experiments at ASTRID. Ions are produced, accelerated and stored, but they are not further accelerated to higher energies. In ETRAP, a chopped electron beam is scattered on the ions, and neutral particles are counted by a detector. The typical storage energy in ELISA is 22 keV, and this means that the energy-sensitive solid-state detector used at ASTRID to distinguish between particles of different mass cannot be applied in ELISA experiments. We can thus measure total rate coefficients only, and this is done by an imaging detector of the same type as the one that can be used at ASTRID (see page 19). Neutral particles created in the interaction region in ETRAP will pass unaffected through the 10° deflector following ETRAP, and here they will impact upon the imaging detector. In experiments where the total rate coefficient is the quantity to be measured, the imaging property of the detector is not utilized, instead the output from the MCP is used as the signal from which the *number* of neutral particles is extracted.

Rate coefficients can be measured as a function of the relative electron-ion energy (Eq. 2.32) by varying the electron acceleration voltage. Each experiment monitors the electron current and the number of neutral particles created both with and without the electron beam, and a relative rate coefficient can thus be found from an equation similar to Eq. 2.25:

$$\langle v\sigma \rangle = \frac{N_s - N_b f}{N_b n_e}. \quad (2.36)$$

The detector efficiency is believed to be between 50-70%, though this number decreases with time as the MCP detector is “worn out”. Presently, ELISA is not equipped with

a current transformer as the one used at ASTRID, and the absolute ion current can therefore not be measured. If one wants to measure the absolute scattering cross-section, the ion current could possibly be deduced from the ion beam lifetime, which is reduced when electrons are turned on due to electron-ion interactions. Also, attempts have been made to estimate the total stored ion current from that which hits a Faraday cup right before the storage ring. Results from electron scattering on negative ions using ELISA and ETRAP will be presented in Chapter 5, but none of these results are calibrated on an absolute scale.

Trap mode

As the name of the ELISA electron target implies, ETRAP is also able to trap electrons in a potential centered on the axis of the ion beam. Radial confinement is achieved with the axial magnetic field, while longitudinal confinement is provided by two electrodes, which are ramped from ground to *e.g.* 100 V in order to trap the electron beam emitted and accelerated from the cathode. As in beam mode, the electrons will undergo cyclotron and magnetron motion, but the anisotropic energy distribution of the beam will quickly relax to a thermal energy distribution in trap mode. In the experiments presented in Chapter 5, only the beam mode of ETRAP has been employed, and details of the experimental procedures involved when operating in trap mode will not be included in this thesis.

2.4 Ion sources

Four different ion sources have been used to produce the results of this thesis. They will all be described below.

2.4.1 The Aarhus negative ion sputter source

A standard device for production of negative ions is the Middleton type sputter source, first described by Middleton as *a close to universal negative ion source* [44]. The source utilizes a beam of Cs^+ ions to sputter the desired beam material from a hollow cone.

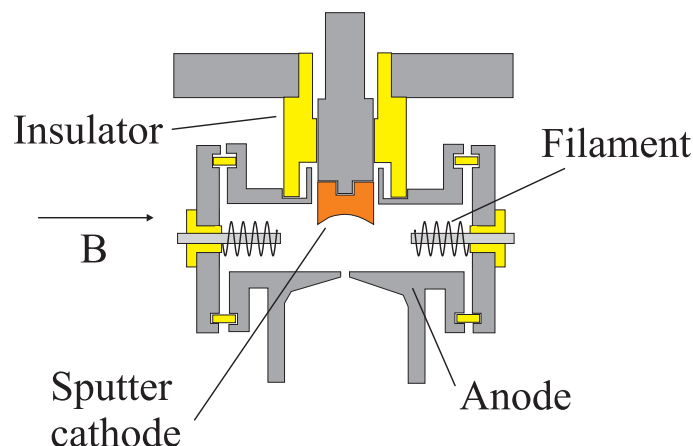


Figure 2.13: Schematic diagram of the discharge chamber of the cesium ion sputter source.

The advantages are manifold; the very versatile source delivers intense beams of a vast number of ion species from both solid and gaseous materials. Sample changing is easy and

the source will typically deliver a stable beam for hours, days and even weeks. Having been developed in Aarhus, the design of our sputter source (the Aarhus Negative Ion Source, ANIS, sketched in Fig. 2.13) is slightly different from Middleton's original source, but the main principles of operation are identical [45, 46, 47].

Cesium atoms are supplied from a small electric oven which evaporates the cesium (~ 10 mg/hr) into a small discharge chamber. Two heated filaments, carrying about 40 A of current, will emit energetic electrons that are further accelerated and guided by a transverse magnetic field into the discharge chamber where the cesium atoms of the source will be ionized. The Cs^+ ions are attracted by the negative sputter cathode (at typically -2 to -3 kV), and the resulting bombardment of the cathode will create free neutral atoms and ions. The cesium layer on the water cooled cathode will cause charge-transfer from cesium atoms to sputtered positive ions and neutrals, which thus increase the negative ion yield considerably [48]. During normal operating conditions, the electron-emitting filaments will heat the entire source to typically 100 - 150 °C which is enough to heat the cesium oven without heating currents.

After production, the negative ions will be repelled towards the extraction orifice by the cathode, which will further focus the ions due to the spherical shape of the cathode surface. By measuring the ion yield as a function of the distance between the sputter cathode and the extraction opening, a distinct maximum is found where the distance equals the radius of the cathode surface [45].

Some materials, *e.g.* carbonaceous ones like C_2H_6 gas, will contaminate the source so badly, that it will have an effect on future use of the source. This *memory effect* is generally expected to be small for sputter sources [49], but it can be of great importance when producing certain ions, and often a very thorough cleaning of the source will precede each employment of the source.

The stability of the extracted ion beam will normally be limited by the cesium oven, the durability of the filaments and the condition of the sputter cathode surface. As mentioned, the filaments will heat the entire source, including the cesium oven. If the filaments get too hot, all the cesium could quickly evaporate, leaving the source operating at reduced efficiency. The cesium has also been observed to completely cover the sputter cathode in a thick layer contaminated with various elements from the gas, thus reducing the efficiency of the sputter process. Further, when using carbonaceous materials the filaments will be badly corroded, and the succeeding increase in resistivity will prevent the passing of high enough currents required for proper operation. This can destroy the filaments within a few days of continuous operation.

The filaments can only be changed by taking the source completely apart, while the sputter cathode can be changed through a vacuum lock thus leaving the vacuum unaffected. The cesium oven can be removed and refilled without demounting the source, but not without breaching the vacuum.

The sputter ion source was used in experiments presented in Chapter 3.

2.4.2 Cold cathode ion source

A simple, yet quite effective, production method of ions consists of inducing an electrical discharge in a gas, which by nature will create high concentrations of ionized species that can be extracted from the discharge volume by the application of electromagnetic fields. This principle is implemented in a particularly simple ion source, which by our group is named the Cold Cathode Ion Source (CCIS). Contrary to *e.g.* the sputter source, the CCIS

does not contain a heated filament, and the absence of this allows the source to function at temperatures somewhat lower than those of the sputter source, hence the name. The source is a hollow-cathode glow discharge source, which consists of a glass cylinder closed in one end. Inside is placed two cylindrical stainless steel electrodes that are electrically isolated from each other. Both are connected with electrodes leading through the glass cylinder to an external current supply. At the open end of the glass cylinder, a stainless steel plate separates the high-pressure ion source from the vacuum of the accelerator onto which the source is mounted. A small orifice (~ 0.5 mm) allows for extraction of the ions produced in the discharge between the electrodes.

To confine the plasma tightly to the radial axis of the source, an extra metal tube may be inserted into the electrode closest to the extraction orifice. The diameter of this inner tube can be changed, with some control of the source operating conditions. Also, the size of the extraction orifice can be varied with even more influence on the operation. To further control the spatial extent of the plasma and the dynamics of the electrons, the source is positioned between the poles of an electromagnet which thus supplies a transverse magnetic field reducing the extraction of electrons during negative ion production. The magnetic field is optimized for maximum ion yield.

The source is evacuated and a controlled partial pressure of a desired gas can be supplied through a needle valve. A voltage of up to 650 V applied across the two electrodes will cause free electrons to accelerate towards the anode, creating electron-ion pairs on their way through collisions with neutrals. The ions generated this way will travel in the opposite direction, bombarding the cathode and thereby cause new electrons to be emitted. If the generation of electron-ion pairs is sufficient to make up for the loss of charged particles to the electrodes and to the chamber walls, a stable plasma is formed. The gas pressure must be within a certain range, however: at low pressures, the ionization process becomes ineffective because the probability for electron-neutral collisions is too small, whereas at high pressures elastic collisions prevent electrons from reaching energies high enough for ionization to occur. Typical discharge parameters are 650 V and 20-100 mA.

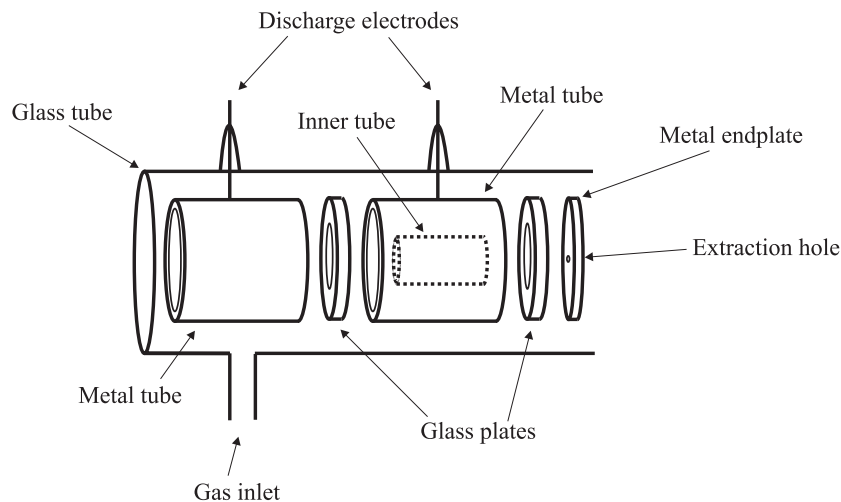


Figure 2.14: Glow discharge ion source. The ion source is a glass cylinder with two electrically isolated stainless steel electrodes. One electrode can be fitted with a coaxial inner electrode of smaller diameter for the purpose of tighter plasma confinement.

A list of ions produced in the CCIS is presented in Table 2.1.

The CCIS is a versatile source of both positive and negative ions. A great advantage of the CCIS over the sputter source is a much shorter start-up time; where the sputter source may require more than an hour before delivering a stable beam, ions can often be extracted from the CCIS within a few minutes and, indeed, pushing the voltage supply power button has even been observed to be sufficient. Further, the glass design makes it possible to see the plasma inside the source, a feature that has often served as an important diagnostics tool. A “good” plasma is typically a well confined, cylindrical plasma inside the small inner tube, right in front of the extraction orifice. Also, the color of the plasma is an indicator of the gas purity. If, for instance, one wishes to change the supplied gas from atmospheric air to pure oxygen, the plasma color can be seen to change from purple to bright white.

Ion	Gas supply	Current (nA)
O^-	O_2	200
O_2^-	Atm. air	100
O_3^-	O_2	4
NO_2^-	Atm. air	750
NO_3^-	Atm. air	250
SO_2^-	SO_2	110*
Cl^-	$CHCl_3$	50

Table 2.1: List of some of the ion currents extracted from the hollow-cathode glass ion source. *As discussed in section 3.3.6, the ion current measured at this mass-to-charge ratio could possibly be due to other ions than SO_2^- .

Another advantage is the possibility of a relatively long period of operation. When running the source on atmospheric air, the source can easily function uninterrupted for weeks. When running on other gases, the operation is only limited by the gas supply, which has to be changed regularly. Uninterrupted operation can still often occur on timescales of weeks. Some gases will contaminate the source, and this can cause the discharge to become unstable and finally impossible to sustain. This is particularly the case for any type of carbonaceous gas, like for instance CO_2 , and also for sulphur-containing gases. With gases of these types, the source will typically have to be dismantled and cleaned every few hours or days.

The source does, however, also display some disadvantages. Where the sputter source can create ions from solid materials, the CCIS is restricted to externally supplied gasses. Also, the sputter source will often deliver more intense beams of negative ions. The CCIS reaches operating temperatures far below those typical for the sputter source, but at high discharge currents, the temperatures can still rise above what the glass structure can withstand, and external convection cooling will normally have to be applied.

Further, the CCIS has proven to operate quite unstably when discharging in certain gasses, especially carbonaceous ones. When operating with carbon in the source, all metal surfaces of the source are quickly covered by vast amounts of carbon, and the electrodes are even observed to be badly corroded. The carbon attacks the metal in point discharges, the result of which can only be removed through mechanical grinding. These point discharges are observed in the source as small, but very bright, spots on the surfaces of electrodes.

This ion source was used in experiments presented in Chapters 3 and 5.

2.4.3 Nielsen type ion source

The Nielsen type ion source was developed in the 1950's [50, 51] by K. O. Nielsen in Copenhagen. The source consists of a heated filament placed in a discharge chamber surrounded by a solenoid, which provides an axial magnetic field. The filament has a negative voltage relative to the chamber walls, and thermally emitted electrons are thus accelerated from the filament, and under the combined influence of the electric and magnetic field, the result is oscillating electrons that cause ionization in the ambient gas.

The source is effective in creating positive ions, and it has also proved excellent in generating doubly-charged ions, for which it has been used in this thesis. The source is moreover fitted with an oven, which can be used to generate ions from a solid source material. The filament heats the entire discharge chamber, including the oven, to high temperatures, and this is sufficient to cause sublimation from many solid materials. In the present work, however, the source has only been operated on gases fed into the discharge chamber.

The ion source was used in experiments presented in Chapter 4.

2.4.4 Electrospray ionization

The previously described sources utilizes "hard" ionization methods, where ions are created using high voltage discharges and high temperature filaments. These methods are insufficient when transforming large organic molecules of interest to biology and medicine into gas-phase ions, the result being extensive decomposition of the molecular structure. In the last 30 years experimentalists have strived to develop more "soft" ionization methods, and the most successful of these is the electrospray ionization (ESI) method, mainly developed by J. B. Fenn¹¹ in the 1980's.

Initial experiments by the physicist John Zeleny in 1917 [52] preceded the first description by Malcolm Dole in 1968 [53] of the electrospray principle, including the charge residue model (CRM), which has survived as a main explanation for the enigmatic ESI process. This explanation is also presented below. The well-defined breakthrough of ESI came in the late 1980's [54], when John Fenn presented an identification of polypeptides and proteins of molecular weight of several thousands amu in mass spectrometer experiments. The findings were based on developments that had started in 1984 [55] in Fenn's laboratory, when electrospray and mass spectrometry were successfully combined for the first time.

Electrospray ionization generates ions directly from a solution by creating a fine spray of highly-charged droplets in the presence of a strong electric field (typically applying voltages of several kV). A dilute analyte solution flows through a small metal tube (or "needle") on the axis of a vacuum chamber mounted on an acceleration platform. A potential difference of several kilovolts between the needle and the chamber walls produces an intense electric field at the needle exit that disperses the emerging liquid into a fine spray of charged droplets¹².

As solution molecules evaporate from each droplets, the droplets quickly decrease in size thus increasing the electric charge density on its surface. The charge density increases until the so-called Rayleigh limit is reached at which the mutual Coulomb repulsion be-

¹¹For his work, Fenn was awarded the Nobel Prize in chemistry in 2002.

¹²The spray effect can actually be demonstrated by spraying water through a syringe with a high voltage applied to the needle. This creates a highly diverging spray of very small water droplets.

tween like charges exceeds the forces of the surface tension. The resulting instability, sometimes called a “Coulomb explosion” or “Rayleigh fission”, tears the droplet apart, producing charged daughter droplets that also evaporate. This sequence of events repeats until the radius of a daughter droplet becomes small enough that the field due to the surface charge density is strong enough to desorb ions from the droplet into the ambient gas. Freely hovering analyte ions remain, as sketched in Fig. 2.15.

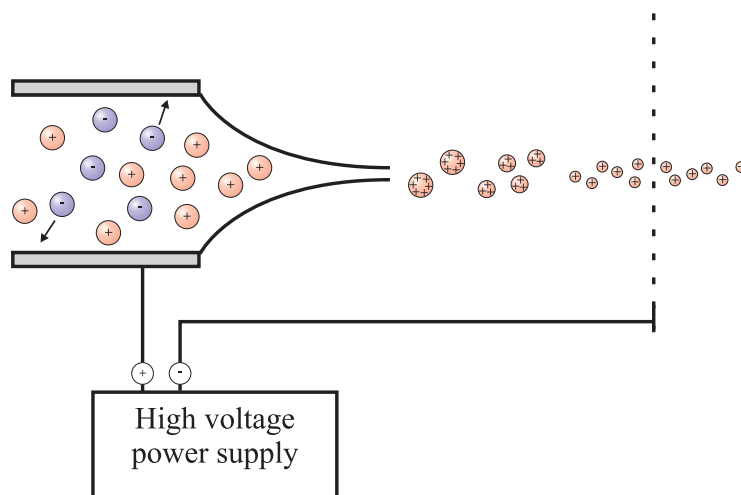


Figure 2.15: Schematic drawing of the electrospray ionization principle. A solution of the molecules that are to be ionized flows through a metal needle lifted to a high electrostatic potential. The droplets dispensed from the needle will be charged, and a combination of evaporation and Coulomb explosion will generate smaller and smaller charged droplets until freely hovering molecular ions remain.

Vaporization of these charged droplets results in the production of singly or multiply-charged gaseous ions. The number of charges retained by an analyte can depend on such factors as the composition and pH of the electrosprayed solvent as well as the chemical nature of the sample. For small molecules (<2000 amu) ESI typically generates singly or doubly-charged ions, while for large molecules (>2000 amu) the ESI process typically gives rise to a series of multiply-charged species.

As mentioned, ESI can readily ionize very large and complex species such as peptides, proteins, nucleic acids and carbohydrates that play a vital role in living systems. This ionization is not possible with other ion sources mentioned in this chapter. With a proper selection of conditions, ESI can be the least invasive of all ionization methods, even allowing studies of molecular complexes that only have weak non-covalent interactions, such as protein-protein, enzyme-substrate or protein-ligand complexes.

The ESI technique has further proved invaluable in mass spectrometry, where molecules of substantial mass but a low degree of ionization cannot be analyzed in an ordinary mass spectrometer, since the applied fields are too weak to deflect the heavy particles sufficiently. Using ESI sources, the macro-molecules may take on a large number of positive charges, and the mass-to-charge ratio thus becomes small enough to allow the substances to be analyzed. Another advantage is that the same molecule causes a series of peaks, since each can take up a varying number of charges. While this complicates the pattern, at first confusing researchers, it also gives information that makes identification easier, since this very complexity adds to the information and can be used to an advantage to

improve the accuracy of the molecular-weight determination.

The main disadvantage of ESI is perhaps the low ion currents that can be extracted. Typical numbers of extracted ions are $\sim 10^6$ ions/s [56], and for this reason the Aarhus ESI source is fitted with an ion trap, which utilizes a helium buffer gas to collisionally dampen the ions that are then confined by an RF field in the central trap region. By accumulating ions before *e.g.* injection them into a storage ring, high enough ion currents can be produced to make experiments feasible.

Another disadvantage of ESI is that the solution-filled syringe, which feeds the electrospray process, is only of finite capacity. The spray rate is one of the many variables of operation for this source, but typical parameters will require interrupting the experiment and refilling the syringe every hour, whereas *e.g.* the CCIS source can operate for days and weeks without interruption.

The electrospray process is governed by a large number of chemical and physical parameters that together determine the quality of the process, and although ESI is now in daily use all over the world, its component processes and mechanisms, especially the dispersion of the sample liquid into charged droplets and the formation of gas phase ions from those droplets, are poorly understood. Both of these processes are very complex, depending strongly on an intricate interplay between variables such as flow rate, applied field and solution properties including conductivity, surface tension concentration, dielectric constant and viscosity, as well as the structure and conformation of the analyte molecules. A thorough discussion about the electrospray mechanism can be found in Ref. [57].

The ESI source was used in experiments presented in Chapter 5.

2.4.5 Comparison and diagnostics

As mentioned, one particular ion source cannot produce all desired ions, and each source has its own advantages and disadvantages. In Table 2.2, the previously described ion sources are compared.

	Sputter	CCIS	Nielsen	ESI
Ion charge	neg.	pos./neg.	pos./neg.	pos./neg.
Source material	solid/gas	gas	solid/gas	solution
Typical currents	medium/high	medium	medium/high	low
Limitations	filament and cesium	electrode contamination	filament	spray volume

Table 2.2: Comparison of the four ion sources utilized in the present work showing the ion charges, source materials from which ions can be produced, a relative comparison of typical ion currents and the parameters that normally limit the operational period.

From the descriptions of the ion sources, it is clear that one cannot easily create one - and just one - ion species from a given source. Many ions are created simultaneously, as is the case in *e.g.* an electrical discharge used in many ion sources. How does one select the desired ion? This is naturally a question of utmost importance to the experiment.

The ion selection employed here is the standard method used since the invention of mass spectrometers, *i.e.* a magnetic separation of the desired ion beam. Ion source outputs are accelerated and directed through a vertical magnetic field supplied by a so-called “analysis magnet”. As described by Eq. 2.29, this deflects the ion beam in a way that

sorts the individual constituents of the ion beam according to their mass-to-charge ratio. This is quite often sufficient when selecting ions for an experiment, but when working with molecular ion sources, it is crucial to double-check that the correct ion has been selected. This is due to the fact that ion sources normally exhibit memory effects, where contaminations from previous experiments have remained in the ion source. Complicated combinations of unidentified basic elements may thus be present in the extracted ion beam. During my work, I have had to employ several ion beam diagnostics techniques, as the following two examples will describe.

After ions have been injected into ASTRID, the resulting SSD pulse height spectrum (see *e.g.* Fig. 2.9) can be analyzed for neutral collision fragments. Molecular ions will break up into smaller molecular and atomic fragments, and these can be identified according to their mass. In the case of CO_2^{2+} , the results from which will be presented in Chapter 4, the first SSD spectrum clearly showed an impurity in the beam (see Fig. 2.16). The exact identity of this impurity was never revealed, but memory effects from previous experiments with that particular ion source is an obvious explanation of the presence of the impurity.

After changing to a new ion source the impurity disappeared, and we then believed to have a pure CO_2^{2+} beam. One notices (Fig. 2.16) that the relative intensities of the different peaks changed with the disappearance of the impurity, another sign that the ion beam constituents had changed with the change of ion source. One can thus conclude that ASTRID is a quite good diagnostics tool for the purpose of identifying the ionic constituents of an ion beam.

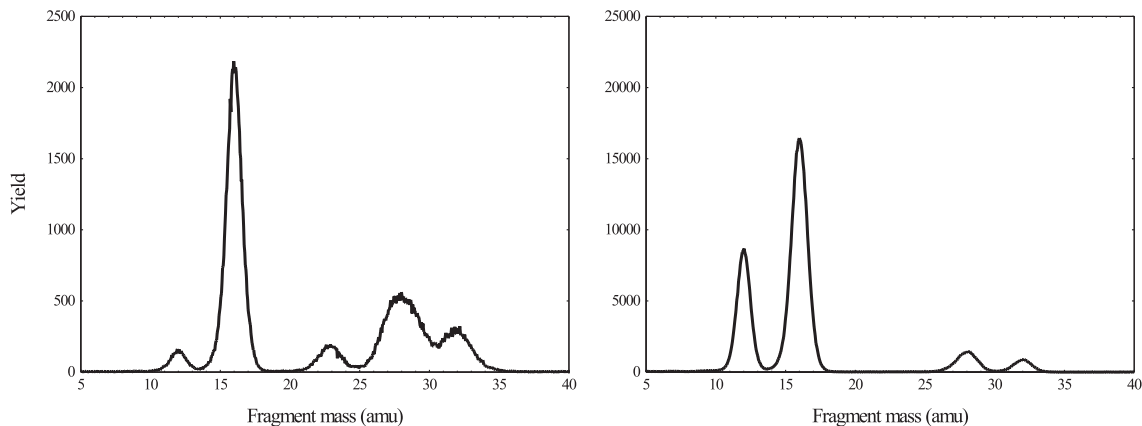


Figure 2.16: Comparison of two SSD pulse height spectra from a CO_2^{2+} experiment. The left spectrum contains an impurity, which has been removed in the right spectrum. The peaks in the right spectrum corresponds to a C atom, an O atom, a (C + O) cluster and an (O + O) cluster.

On several different occasions, we have been interested in studying electron impact upon singly-charged ions of mass 26 amu. One of these ions was the vinylidene anion H_2CC^- , which has previously been studied at ELISA [38]. In that experiment H_2CC^- ions were produced in a sputter source containing an iron oxide cathode and fed with a C_2H_4 gas. The extracted ions were stored in ELISA, and the decay rate of the ions was measured as a function of the background pressure in the ring. In an attempt to perform an electron scattering experiment on the vinylidene anion at ASTRID, we tried to produce the ion using the same ion source type. The SSD spectrum showed then that the extracted ion beam did *not* consist of H_2CC^- ions.

We decided to test the sputter source by another method, utilizing the Aarhus tandem van de Graaff accelerator. The tandem accelerates negative ions by charging a high voltage platform to *e.g.* 3 million volts. The negative ions are accelerated from the source to the platform, in which an argon stripper gas will convert the negative ions to singly and multiply-charged positives ions and at the same time fragmentize most of the molecular species in the ion beam. The positive ions are then even further accelerated by the now repulsive high voltage platform, to energies of $(q + 1)$ times the high voltage platform¹³ of 3 MeV. The ion current can be measured in several Faraday cups, both in the low (LE) and high energy (HE) regions, and also after an analysis magnet (image cup). All this is sketched in Fig. 2.17.

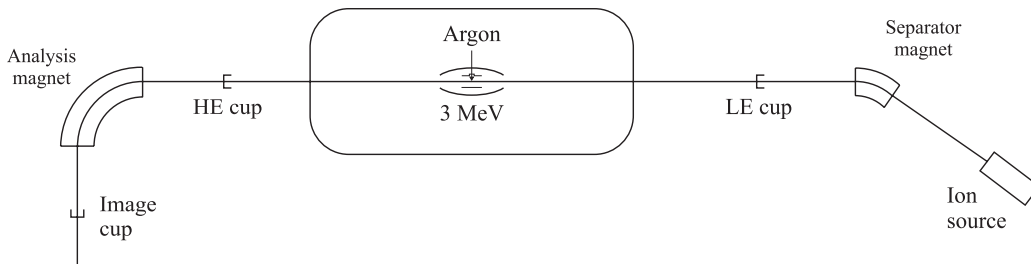


Figure 2.17: Schematic diagram of the Aarhus tandem accelerator.

The sputter source was cleaned and mounted with an iron oxide cathode and a C_2H_4 gas bottle connected, *i.e.* just as the source was used at the ELISA experiment. An ion beam of mass 26 amu was produced, and the beam was mass analyzed after passing through the tandem stripper gas. The magnetic field separates the fragments according to their mass to charge ratio, but the particular nature of the tandem acceleration results in the following relation:

$$B = \sqrt{c_1 \cdot \left(\frac{M_{frag}}{Q}\right)^2 + c_2 \cdot \left(\frac{M_{frag}}{Q}\right)}, \quad (2.37)$$

where B is the magnetic field required to detect a particular fragment, M_{frag} and Q are the mass and charge of the fragment and c_1 and c_2 are constants depending on the high voltage platform, the energy of the extracted ions, the radius of curvature in the magnet and the mass of the ions extracted from the source. The result showed a high content of nitrogen, and it was concluded that the CN^- ion was the most probable candidate for the true identity of the mass 26 peak (Fig. 2.18, left).

The source was recleaned and a new and cleaner supply of C_4H_4 gas was connected. This spectrum (Fig. 2.18, right) indicated that the beam was a complicated mixture of *e.g.* H_2CC^- , BO^- and CN^- ions, and we thus concluded that the vinylidene anion *could* be produced in the cesium sputter source, though it was quite difficult to achieve a pure beam of that ion.

This result is in conflict with the test previously performed with the sputter source at the tandem, a test that was done prior to the ELISA measurement, and which yielded only small traces of possible nitrogen contamination. Moreover, a test had been performed at ELISA where the decay curves of the mass 26 beam was compared with a pure CN^- beam prepared from a sputter cathode containing CN. This test showed a difference in

¹³Plus an additional 100 keV acquired during the initial acceleration.

decay rates, confirming that the mass 26 beam did not contain significant amounts of CN^- . Further, the measurement at ELISA yielded a lifetime of the negative vinylidene ion of $\tau \sim 110$ s, which is in agreement with unpublished data of $\tau > 100$ s.

It is thus apparent that the exact same type of ion source with the same settings is capable of producing two completely different ion beams, and this again stresses the importance of identifying the extracted ions used in an experiment.

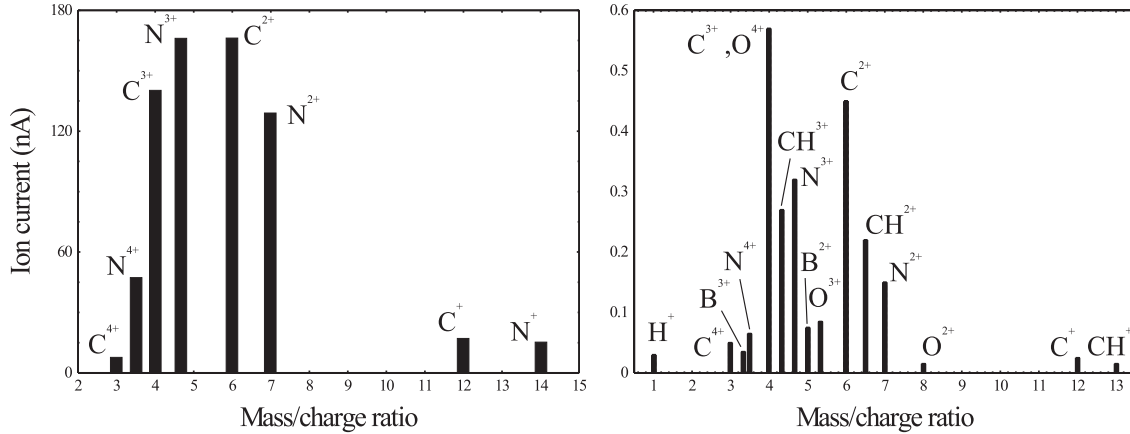


Figure 2.18: A scan of the tandem analysis magnet showing several charge states ($q = 1, \dots, 4$) of various fragments. The two spectra show two different modes of operation for the same ion source. The left spectrum is believed to identify an ion beam primarily consisting of CN^- , while the right spectrum indicates that the beam is a mixture of CN^- , BO^- and H_2CC^- .

2.5 Conclusion

This chapter has presented all the experimental equipment that forms the basis of the present work. The two storage rings ASTRID and ELISA have been described, and so have the ion sources that are used to create the ions of interest. Moreover, the experimental procedures involved when one wishes to measure electron-ion collision cross-sections are explained. In short, it should now be clear how ions are produced, selected and identified, stored and collided with well-defined beams of electrons, and how the collision cross-sections are derived from measurable quantities. In the following chapters, results using these experimental tools will be presented, and a few extra details will be added to form a more complete picture about the experimental procedures.

Chapter 3

Electron scattering on negative ions

This chapter describes experiments with electron scattering on negatively charged ions performed at the heavy-ion storage ring ASTRID. A number of different ions have been studied. For all ions, the relative cross-section has been measured, and for ions produced in sufficient quantities, the cross-sections have been put on an absolute scale. Branching ratios for molecular break-up have been determined for polyatomic ions. Also in this chapter, descriptions are presented of the experimental procedures involved when a measured cross-section is put on an absolute scale and when reaction channel branching ratios are determined.

3.1 Introduction

The present study was initiated to better understand the collision dynamics involved when free electrons scatter on negatively charged ions, or anions, an important reaction in a vast number of plasma-related situations. We address the following questions:

- What is the effective threshold for electron-impact detachment (release of a target electron)?
- Is detachment accompanied by substantial dissociation, and if so into which dissociation channels?
- May the incoming electron be captured and hence provide formation of a doubly-charged negative ion (dianion)?

3.1.1 General introduction

The structure and properties of negative ions differ significantly from their neutral and positive counterparts, which is due to the differences in the respective binding potentials. Where the long-range Coulomb interaction dominates neutral and positive species, the extra electron in anions is bound by an induced short-range dipole interaction. Negative ions play an important role in weakly ionized gases, and many types of plasma can only be modeled accurately if negative ions are included. A typical example of this is the presence of H^- in the solar photosphere, where the anion controls the emission of the Sun in the optical part of the spectrum, and indeed, H^- is the predominant source of opacity in most stellar atmospheres. Also, in the atmosphere of Earth, the negative charge at altitudes up to 70 km is carried mainly by negative ions [58]. Plasma properties are strongly

dependent on whether the negative charges are in the form of highly mobile electrons or slowly moving anions. In order to correctly model a plasma it is therefore important to know the energy-dependent cross-sections for the various collisional processes involving anions.

Negative ions provide a unique test bench in the ongoing development of atomic and molecular theory. Due to the high degree of electron correlation in these systems, they are quite sensitive to the various approximations applied when calculating their structural and dynamical properties, and available experimental results are essential to test the quality of different theoretical models.

The binding energy of the extra electron of an anion is called the *electron affinity*, abbreviated EA. An atom or molecule with a positive EA can thus bind an extra electron, while species like the noble gases with negative electron affinities are unable to form negative ions. One of the most studied anions is that of hydrogen, which is the only atomic system, whose EA is more precisely known theoretically than experimentally [59]. This is in spite of massive experimental investigation motivated by the fact that the ion is the most simple of all anions and that it is an important constituent of most astrophysical plasma.

Also, the generation of negatively charged atoms and molecules is of utmost relevance for accelerator mass spectrometry (used for *e.g.* carbon-14 dating) where the production of an abundant flux of stable anions is a prerequisite for the ultrahigh sensitivity of this technique [60, 61, 62].

While singly-charged negative ions in the gas-phase have been the center of attention for most experimental and theoretical work over the past decades, the existence of free doubly or multiply-charged negative ions, in particular those of small systems, has remained a curiosity and a matter of some controversy. Lately, doubly-charged anions in the gas-phase have attracted considerable experimental and theoretical attention, an interest stimulated in part by the development of the tandem accelerator, where doubly-charged negative ions would increase the final ion kinetic energy significantly without increasing the standoff voltage of the accelerator. Recent experimental and quantum mechanical studies show that multiply-charged negative ions of small molecules and clusters can exist as isolated entities, and it is yet an unanswered question how small a molecular system may be while still supporting two extra electrons.

3.1.2 Historical overview

Negative ions were first observed in mass spectrometers invented by J. J. Thomson in the first two decades of the twentieth century. Anions like O^- , H^- and C^- were identified by Thomson and his assistant Francis W. Aston during the 1910's [63, 64]. It was already noticed by Thomson [63] that negative ions of He, N, Ne, Ar, Kr, Xe and Hg could not be observed, even though the positive ions of these elements were present in the spectrometer. Thomson further noticed a lack of negatively charged molecules, and he speculated that this was caused by a very weak binding of the electrons. He did, however, observe some molecular anions, *e.g.* C_2^- , C_3^- and O_2^- [63].

Most of the information about the structure of negatively charged ions has been obtained through photodetachment experiments. These investigations were initiated by Lewis Branscomb in the 1950's [65, 66, 67] using incandescent light sources, but it was Lineberger and co-workers in the 1970's [68] who performed the first systematic studies using the newly invented laser technology. The first experiments involving scattering on

negative gas-phase ions with electrons of a well-defined energy were performed in the 1960's [69]. The first experiment studied the detachment reaction:



with hydrogen as the involved atom ($X=H$), and it was initiated due to the importance of H^- in astrophysics. Other experiments on H^- were carried out in the following years [70, 71, 72], and studies of several other systems as C^- [73], O^- [71, 73] and F^- [74] soon followed.

In the early 1990's, studies of negative ions utilizing heavy-ion storage rings were commenced in Århus [75], and a few years later electron scattering on atomic anions was studied in Århus [76] as well as in Japan [77]. A similar research program was later initiated at the CRYRING storage ring in Stockholm [78]. The first experiments were performed on negative atomic ions [76, 77, 78, 79], but soon followed diatomic anions [80] and small polyatomic anions [81, 82].

Many researchers have searched for stable doubly-charged negative ions. Several times during the past 40 years, discovery of an atomic dianion has been claimed, but none have been confirmed [83, 84]. Today, the non-existence of bound atomic dianions is a well-established fact. The first doubly-charged negative ion to be observed experimentally in the gas phase was the dianion of Benzol[cd]-pyrene-6-one, a large organic ketone seen in a mass spectrum in 1969 [85]. Indeed, all dianions observed in the following decades were moderate-size molecules [83]. Not until 1990 were the first dianions consisting of fewer than twenty atoms discovered, *e.g.* carbon clusters as small as C_7^{2-} [86]. Theoretical attempts to understand the stability of the dianions already discovered and directed towards finding ever smaller molecules capable of supporting two extra electrons soon followed. A summary of the status of these calculations is given in Ref. [87].

The smallest molecular dianions calculated to be stable are alkali-metal halides of the form MX_3^{2-} ($M = Li, Na$ or K ; $X = F$ or Cl) [88, 89] and the alkaline-earth-metal tetrahalides, MX_4^{2-} ($M = Be, Mg$ or Ca ; $X = F$ or Cl) [90]. In both cases, the electron detachment energies are predicted to be greater than 1.5 eV, and indeed BeF_4^{2-} and MgF_4^{2-} ions were detected in the output of a cesium sputter source and confirmed in a tandem accelerator [83] using a technique quite similar to the one described in section 2.4.5. These are the smallest stable dianions observed so far [91], and today it is generally believed that sputter sources are very effective in producing small dianions, in fact all small dianions to date have been produced in cesium sputter sources.

Excellent reviews of the history of dianion research can be found in Refs. [59, 92] and references therein.

3.2 Theoretical overview

Negative ions form systems of tremendous theoretical challenge. Although the ions are identical to neutral atoms and positive ions in terms of the constituent particles and internal interactions, their properties are considerably different and correspondingly more difficult to describe theoretically. Experimental studies of negative ions thus serve as an important test of theoretical models.

The difficulties arise due to the significance of the relatively large electron-electron correlation present in these systems. The formation of a negative ion requires an electron to be attached to a neutral particle, a task that initially seems quite troublesome. About

80% of all the basic elements are, however, capable of forming negative ions, which is achieved by the induced dipole moment created by the rearrangement of the electrons in the field of the external electron. The extra electron is thus strongly correlated to the indigenous electrons, a situation difficult to describe in theory. The problem becomes immensely more complicated when considering dianions.

Not only are negative ions themselves difficult to describe theoretically, but also the case of electron scattering on negative ions leading to the detachment process (Eq. 3.1) is especially difficult to model due to the necessity for describing two outgoing continuum electrons. Theoretical studies have struggled with the large amount of correlation between these two free electrons, but recently several authors like Robicheaux [93, 94], Rost [95], Lin [96] and Pindzola [97, 98] have developed theory that accurately describes scattering on weakly bound negative ions.

The measured electron-impact detachment cross-sections have also with success been compared to a classical “reaction zone” model [76] where it is assumed that the scattering electron experiences a purely repulsive Coulomb potential and that detachment takes place with a constant probability p if the electron gets inside a certain reaction radius R . The distance of closest approach, $D(\rho)$, can be written as a function of the impact parameter, ρ , and the energy of the incoming electron, E :

$$D(\rho) = \frac{1}{2}D_0 + \sqrt{\left(\frac{1}{2}D_0\right)^2 + \rho^2}, \quad (3.2)$$

where $D_0 = 1/E$ in atomic units. The requirement that the closest approach is within the reaction zone is equivalent to demanding that the impact parameter is less than $\rho_0 = \sqrt{R^2 - RD_0}$. All this yields a smooth non-resonant detachment cross-section with an onset above some threshold $E_{th} = 1/R$:

$$\sigma_{NR} = 2\pi \int_0^\infty \rho d\rho \times \begin{cases} p & , \text{ for } \rho \leq \rho_0 \\ 0 & , \text{ for } \rho > \rho_0 \end{cases} \quad (3.3)$$

$$= p\pi R^2 \times \max\left[0; 1 - \frac{E_{th}}{E}\right]. \quad (3.4)$$

It is important to note that this model does not include any contributions from electrons tunneling out through the potential barrier, which is possible when the incoming electron perturbs the potential experienced by the target electron in the anion. However, the model does show quite good agreement with all detachment cross-sections measured so far at storage rings (see *e.g.* Refs. [76, 80, 99]), though these typically do exhibit some tunneling contribution.

The effective threshold energy E_{th} may be estimated using a classical over-the-barrier detachment model, where the binding force of a short-range r^{-4} potential (characteristic of the induced dipole interaction) is equated with the perturbing force of the incoming electron. Consider an electron bound in an anion by a simple one-dimensional binding potential:

$$V_b(r) = \frac{-E_b}{1 + (r/d)^4}, \quad (3.5)$$

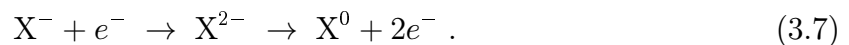
where d is a measure of the potential width. The electron will then experience a binding force of $F = -dV_b/dr$, and if an incoming electron scatters on the anion, the bound

electron will feel an additional perturbing Coulomb force of $1/r^2$ (in atomic units). The maximum perturbing force is experienced at the distance of closest approach between the anion and the incoming electron, $r_{min} = 1/E_0$, where E_0 is the initial energy of the incoming electron. The detachment threshold can now be estimated by balancing the maximum binding force with the maximum perturbing force, $F_b^{max} = E_{th}^2$:

$$E_{th} \approx \sqrt{\frac{EA}{d}} = 2^{1/4} (EA)^{3/4} , \quad (3.6)$$

where the width of the anion binding potential scales with the electron affinity as [100] $d \sim 1/\sqrt{2EA}$. This very simple model will later be compared to the detachment results of this thesis.

When scattering on an anion, the incoming electron could be captured into a state of the doubly-charged negative ion with subsequent decay and emission of two electrons:



When this reaction occurs in small anions, the dianion is too short-lived to be observed directly, but its presence can be extracted from the scattering cross-section, where a resonance structure will appear [101]. Because small dianions have very short lifetimes, τ , the resonances are expected to be of substantial widths ($\Delta E \approx \hbar/\tau$). A wide resonance structure in the cross-section is therefore a telltale sign that a short-lived dianion state has been created. In practice, the resonances are slightly widened by the finite velocity distribution of the electrons, and the measured width thus gives a lower limit of the resonance state lifetime.

If an electron is detached from a neutral atom or molecule, a positively charged ion is formed, and the interaction between the outgoing electron and the residual cation is attractive due to their Coulomb attraction. Detachment of a singly-charged anion results in an electron and a residual neutral system, whose long-range interactions are usually weak but also mainly attractive in nature. The situation is different for detachment of multiply-charged anions: after detachment, the residual system is still negatively charged, and the long-range interaction between the outgoing electron and the system is dominated by the electrostatic Coulomb *repulsion*. Combining this long-range electrostatic repulsion with the short-range binding potential of the electron, a repulsive Coulomb barrier (RCB) emerges. This barrier has to be surmounted by the outgoing electron during its detachment process¹, or in the case of scattering, by the incoming electron during resonance state population. This conquest of the potential barrier is possible through quantum mechanical tunneling.

The RCB, which is treated thoroughly in *e.g.* Ref. [102], is very difficult to calculate exactly, but a qualitative picture can be expounded: apart from the repulsive $1/r$ Coulomb potential seen at large distances, the electron additionally sees a repulsive centrifugal term $l(l+1)/2r^2$ (where l is the angular momentum of the free electron) and at short distances within the core region some effective attraction. The situation is depicted for scattering on NO_2^- in Fig. 3.1 for *s* ($l = 0$) and *p* ($l = 1$) partial wave scattering. Two resonance states are included in the figure.

From the figure, one can explain why some ions do not exhibit a resonance at the ground state energy: if the barrier is too thick, the incoming electron will not be able to

¹The situation is quite like the case of nuclear α -particle emission, though the interactions and energy scales are different.

penetrate it, and actual formation of the dianion state is not achieved. At higher energies, the barrier is less impervious, and possible excited states of the dianion could be detectable while leaving the ground state concealed. As Fig. 3.1 shows, the high energy resonance state (E_2) cannot be supported without the centrifugal contribution. At least one unit of angular momentum is required, though higher partial waves can also contribute. If two resonances belonging to the same partial wave exist, we would expect a significant difference in the lifetime since the low-energy resonance then is associated with a much smaller tunneling probability than the high-energy resonance.

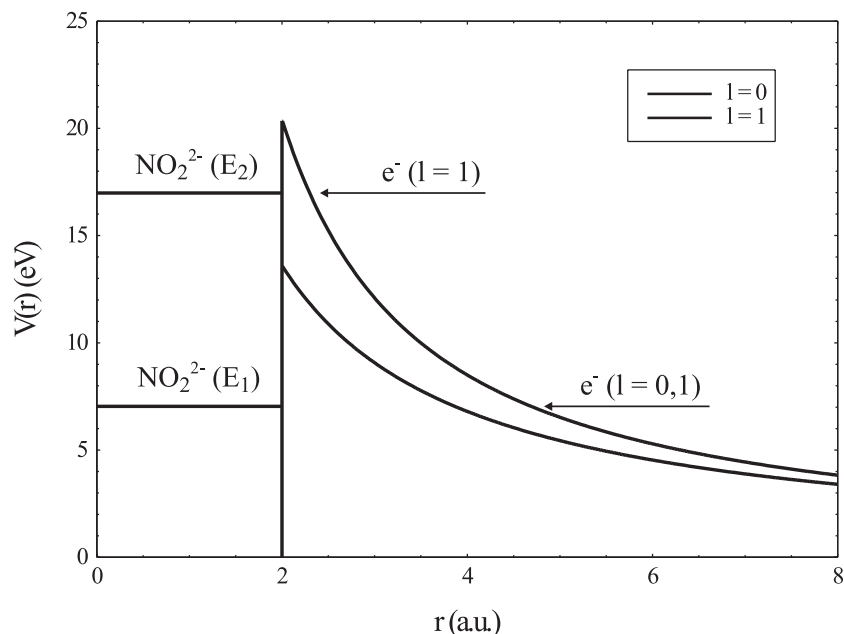


Figure 3.1: Schematic diagram of electrons scattering on an anion, in this case NO_2^- with two dianion states included. The potential energy is sketched as a function of the electron-anion distance.

With the strong internal Coulomb repulsion present in dianions, small molecular dianions are often highly unstable with lifetimes in the femtosecond range. Larger molecules, like hydrocarbons and polypeptides, may however support several charges due to their ability to spatially separate the extra charges. Short-lived dianion states may, as mentioned, be observable in electron scattering experiments, where the states may appear as wide resonances in the reaction cross-section. These resonances can be clearly seen as Lorentzian resonances superimposed on the non-resonant contribution as described by the classical scattering theory (Eq. 3.4). Electron scattering in storage ring experiments have within the last 10 years searched for [76, 79] and found resonance structures in the scattering cross-sections of several ions, *e.g.* C_2^- [80, 103, 104], B_2^- [80, 104], BN^- [80], NO_2^- [81], CN^- [105, 106], and C_4^- [82, 107].

To calculate the ground-state energy of a doubly-charged negative ion, we have applied the GAUSSIAN-98 program [108]. The program is fed with an initial geometrical configuration of the ion of interest, and through an iterative procedure, the molecular energy is calculated for the dianion. Furthermore, the energy gradient serves as a means of optimizing the geometrical structure, while the second derivative of the energy gives information on the nuclear vibrations. The calculations are performed both for the anion and the dianion. The predicted ground-state energy of the dianion can be compared to

observed resonance positions, which thus allows one to distinguish between ground-state and excited-state resonances. Table 3.1 summarizes the binding energies of some of the anions and dianions investigated in this thesis.

X	EA(X)	EA(X)	EA(X ⁻)
	[eV] Calc.	[eV] Exp.	[eV] Calc.
BO	2.5	2.51	-6.0
CN	3.8	3.86	-6.5
NO ₂	2.2	2.27	-6.8
NO ₃	3.9	3.94	-6.1
O ₃	2.7	2.10	-5.6
SO ₂	1.5	1.11	-5.5

Table 3.1: Table showing (adiabatic) electron affinities for neutrals (GAUSSIAN-98 calculation and experimental) and for negative ions (GAUSSIAN-98 calculation only).

3.3 Experimental results

As a PhD student, I have participated in many experiments involving electron scattering on negative ions, the results of which are presented in the following sections. The electron-impact cross-sections are compared to Eq. 3.4, and the detachment thresholds are compared to Eq. 3.6.

3.3.1 S⁻ and Cl⁻

Two negative atomic ions, S⁻ and Cl⁻, have been investigated in the present work. In both cases, the main purpose of the experiment has been to determine the detachment threshold, and we have thus only measured relative detachment cross-sections.

One of the first atomic electron affinities determined in laser photodetachment experiments was that of sulphur [109], which has an affinity of 2.077 eV [110]. Of all the basic elements, chlorine has the highest electron affinity (3.613 eV [111]), and the threshold would thus prove a good test of the model in Eq. 3.6. The Cl⁻ ion has previously been studied at CRYRING [112], an experiment that yielded a threshold of 10.1 eV. This is about 3 eV too high for it to agree with our classical detachment prediction (Eq. 3.6), and we thus decided to measure the threshold at ASTRID in order to compare with the Swedish result.

The S⁻ ion was produced in the cesium sputter source fitted with a cathode containing the sulphur isotope ³⁴S. This was chosen in order to avoid contamination from O₂⁻ ions, since the naturally most abundant isotope of sulphur, ³²S, has the same mass as molecular oxygen.

A current of about 500 nA was extracted from the source, pre-accelerated to 150 keV and stored in ASTRID, where it was further accelerated to 3.683 MeV. The lifetime of the beam was 2.3 s, and a clear peak corresponding to neutral S atoms could be observed in the pulse height spectrum of the SSD. The relative detachment cross-section was measured in the range from 0 to about 40 eV (see Fig. 3.2).

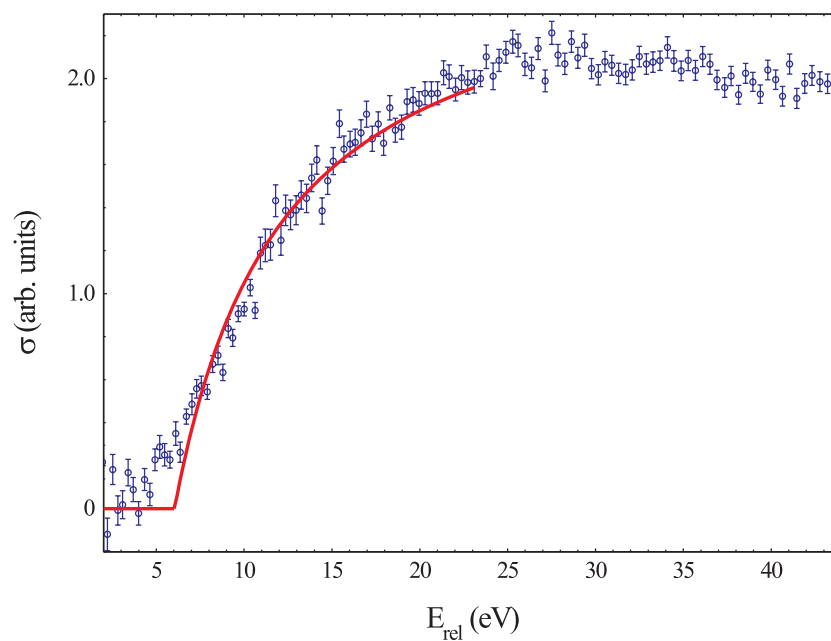


Figure 3.2: The measured S^- detachment cross-section compared to the non-resonant model of Eq. 3.4.

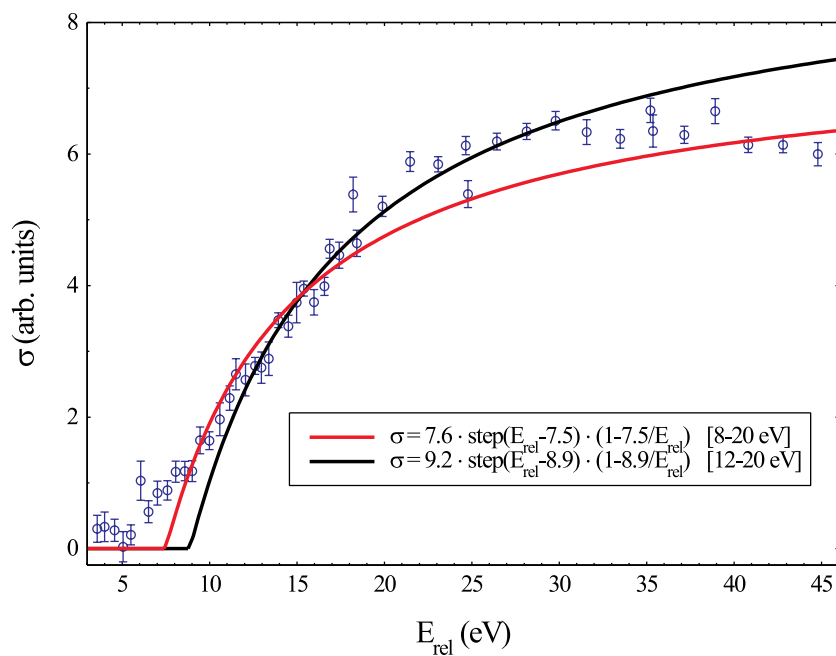


Figure 3.3: The Cl^- detachment cross-section compared to two different fits to the non-resonant model of Eq. 3.4.

The detachment cross-section exhibits a smooth threshold near 5 eV, a featureless increase up to about 25-30 eV, from where it begins to decrease slowly again. In the interval from 0 to 23 eV, the cross-section has been fitted with the non-resonant model of Eq. 3.4, which is in good agreement, although some tunneling contribution influences the threshold region. The threshold is found to be 6.0 eV, which agrees well with the prediction of Eq. 3.6. The S^{2-} dianion is known to be stable in both solid state and solution [113], but the in gas-phase it is very unstable. A low-energy resonance state of this ion has been predicted to exist [114], but the existence cannot be proved or disproved due to the quality of the present data.

Chlorine has four naturally occurring isotopes of which ^{35}Cl and ^{37}Cl are the most abundant, constituting 94.9% and 4.3%, respectively, of all natural chlorine. To avoid any contamination from water clusters like $\text{OH}^-(\text{H}_2\text{O})$ of mass 35 amu, the ^{37}Cl isotope was chosen for the experiment. The ion was produced in the hollow-anode CCIS source discharging in atmospheric air seeded with a small amount of chloroform (CHCl_3). About 50 nA of ion current was extracted and stored at 3.308 MeV in ASTRID.

The relative detachment cross-section can be seen in Fig. 3.3 in the interval from 0 to about 45 eV. It opens up just above 5 eV and then increases smoothly to about 30-35 eV, from where it slowly decreases. The model of Eq. 3.4 has been fitted to two different energy intervals of the experimental data.

One fit is to the data between 8 and 20 eV, which yields a threshold of 7.5 eV. Another fit to the data from 12 to 20 eV yields a higher threshold of 8.9 eV, and this fit follows the data more closely in a larger energy interval, but it also leaves a large tunneling contribution. The Swedish data are fitted to an energy interval from 10 to 30 eV, which explains the large discrepancies between the threshold value results, since the threshold is highly dependent on the energy region chosen for the fit. This is not always the case for other ions, but the Cl^- ion appears to exhibit a somewhat larger tunneling contribution than many previously investigated systems. We believe that it is quite difficult to derive exact quantitative requirements for the energy interval to be chosen for the fitting procedure, and instead we interpret the diverging results as a measure of the uncertainty on the threshold value.

3.3.2 CN^- and BO^-

CN^- and BO^- are isoelectronic anions, both molecules of $(5\sigma)^2(1\pi)^4$ electron configuration. Electron scattering on the two ions can thus give important information on the circumstances for resonances to appear. Both ions were produced in the ANIS sputter source running on sputter cathodes containing carbon and boron-oxide, respectively. Currents of several μA were extracted. The detachment cross-sections were measured for both ions, and the ion currents were intense enough for absolute measurements to be made.

After a relative cross-section had been measured in the entire energy range, the electron cooler was set to a relative energy of 30 eV, and the stored ion current was measured simultaneously with the neutral particle signal. The current was measured with a beam charge monitor² (BCM) from Bergoz [115] capable of measuring ion currents down to about 10-50 nA with a resolution below 10 nA. The resultant signal minus background and absolute ion current is depicted in Fig. 3.4, and with these measured values of N_s , N_b and N_{ion} , the absolute cross-section can be calculated from Eq. 2.25.

²This is the current transformer described on page 21.

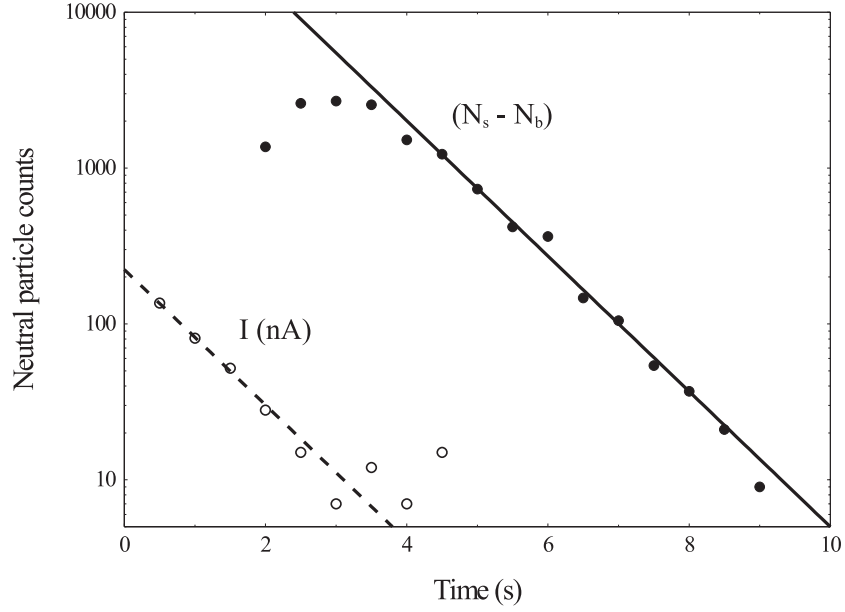


Figure 3.4: Detector count rate ($N_s - N_b$) and ion current (I) as a function of time measured for CN^- . The timescale is relative to the measurement start, *i.e.* after injection and acceleration. The data were recorded at a relative energy of 30 eV, an electron current of 3.5 mA and a corresponding electron density of $7 \times 10^6 \text{ cm}^{-3}$.

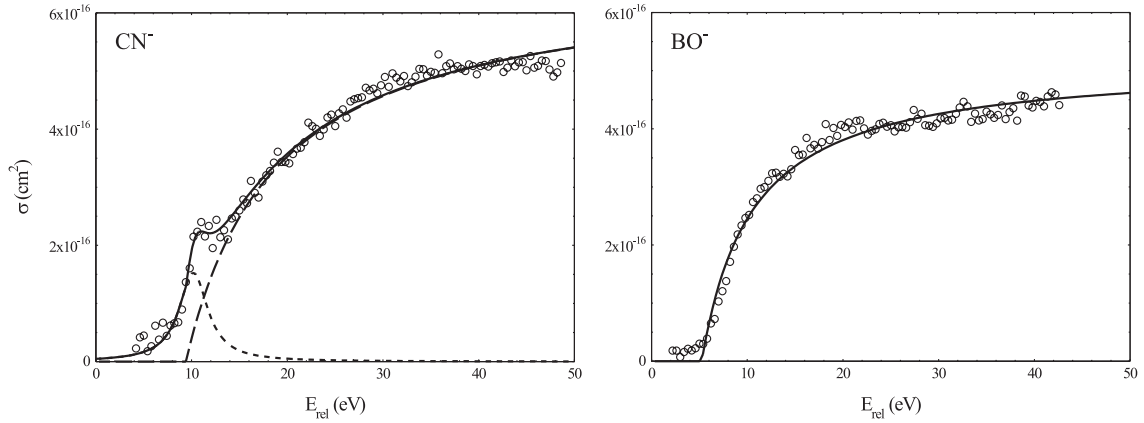


Figure 3.5: Absolute detachment cross-section for electron scattering on CN^- (left) and BO^- (right). Cross-sections are compared to the theoretical non-resonant cross-sections of Eq. 3.4 and in the case of CN^- a resonance state is observed.

The entire relative cross-section is then put on an absolute scale by using the absolute value measured at 30 eV. The result is presented for both CN^- and BO^- in Fig. 3.5. The cross-sections exhibit thresholds at 8.5 eV (CN^-) and 5.2 eV (BO^-), both of which are in accordance with the expected value calculated from Eq. 3.6. The CN^- cross-section shows a resonance state at 10.0 eV, above a GAUSSIAN-98 calculation of 6.5 eV for the dianion ground state. The resonance is thus attributed to an excited state. The width of the resonance, 2.4 eV, corresponds to a lifetime of only 0.3 fs. No resonance is found for BO^- . It remains an open question, why an excited state is observed for CN^{2-} and not for BO^{2-} .

With the resonance of CN^- positioned close to the threshold, it is difficult to estimate the significance of tunneling contribution in this reaction. The BO^- data fit the classical detachment model quite well, even better than that of Cl^- , which implies that tunneling contribution is of less importance in this system.

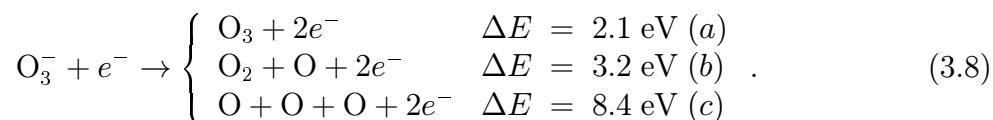
The CN^- experiment has also been performed at the Swedish heavy ion storage ring, CRYRING, in Stockholm [105]. This experiment yielded a threshold of only 7 eV, and the resonance found in the ASTRID experiment was thoroughly searched. It was concluded that the statistical uncertainty in the data was too large to conclusively prove or disprove the existence of the resonance.

3.3.3 O_3^-

O_3 is a well-known and important constituent in the atmosphere of the Earth, where it absorbs the harmful ultraviolet radiation from the Sun. It is formed from molecular oxygen under influence of ultraviolet radiation or in an electric discharge like lightning. It has a characteristic smell which is present in the air after a thunderstorm, and its name *ozone* is actual derived from the Greek *ozein* that means smell. The electron affinity of this molecule is 2.1030 ± 0.0040 eV [116].

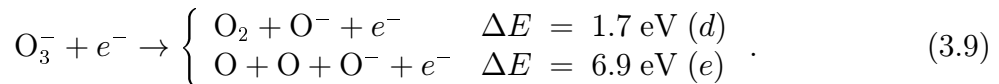
The ion was produced in the hollow-anode CCIS source discharging in O_2 gas, and a current of only 2-4 nA was extracted and stored at 2.144 MeV. This is one of the smallest ion currents successfully stored in ASTRID, and it was too low a current for the beam charge monitor to detect it in order to make an absolute measurement. Relative O_3^- cross-sections were measured from 0 to 50 eV, and this is shown in Fig. 3.6.

The pulse height spectrum recorded during this experiment was presented in Fig. 2.9, and the reaction cross-section was measured from the signal in each of the three peaks of this spectrum. The detachment signal, *i.e.* the SSD peak containing three neutral oxygen atoms, has three contributions (with the endothermic reaction energy, ΔE , listed):



The detachment cross-section can be fitted to the classical non-resonant cross-section of Eq. 3.4. This yields a threshold of 7.3 eV, which is 3.5 times the electron affinity of the molecule.

For most small anions, the dominating reaction induced by electron scattering is detachment (possibly in combination with dissociation) of the anion [80]. For O_3^- , however, the following channels involving pure dissociation, where one oxygen atoms carries a charge away (the second peak of the SSD spectrum) opens up even earlier (at 4.9 eV):



As seen in Fig. 3.6, this channel is actually of a magnitude similar to the detachment channel. Similar behavior is observed for photon scattering on O_3^- , where $h\nu + \text{O}_3^- \rightarrow \text{O}_2 + \text{O}^-$ is a dominant reaction channel in the wavelength interval from 508 to 640 nm [117], indicating that Franck-Condon factors play a crucial role in the scattering process. Channels resulting in only one neutral oxygen atom, *i.e.* channel³ f : ($\text{O} + \text{O}_2^-$), is about a magnitude smaller than the channels of Eq. 3.9. The small ($\text{O} + \text{O}_2^-$) channel has a maximum near 15 eV, drops off to near zero, and then begins to increase again.

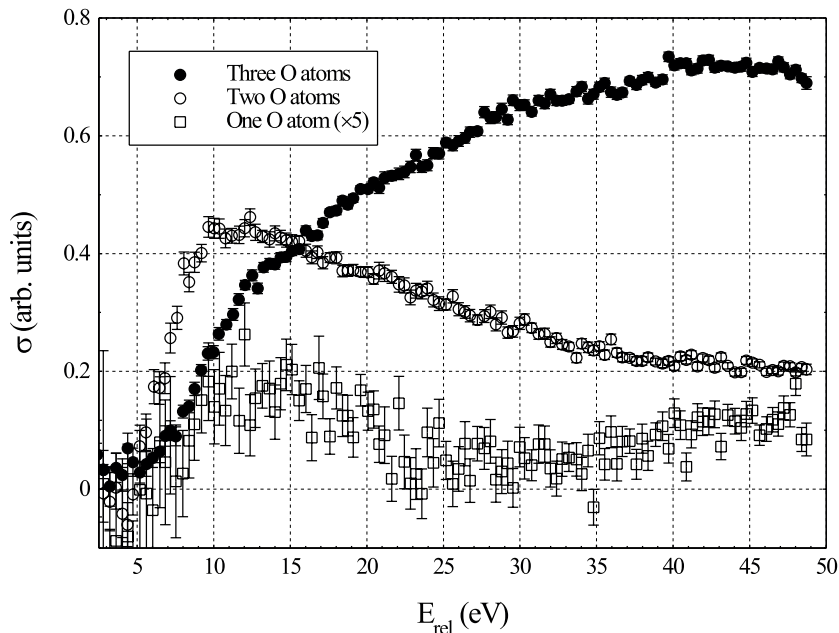


Figure 3.6: O_3^- cross-sections measured for each of the three peaks in Fig. 2.9. The *Three O atoms*-channel includes all channels leading to complete neutralization of the ozone anion. The two other channels consist of reactions leading to two and one neutral oxygen atoms, respectively. The *Two O atoms*-channel is most likely due to the $\text{O}_2 + \text{O}^-$ final channel. The *One O atom*-channel has been multiplied by a factor of 5.

The experimental technique, as described so far, only allows us to determine the cross-sections corresponding to the individual peaks of the SSD pulse height spectrum. As described in Eqs. 3.8 and 3.9, each peak includes contribution from several reaction channels. As an example, the detachment peak consists of impacts from both an O_3 molecule (channel a) and three individual O atoms (channel c). The detection system cannot distinguish these two channels, because the O atoms arrive at the detector practically simultaneously.

By utilizing a special grid technique we can measure the many reaction channels of the electron scattering process. If we insert a mesh grid of known transmission T in front of the detector, the two channels a and c will contribute to the full-energy peak with different probabilities, T and T^3 , respectively. With the grid we may thus differentiate between different channels that would otherwise deposit the same energy in the solid state detector.

³We here disregard channels involving positively charged ionization species.

For the O_3^- system, the total rate of events R_0 is distributed into the three peaks of the spectrum as follows:

$$R_{3 \text{ atoms}} = [aT + bT^2 + cT^3]R_0 \quad (3.10)$$

$$R_{2 \text{ atoms}} = [bT(1 - T) + 3cT^2(1 - T) + dT + eT^2]R_0, \quad (3.11)$$

$$R_{1 \text{ atom}} = [bT(1 - T) + 3cT(1 - T)^2 + 2eT(1 - T) + fT]R_0 \quad (3.12)$$

where $R_{n \text{ atoms}}$ is the rate of events recorded in each of the peaks in the SSD spectrum, and a, \dots, f are the branching ratios of the various channels. In our experiment we used two grids of transmissions 68% and 24%. These transmissions have been determined in previous experiments [118]. We thus obtain 10 equations (the three equations above with three values (100%, 68% and 24%) of T , and the normalization equation, $a + \dots + f = 1$) and 6 unknowns (a, \dots, f). This overdetermined system of equations is solved using a standard χ^2 minimization routine.

The peaks in the SSD spectrum are clearly distinguishable, and the ASTRID data acquisition system therefore allows us to set up single-channel analyzers, which count the signal in each individual peak, and from this we can automatically measure the branching ratios as a function of the relative collision energy. This is done in the energy interval from 8 to 36 eV, and the result is presented in Fig. 3.7. Pure detachment (channel a) dominates at energies above 13 eV, where it constitutes about 50% of the total flux. Below this energy, neutral O_2 (channel d) is the dominating result of the reaction. Channel b ($O_2 + O$ production) has a well-defined threshold at 18 eV, above which it increases smoothly to about 20% at $E_{rel} = 35$ eV. None of the remaining channels contribute more than about 5%.

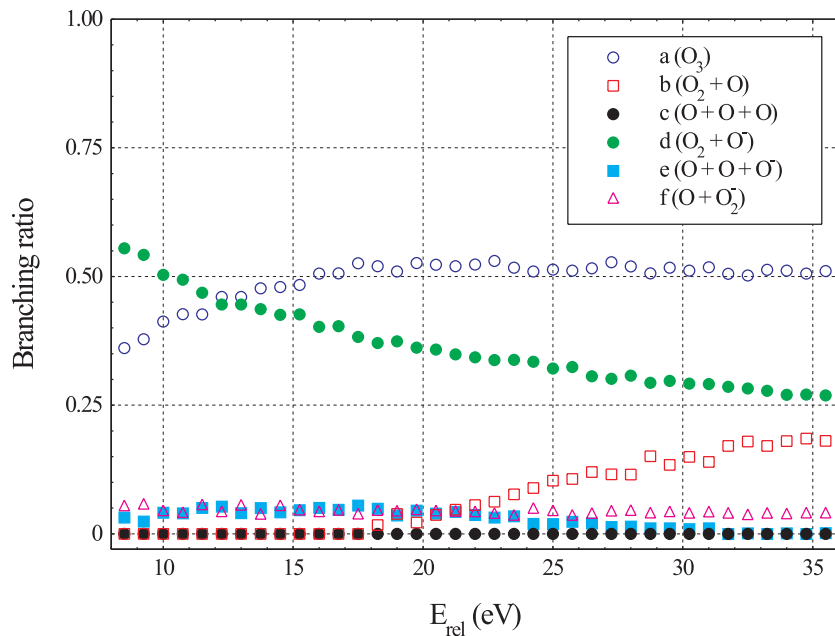


Figure 3.7: O_3^- branching ratios measured as a function of the relative ion-electron velocity.

3.3.4 NO_2^-

The NO_2^- ions were created in a 60 mA discharge in atmospheric air in the CCIS hollow-anode source, yielding a beam current of about 190 nA. The scattering cross-section was measured from 0 to 30 eV, and the measurement was placed on an absolute scale. The data are presented in Fig. 3.8.

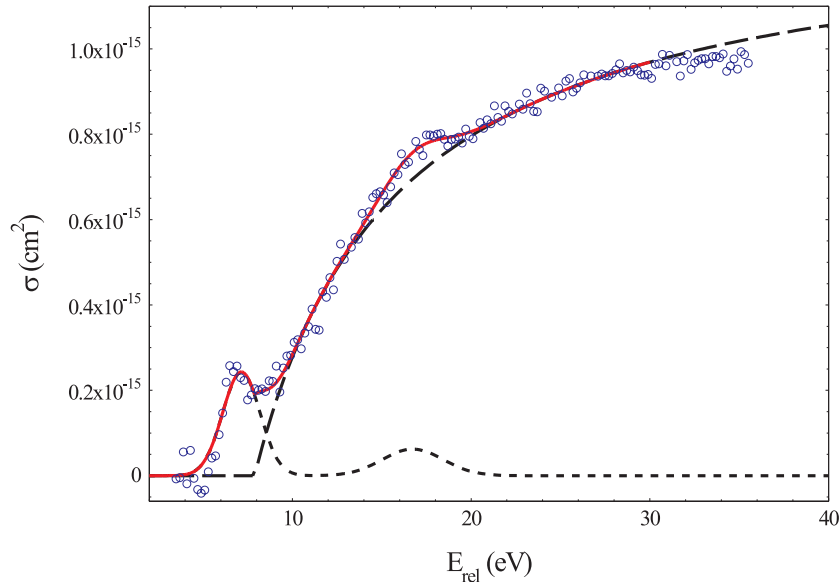
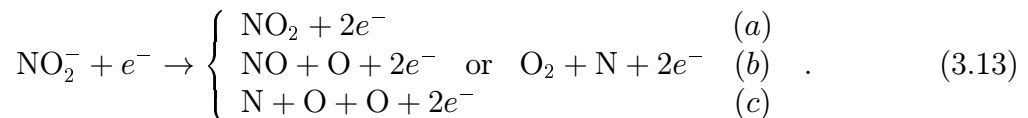


Figure 3.8: Total absolute detachment cross-section for NO_2^- fitted to the non-resonant model with two resonances superimposed.

The cross-section shows a threshold at about 7.9 eV, somewhat higher than what is expected from Eq. 3.6. Two resonances are seen, and this is to our knowledge the only ion for which more than one resonance has been observed. The resonances are located at 7.2 eV (FWHM: 2.3 eV, lifetime: 0.29 fs) and 16.5 eV (FWHM: 5.2 eV, lifetime: 0.13 fs). The lifetimes are typical values for resonance states supported by a repulsive Coulomb barrier [114]. The low energy resonance is close to the ground-state energy of the NO_2^{2-} dianion, as calculated by the GAUSSIAN-98 program. The two resonances are thus interpreted as the ground-state and an excited state of NO_2^{2-} . The situation is exactly the one depicted in Fig. 3.1.

Branching ratios were also measured. The pulse height spectrum revealed that only neutrals remained in the product channels:



The resolution of the SSD prevents us from distinguishing O from N atoms. The branching ratio analysis revealed that pure detachment dominates ($a \approx (75 \pm 15)\%$) over a large energy range (10-30 eV). The remaining reactions all appear to belong to the two indistinguishable ($\text{NO} + \text{O}$) and ($\text{O}_2 + \text{N}$) channels ($b \approx (25 \pm 15)\%$), while three-particle breakup seems negligible.

3.3.5 NO_3^-

Nitrogen trioxide, NO_3 , is one of the most important free radicals in atmospheric chemical reactions, and NO_3^- is the most abundant negative ion species, either free or clustered with H_2O , in the lower ionosphere [119]. This is essentially due to the high electron affinity of this ion (3.937 ± 0.014 eV [120]).

The ion was produced by a 70 mA discharge in atmospheric air in the CCIS hollow-anode source, and about 50 nA of current was extracted and stored in ASTRID at 2.112 MeV. Again, the N and O atoms were indistinguishable in the SSD spectrum, and generally the resolution was quite low, why it was difficult to resolve the individual peaks of the spectrum.

The *total* NO_3^- cross-section (*i.e.* the cross-section derived from the total signal in all the SSD peaks in combination) is shown in Fig. 3.9 from 0 to 40 eV. Contrary to the O_3^- spectrum (Fig. 2.9), the NO_3^- spectrum cannot be resolved into individual peaks. We thus plot the combined cross-section from all neutral particle channels. We can, however, see that signal is only observable in the two highest peaks corresponding to three and four neutral atoms ($\text{N}^+ + \text{O}^- + \text{O}_2$ is thus insignificant).

The cross-section shows a very good agreement with the non-resonant theory (Eq. 3.4) when a Lorentzian resonance structure is superimposed at an energy of 18.6 eV. This resonance is ascribed to the ultra-fast formation and decay of the doubly-charged negative ion of NO_3 . The FWHM of 4.46 eV corresponds to a lifetime of about 0.15 fs.

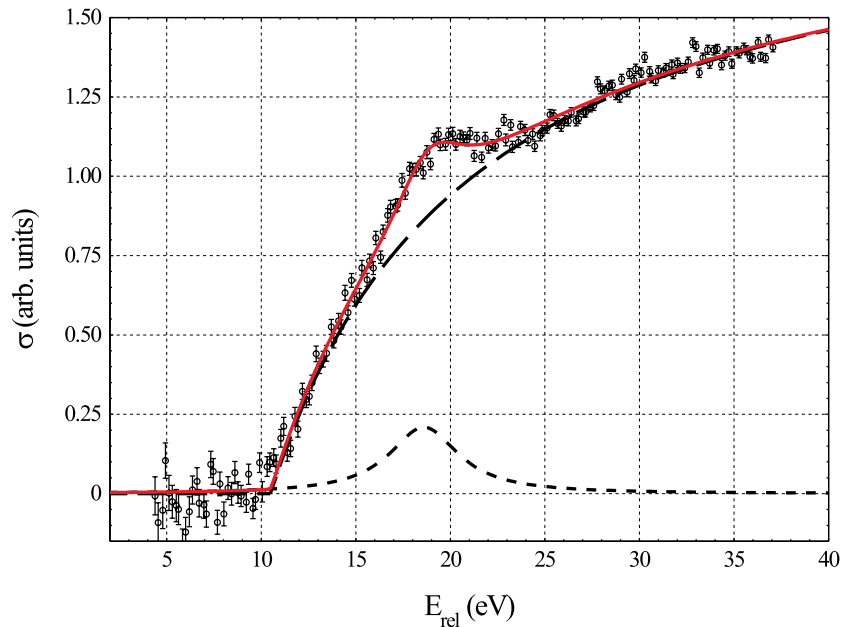
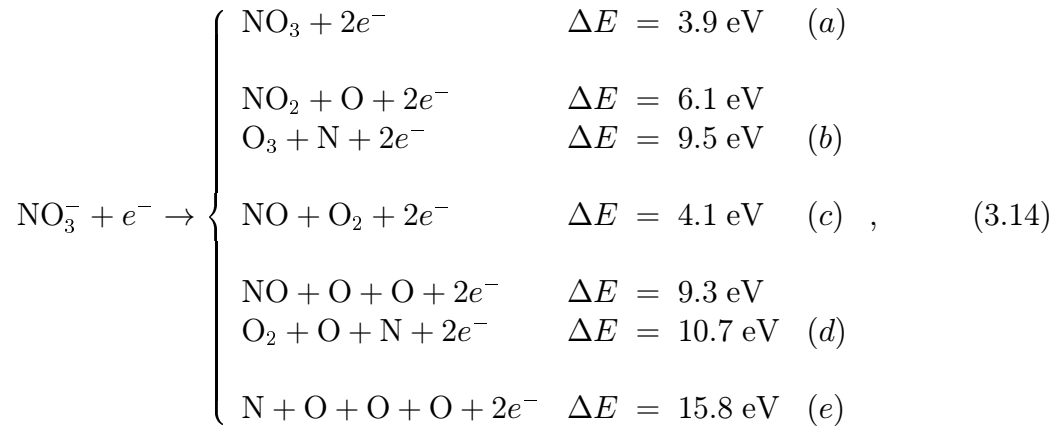


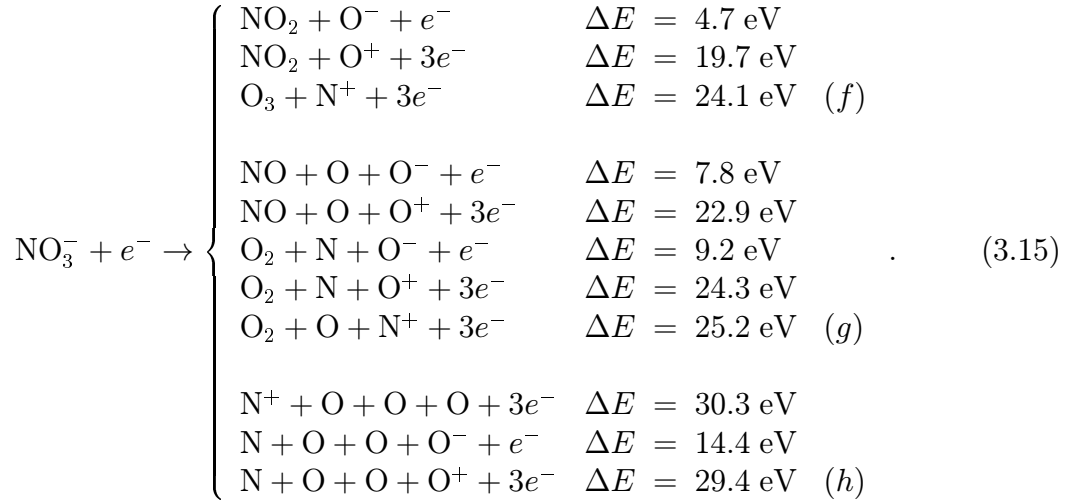
Figure 3.9: The total NO_3^- cross-section. The cross-section has been fitted (solid curve) with a sum of the non-resonant contribution (long-dashed) of Eq. 3.4 and a Lorentzian resonance (short-dashed). The threshold is 10.5 eV and the resonance position is 18.6 eV with a width of 4.5 eV.

Calculations with the GAUSSIAN-98 program package estimate the NO_3^{2-} ground-state to be 6.1 eV above the mono-anion state, and since the resonance is significantly higher than the predicted ground-state energy, we ascribe the observed resonance to an excited state of the dianion.

In the SSD spectrum from NO_3^- we only observe an electron-induced signal for channels leading to three or four atoms. The following channels can contribute to the four-atom peak:



while the following channels can contribute to the 3-atom peak:



The branching ratios are presented in Table 3.2. Only channels *a*, *b*, *c* and *f* appear to contribute with a non-negligible flux.

Energy	<i>a</i>	<i>b</i>	<i>c</i>	<i>f</i>
15 eV	60%	13%	4%	20%
25 eV	60%	12%	7%	22%
35 eV	53%	14%	10%	22%

Table 3.2: NO_3^- branching ratios. Error-bars are estimated to be about 8%.

As seen in Eqs. 3.14 and 3.15, these channels correspond to pure detachment and two-particle break-up, while three- and four-particle break-up channels are all closed. The signal is only strong enough to determine branching ratios for energies in excess of about 12 eV. In the energy range 12-35 eV, the branching ratios vary only slightly, and it is found that the pure detachment channel, *a*, dominates.

3.3.6 SO_2^-

Sulphur dioxide, SO_2 , enters the atmosphere as a result of both natural phenomena and human activities, *e.g.* combustion of fossil fuels (especially coal and oil burning), oxidation of organic material in soils, volcanic eruptions and biomass burning. In the atmosphere, SO_2 can be oxidized within airborne water droplets, producing sulphuric acid. The resulting acid rain is a major concern in environmental debates. The electron affinity of SO_2 is 1.1070 ± 0.0080 eV [121].

The SO_2^- was attempted produced in the CCIS hollow-anode source discharging in SO_2 gas, and an ion beam of up to 110 nA could be extracted. However, a problem with the SO_2^- ion is that magnetic analysis of the ion beam will select only ions of a specific mass-to-charge ratio, and we can thus not distinguish between S_2^- , O_4^- and SO_2^- ions, all of which have a mass of 64 amu when using the naturally most abundant isotopes ^{16}O and ^{32}S . The problem can be solved by using the ^{18}O and ^{34}S isotopes, which will result in ions of different masses (S_2^- , O_4^- and SO_2^- having masses of 68, 72 and 70 amu, respectively). Pure $^{34}\text{S}^{18}\text{O}_2$ gas is, however, not easy to obtain. Instead, SO_2^- ions were produced by the cesium sputter source fitted with a cathode containing ^{34}S and fed with a gas of $^{18}\text{O}_2$. This produced ion currents of about only 5 nA, which was stored and accelerated to 2.1 MeV.

The relative detachment cross-section was measured from 0 to 50 eV, and this is shown in Fig. 3.10. This cross-section again shows good agreement with the non-resonant detachment model with a threshold of 7.8 eV. No resonances are found, and again tunneling is believed to explain the slight deviance from the model near the threshold.

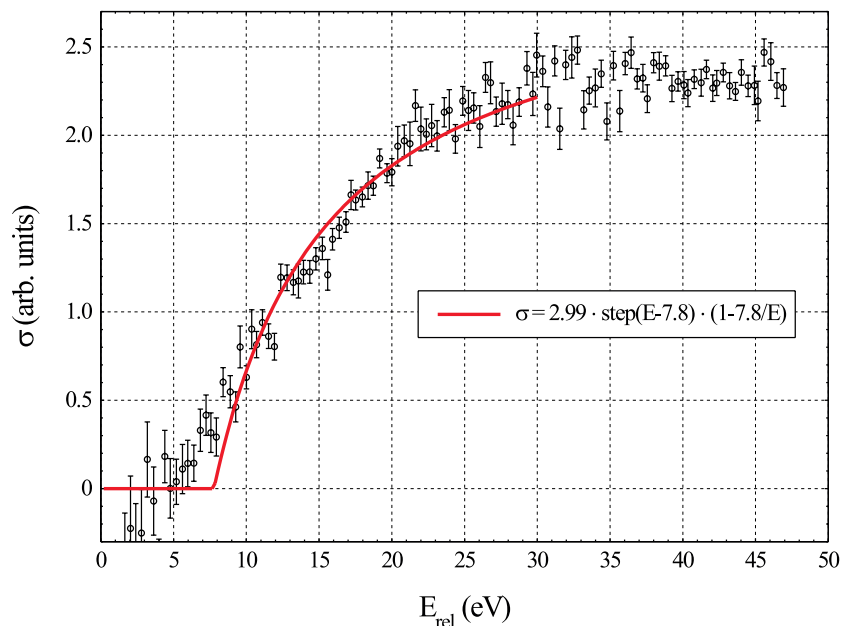


Figure 3.10: The SO_2^- detachment cross-section, *i.e.* the cross-section for channels leading to all neutral fragments, corresponding to the full energy peak of the SSD spectrum.

The branching ratios for SO_2^- were determined at one energy (40 eV). Once again, pure detachment is the dominant channel, attributing $(70 \pm 7)\%$ to the total reaction channel. The remaining channels all contribute with less than 10% each.

3.4 Comparison of anion cross-sections

Though only one of the polyatomic detachment cross-sections presented in the previous sections have been measured on an absolute scale, we may use Eq. 3.4 to predict the general energy dependency and the absolute magnitude of the cross-sections for NO_3^- , SO_2^- and O_3^- . The parameter R is related to the measured threshold energy $E_{th} = 1/R$, which leaves only p as an unknown variable. Note that p acts only as a scaling factor with no influence on the shape of the cross-sections. Previously measured detachment cross-sections for a number of different ions have yielded values of p ranging from 8% for F_2^- to 125%⁴ for NO_2^- . The average for all measured anions is about 40% and this value is chosen for all three ions of the present work. The resulting non-resonant model cross-sections can be seen in Fig. 3.11. The cross sections are expected to be accurate within a factor of two.

In Fig. 3.12 all threshold values for electron scattering on anions measured at storage rings are plotted as a function of the electron affinity of the corresponding molecules and atoms. The data plotted in this figure are obtained at CRYRING (Refs. [78, 99, 105, 112]) and at ASTRID (present work and Refs. [76, 79, 80, 81, 122]).

The $\text{EA}^{3/4}$ prediction of Eq. 3.6 is also shown in Fig. 3.12. The atomic ions appear to follow this prediction very well. The diatomic ions also agree quite well with this curve, though the two ions O_2^- and F_2^- differ significantly from the remaining group of diatomics. This is explained by a poor Franck-Condon overlap between the neutral and anionic states, and a much better agreement is obtained by using the vertical electron affinities of the molecules. These electron affinities are almost 1 eV larger than the adiabatic electron affinities. The polyatomic anions exhibit a threshold that is higher than the prediction of Eq. 3.6, also presumably because of poor Franck-Condon overlap.

3.5 Conclusion

Relative cross-sections for electron scattering on a number of negatively charged ions have been measured in the energy range from 0 to about 50 eV. All cross-sections exhibit a well-defined onset at some threshold energy, which is significantly larger than the electron affinity of the corresponding molecule. This is consistent with a classical reaction model.

The detachment thresholds have been determined for the atomic ions Cl^- and S^- . Both cross-sections are only measured on a relative scale as a function of energy. The Cl^- threshold has also been measured at CRYRING, and the different results are ascribed to the choices of energy intervals used in the fitting procedures. The absolute detachment cross-sections have further been determined for the diatomic molecular ions CN^- and BO^- . These are isoelectronic anions, and it is thus interesting to compare the results for the two ions. A resonance is seen in the CN^- cross-section, but not in the BO^- cross-section. It is not clear why this is the case.

Relative cross-sections have been measured for the four polyatomic ions, O_3^- , NO_2^- , NO_3^- and SO_2^- . Only the NO_2^- result is calibrated to an absolute scale, while none of the other ions could be produced in high enough quantities for an absolute calibration. The general energy dependency of the cross-sections on an absolute scale are, however, predicted using the classical reaction model. Two resonances corresponding to dianion formation are observed for NO_2^- , while one resonance is observed for NO_3^- . Moreover,

⁴The NO_2^- ion is the only ion for which the p factor exceeds 100%.

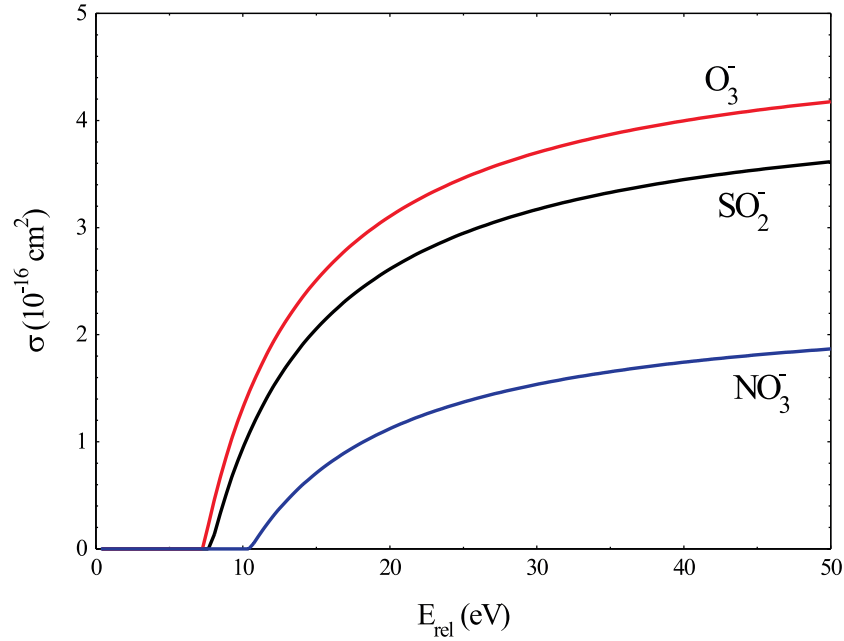


Figure 3.11: Non-resonant model cross-sections calculated from Eq. 3.4 using the measured thresholds E_{th} . The scaling factor p has been chosen to be 40%.

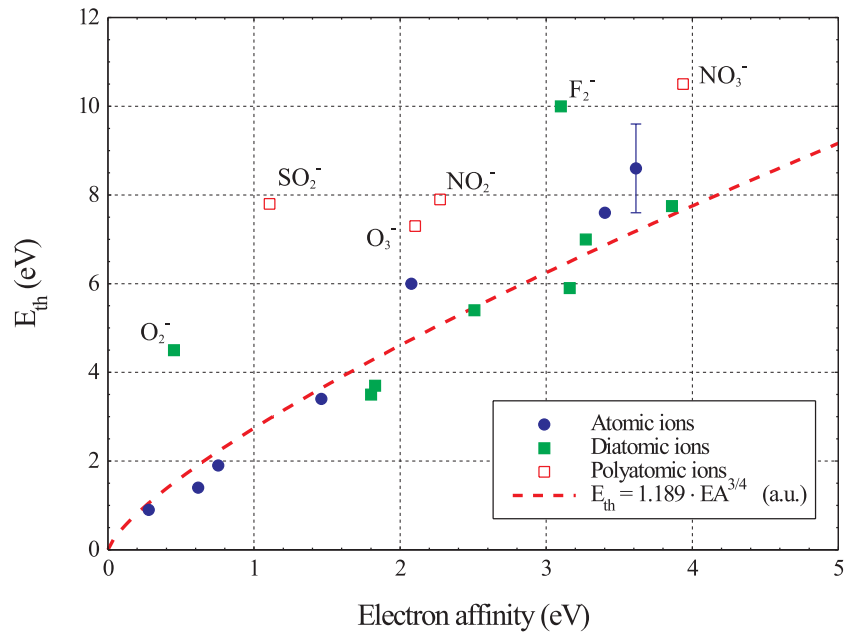


Figure 3.12: Anion detachment thresholds as a function of the electron affinity. The dashed line is the theoretical prediction of Eq. 3.6. Selected ions are labeled. An average of two different values (from ASTRID and CRYRING, respectively) for CN^- and Cl^- are included in the figure. The uncertainties on the thresholds are estimated from the two measured values of Cl^- , and this is represented as an error-bar on the Cl^- data point. The atomic ions in the figure are (from left to right): B^- , Li^- , D^- , O^- , S^- , F^- and Cl^- . The diatomic ions are (from left to right): O_2^- , B_2^- , OH^- , BO^- , F_2^- , BN^- , C_2^- and CN^- .

reaction branching ratios have been measured for the ions. The main reaction channel for all ions is the pure detachment channel, except for O_3^- below relative energies of 13 eV, where the $\text{O}_2 + \text{O}^-$ channel dominates. All ions exhibit negligible three- and four-particle break-up.

All anion cross-section thresholds previously measured at the ASTRID and CRYRING storage rings are compared to the electron affinities of the corresponding neutral species. A classical over-the-barrier model predicts the atomic anion thresholds well, whereas Franck-Condon factors play a role for molecular ions.

In the future we plan to measure electron-impact detachment of micro-solvated NO_2 , *i.e.* NO_2^- ions clustered with one or more water molecules; $\text{NO}_2^-(\text{H}_2\text{O})_n$. Though small negative ions are unable to support an extra charge and form a stable doubly-charged negative ion, the same ion may be stable in solution, where polarization interactions between ions and the surrounding medium may cause complete stabilization. Notable examples are the SO_4^{2-} and HPO_4^{2-} ions, which are unstable in gas-phase but exist as stable ions in bodily fluids, where they play a vital role as electrolytes. The resonances found in the NO_2^- experiment presented in this thesis is thus expected to be stabilized as a function of the number of water molecules attached to the cluster, and this should be observed as a decrease in the energy of the resonance positions.

Chapter 4

Electron scattering on doubly-charged positive ions

This chapter describes experiments with electron scattering on positively charged ions performed at the heavy-ion storage ring ASTRID. We have measured the rate coefficient for dissociative recombination, and the thermal rate coefficients have been extracted for three different doubly-charged molecular ions and compared to those of the corresponding singly-charged ions. Moreover, branching ratios for molecular break-up have been determined.

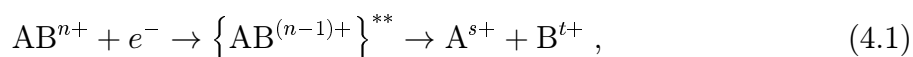
4.1 Introduction

The present study was initiated to better understand the collision dynamics involved when free electrons scatter on doubly-charged positive ions (dications). We address the following questions:

- What is the dissociative recombination rate coefficient as a function of the relative electron-ion energy, and what is the associated thermal rate coefficient?
- Which dissociative recombination and excitation channels do the electron-ion collisions result in?
- How is electron scattering on dications different from that of monocations?

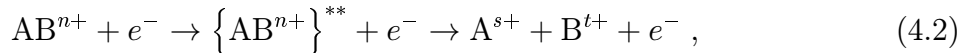
4.1.1 General introduction

Dissociative recombination (DR) is the reaction in which a positively charged molecular ion recombines with an electron to form an excited intermediate complex, which subsequently dissociates into smaller fragments. These fragments may possess kinetic energy and potential excitation energy. In the case of a multiply-charged diatomic molecule AB, the reaction may be written as follows:



where $(n - 1) = s + t$. With typical thermal rate coefficients of $10^{-7} \text{ cm}^3/\text{s}$, DR is a very fast process. In comparison, thermal rate coefficients for atomic recombination are usually of the order of $10^{-12} \text{ cm}^3/\text{s}$ for radiative recombination and $10^{-9} \text{ cm}^3/\text{s}$ for dielectronic recombination. Electrons scattered on a molecular ion may also induce dissociative

excitation (DE), which leaves an additional charge in the product channel, *i.e.* the incident electron induces dissociation without itself being bound to any atomic or molecular fragment in the final state. For our model molecule AB, this reaction takes the following form:



where $n = s + t$. DR and DE are complex molecular processes that occur in any plasma cold enough to contain molecular constituents, and they are typically some of the dominant processes in both naturally occurring and man-made plasmas relevant to for instance planetary atmospheres [123, 124, 125, 126], fusion plasmas [14], the space shuttle environment [127], chemistry of interstellar matter [128, 129, 130] and the comas of comets [131], but also to laser physics, reentry vehicles, plasma processing and combustion science. For singly-charged ions, DE is usually not energetically allowed at low collision energies, but it is important at energies above ~ 10 eV, and it is consequently a topic of interest when considering high temperature plasmas. For multiply-charged cations, DE can be energetically allowed even at zero collisional energy. Reviews of dissociative recombination are found in Refs. [3, 132, 133].

Doubly-charged molecular cations differ from singly-charged species in fundamental ways. If two charges are brought together in a small molecule, the long-range Coulomb repulsion lifts the potential energy surfaces, and small multiply-charged ions are thus unstable towards dissociation because their energy levels are embedded in the continuum. However, the bonding properties of dications give rise to interesting topologies of their potential energy surfaces, where the short-range binding interactions within a molecule may form a shallow well separated by a broad potential barrier from the dissociation continuum at low energy. At large internuclear distances, the potential is dominated by the repulsive Coulomb interaction. The shallow potential minimum often supports several quasi-bound vibrational levels lying well above the dissociation asymptote, and these metastable states will eventually decay through either direct dissociation (preceded by tunneling through the barrier), or by electronic predissociation by another state.

Another characteristic of a reaction with a doubly-charged molecular ion is that the resultant fragments will often possess considerable kinetic energy. Typical kinetic energy releases during ion pair formation from diatomic dications are comparable to the reaction exothermicities of many of the chemical reactions used to propel rockets. This significant energy release, which is stored as potential energy in the undissociated dication, has led to the classification of these dications as *high energy-density materials* [134].

Electron capture by multiply-charged molecular ions has been proposed [123] as a mechanism for generating singly-charged ions in the upper atmosphere of Earth. Molecular double-photoionization has been proposed as a source of energetic, charged particles in the terrestrial ionosphere and in the interstellar medium [135]. Furthermore, multiply-charged molecules may be found in various astrophysical environments [136].

Since dications are generally relatively difficult to produce and may undergo spontaneous dissociation on timescales shorter than those of typical experiments, only very little is known about their structure and dynamics. Recombination of multiply-charged *atomic* species has been studied extensively [25, 137], but knowledge about dissociative recombination of multiply-charged *molecules* is sparse, as most theoretical and experimental work has focused on singly-charged species. Review articles on doubly-charged positive ions can be found in Refs. [138, 139].

4.1.2 Historical overview

The interest in dissociative recombination was partly sparked by the presence of a green emission line in the atmosphere of Earth. When looking up during the night, one normally sees a black carpet filled with thousands of twinkling stars; or so it appears to the naked eye. If a spectrometer is pointed towards the sky, various faint emission lines are observed, one of those a green line of 557.7 nm, discovered already at the end of the 19th century [140]. The wavelength of the emission line was determined with great precision in 1923, and after a few years of experimental work, it was determined in 1927 [141] that the emission line was produced by a forbidden transition in atomic oxygen ($O(^1S) \rightarrow O(^1D)$).

This explained the presence of the green emission line, but it did not explain why large concentrations of atomic oxygen was found in the upper atmosphere. A solution to this enigma was suggested in 1931 by Kaplan [142], who believed that dissociative recombination of molecular oxygen ions was the source of atoms. Though experiments indicated that the rate coefficient for this process was high enough to produce the right amounts of atomic oxygen (*i.e.* of the order of 10^{-8} - 10^{-7} cm³/s), theory predicted much lower values. Early theoretical studies [143, 144] of the reactions in the upper atmosphere assumed that DR could be neglected, and that electron-ion recombination occurred through radiative free-to-bound transitions, processes of rate coefficients as low as 10^{-12} cm³/s. In 1947, however, it was pointed out by Bates and Massey [145] that DR was the only process that could explain the observed electron recombination rates in the upper ionosphere of the earth.

In 1950, Bates [146] presented a theory of dissociative recombination that could explain the observed rate coefficients, and in the following years interest in the process thus increased with the recognition that DR was of the utmost importance to the charge density of a plasma. Particularly, the interest was sparked in military circles, where it was realized that the effect of a nuclear explosion in the atmosphere would create ionization that disturbed radio communication. A wish to model the charge density of the atmosphere thus motivated thorough investigation of the process.

In 1968, Bardsley [147] added to the theoretical understanding of DR by suggesting a new physical mechanism leading to DR. Both the theory of Bates and that of Bardsley, later named the *direct* and *indirect* mechanisms, respectively, will be described in section 4.2.

Doubly-charged positive ions have in principle been known since 1899 with the discovery of He^{2+} ions, or *alpha particles* as they were coined by their discoverer Ernest Rutherford. Several both positive and negative ions were later observed in J. J. Thomson's mass spectrometers during the first two decades of the twentieth century. Thomson, at first, did not observe multiply-charged molecules [63], but this task was instead accomplished by his assistant Aston [148, 149]. Later, Thomson [150] found evidence for N_2^{2+} or CO^{2+} , which are one of the subjects of this Chapter.

At the time it was believed that dications were quite unstable and that the experiments of Aston and Thomson were a few exceptions to a general rule stating that molecular dications were too short-lived to show up in mass spectrometers. In 1930, however, Conrad [151] refuted this rule by identifying several doubly-charged molecular ions like O_2^{2+} , CO^{2+} and CO_2^{2+} . The year after, the first ionization potential for a multiply-charged molecule (CO^{2+}) was measured by Vaughan [152]. In 1932 Friedländer [153] studied dications like CO^{2+} and CO_2^{2+} , and he found that the ions were probably unstable towards dissociation, but that they were metastable with lifetimes longer than 1 μ s. This was

explained with a potential well model still used today.

With Friedländer's discovery of metastable dications, the following search soon identified a stable state of N_2^{2+} [154]. The same work yielded the double-ionization potential of nitrogen, and in 1958 Carroll made the first observation of fluorescence from N_2^{2+} [155]. These experiments were only the beginning of a long history of experimental and theoretical exploration of the structure of the N_2^{2+} ions. For more details on previous work, see for instance Refs. [156, 157, 158, 159].

The desire to study multiply-charged ions was one of the driving thrusts behind the development of storage rings for atomic physics [15], and indeed the storage ring technique was applied to dications early in the youth of heavy-ion rings. Storage ring experiments about 10 years ago [160, 161] on N_2^{2+} , CO^{2+} and other dications showed that multiply-charged positive molecular ions can contain long-lived components with lifetimes longer than a few seconds. In these experiments it was found that the lifetime was limited by residual gas collisions, and the ions were practically stable, at least on the time-scale of a storage ring experiment. This motivated further storage ring investigations of the ions, as presented in this thesis. Today, even small thermodynamically stable dications, *i.e.* dications stable with respect to all dissociation channels, are known [162].

4.2 Theoretical overview

As described in the previous section, the history of dissociative recombination is a long and interesting tale. The development of a theoretical treatment of the reaction has yielded several different mechanisms in order to describe the DR cross-section accurately. These mechanisms will be overviewed in the following.

Direct DR mechanism

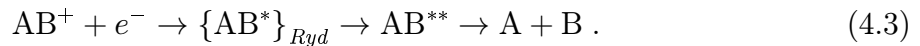
Early theoretical models treating dissociative recombination underestimated the rate coefficient by magnitudes. This was based on the argument that the reaction involves the exchange of energy from electronic to nuclear motion, something that would cause breakdown of the Born-Oppenheimer approximation. In the *direct* (or *curve-crossing*) mechanism for DR, proposed by Bates [146], this breakdown is prevented. In this picture, the reaction takes place in two steps: i) capture of the electron, and ii) stabilization through dissociation. Initially, the incident electron excites a target electron in the molecule, and simultaneously itself is captured into an unoccupied orbital. The potential energy curve controlling the motion of the nuclei is now that of the doubly-excited molecular system, and not that of the initial ionic state. If the potential curve is repulsive, the nuclei will consequently separate and dissociate. The recombination process is thus *not* a direct energy transfer from electron to nuclei, but an exchange of energy between the incident electron and a bound target electron. The molecule will, however, have to survive against the possibility of the electron autoionizing. The lifetimes of autoionizing states are typically of the order of 10^{-14} seconds. Using the Born-Oppenheimer approximation, autoionization is forbidden for internuclear distances larger than the crossing point between the repulsive and the initial potential curve. This results in stabilization times of the order 10^{-16} to 10^{-15} seconds, which thus makes the direct DR mechanism very efficient. The direct DR mechanism is sketched in the case of a diatomic molecule in Fig. 4.1.

In 1948, E. P. Wigner showed [163] that for the same long-range potential, the reaction between particles with very low relative velocities has a cross-section with the same

function of energy, no matter what particles collide. For a Coulomb attraction between the colliding particles, he found that the cross-section is proportional to $1/E$ at small collision energies. Indeed, the cross-section for the direct mechanism is expected to be large at very small electron energies and then fall off like $1/E$. If there exists excited neutral states, a broad peak can be observed in the total DR cross-section at larger collision energies (typically above a few eV).

Indirect DR mechanism

The direct mechanism is fully valid within the Born-Oppenheimer approximation, while the indirect process of Bardsley [147] goes beyond this. In the indirect mechanism, the series of Rydberg states converging to the ionic state serves as intermediate states of the DR process. Initially, the captured electron excites the ion core vibrationally producing a neutral molecule in a bound Rydberg state, which is then predissociated by a repulsive curve. For a singly-charged diatomic ion, the mechanism may be written as:



In analogy with direct DR, predissociation competes with autoionization as the stabilization mechanism. Indirect DR is a resonant process, because the first step of Eq. 4.3 requires the electron collision energy to match that of a vibrational level of one of the Rydberg states. The indirect DR mechanism is also sketched in Fig. 4.1.

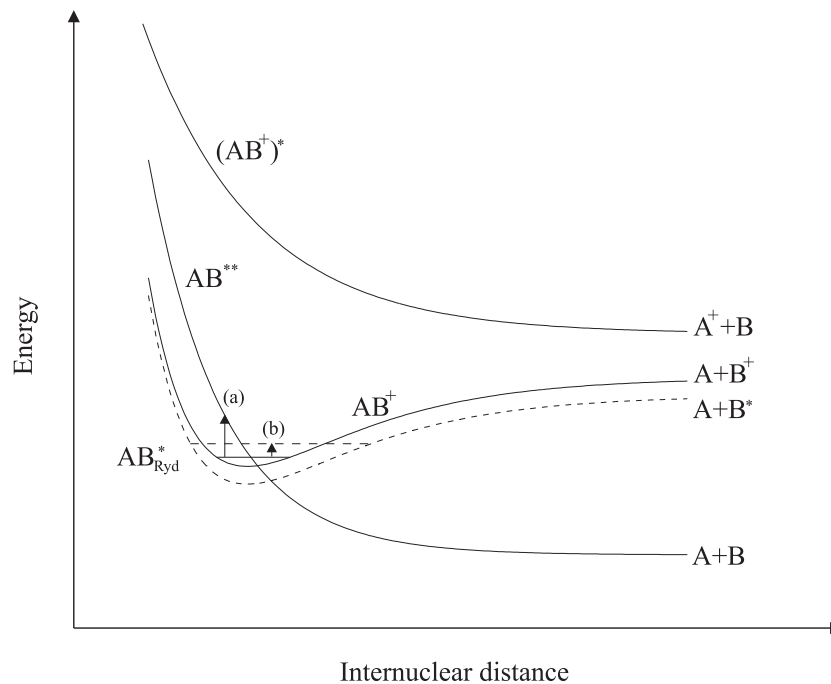


Figure 4.1: Schematic diagram of potential energy curves for a diatomic molecule. The arrows (a) and (b) indicate the *direct* and the *indirect* mechanisms for dissociative recombination. DR of polyatomic molecules proceed in a similar fashion.

Combining direct and indirect DR

When a doubly-excited repulsive neutral state crosses the ionic state, this repulsive curve will also cross the Rydberg state potentials situated below the ionic state potential. Thus,

when the direct process of DR is open, the indirect process will be present as well and the two processes may interfere quantum mechanically, leading to narrow resonances [164] in the DR cross-section at low energies¹.

Ignoring interference between the direct and indirect mechanisms, the cross-section for the indirect process may be written as [147]:

$$\sigma(E) = \sum_s \frac{\pi \hbar}{2mE} \frac{g_s}{2} \frac{\Gamma_{sa}\Gamma_{sd}}{(E - E_s)^2 + \Gamma_s^2/4}, \quad (4.4)$$

where the subscript s denotes the individual intermediate resonance states s , Γ_{sa} and Γ_{sd} are the partial widths against decay by autoionization and predissociation, respectively, and Γ_s is the total width. E_s is the energy of the intermediate state and g_s is its multiplicity. For narrow resonances, Γ_s can be neglected, and the indirect DR cross-section approximately scales as $1/E^3$, which accordingly may cause deviations from the $1/E$ behavior expected for the direct mechanism at low energy. Even though the capture process involves a change in the nuclear configuration, the indirect mechanism may be as efficient as the direct since only a single radiationless electron-transition is needed; the direct mechanism is governed by a two radiationless electron-transitions from the ionic ground-state to a doubly-excited neutral state.

Tunneling DR mechanism

Both the direct and indirect mechanism rely on favorable curve crossings between the initial ionic state and a state of the neutral system. In the direct mechanism, the repulsive potential energy curve of the neutral molecule must cross the ionic potential energy curve between the classical turning points of the initial vibrational state, and a similar argument holds true for the indirect mechanism.

For a long time it was believed that such a favorable curve crossing was a prerequisite for a high DR rate coefficient. Gradually, however, it has been realized that other mechanisms can lead to high rate coefficients as well. For some molecular ions, such as HeH^+ and H_3^+ , there are no doubly-excited neutral states crossing the ionic ground-state potential close to its minimum, yet experimental measurements have found high rate coefficients of 10^{-8} to 10^{-7} cm^3/s [165, 166, 167].

These high rate coefficients can be explained by the *tunneling* mechanism of DR, in which the molecular ion simultaneously captures an electron and tunnels through the potential barrier to a neutral repulsive state located on the left hand side of the ionic potential well [168]. This situation is sketched in Fig. 4.2.

Since this mechanism involves tunneling, it is expected to be efficient only for hydrogen containing molecules. This is supported by the observation of a strong isotope effect in the DR of HeH^+ and HeD^+ [169]. As for indirect DR, only a single radiationless electron-transition is needed, and the tunneling mechanism can be relatively efficient despite the fact that the capture process involves a change in nuclear configuration to shorter internuclear distance.

¹The first step in the indirect mechanism is only possible for collision energies below the dissociation energy of the molecular ion.

predicted (using results presented in this thesis) to exist in the atmosphere of Mars in densities detectable by future space missions to Mars [125, 126].

A metastable state of CO_2^+ was discovered in 1964 [173], and later storage ring experiments [160, 161] on CO_2^+ and other dications showed that the ion contains long-lived components with lifetimes longer than a few seconds. DR of CO_2^+ has been studied using both the stationary and the flowing afterglow techniques since 1967, but this is to our knowledge the first study of the CO_2^+ DR rate coefficient using the storage ring technique. Also, this is believed to be the first determination of the DR rate coefficient for CO_2^{2+} .

CO_2^+ and CO_2^{2+} ions were produced by electron-impact ionization of a CO_2 gas in a Nielsen type plasma ion source, and ion currents of about $1 \mu\text{A}$ of CO_2^+ and 60 nA of CO_2^{2+} were extracted and stored in ASTRID. This difference in ion currents produced by the same type of source operating under similar conditions clearly demonstrates one of the problems with multiply-charged ion research; dications are quite simply more difficult to produce in ion sources. CO_2^+ was stored at 3.35 MeV and CO_2^{2+} at 6.50 MeV , and the ion beam lifetimes were 2 seconds and 1 second, respectively. None of the ions have any dipole moment, and thus some rovibrational excitation is believed to exist in the stored beams.

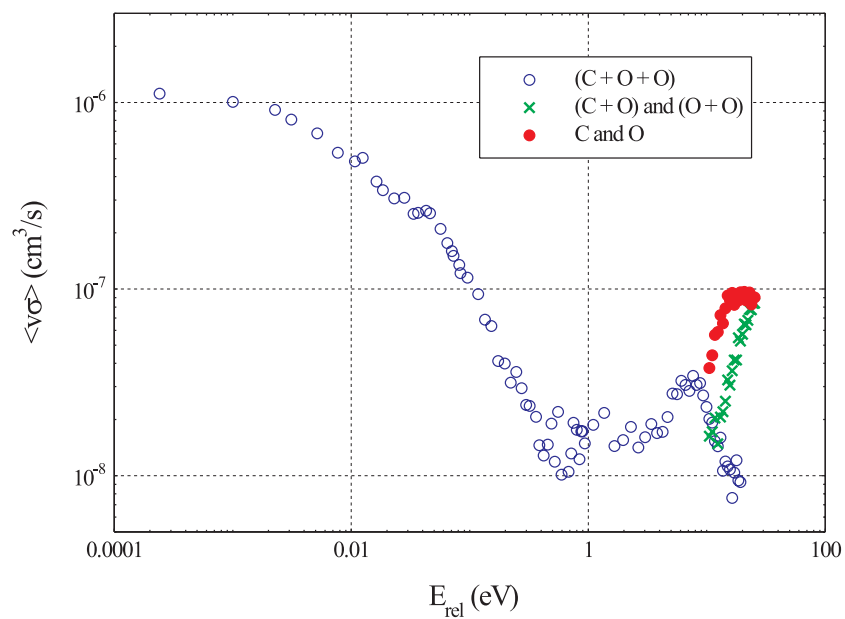
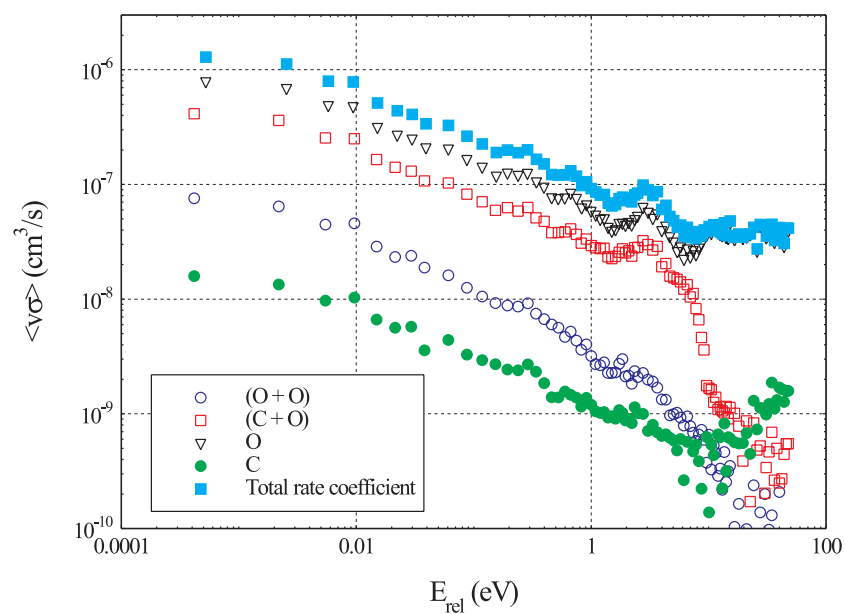
The absolute ion currents were measured by two different methods: the CO_2^+ current was measured with the beam charge monitor already mentioned. The stored ion current of CO_2^{2+} did not exceed 10 nA and the BCM technique could not be used, and instead we used the signal from a set of pick-up electrodes in ASTRID. This signal was fed to a spectrum-analyzer, which monitored the input at the revolution frequency of the ions, thus providing a measure of the number of ions in the ring. The signal was calibrated to a known ion current. For this method to be exact, the two ion beams (the calibration ion beam and the CO_2^{2+} beam) have to be stored with identical ion bunch shapes, which is not always guaranteed. We thus estimate the uncertainty of this technique to be about 30 percent. Indeed, the main contribution to the uncertainties of our results comes from the absolute measurement of the stored ion current.

The total DR rate coefficients for CO_2^+ and CO_2^{2+} are shown in Figs. 4.3 and 4.4. The curves show the rate coefficients measured for each individual neutral fragment peak in the SSD spectrum. Each curve is denoted by the atomic constituents of the neutral particles, so *e.g.* the curve denoted by “(C,O)” includes channels like $(\text{CO} + \text{O}^+)$ and $(\text{C} + \text{O} + \text{O}^+)$.

For CO_2^+ , the rate coefficient is observed to drop two orders of magnitude up to a center-of-mass energy of about 1 eV . A wide resonance is seen at about 7 eV , and the rate coefficient then drops at higher energies. Above approximately 10 eV , we start to see dissociative excitation channels, *i.e.* channels containing charged fragments where not all constituent atoms of the molecule hit the detector. The CO_2^{2+} rate coefficients drop continuously up to 10 eV , and resonance-like structures are seen in the total rate coefficient at 0.3 , 0.7 , and 3 eV . Notice the sharp drop near 8 eV in the (C,O) channel (*i.e.* the SSD peak at mass 28), which will be discussed later in connection with branching ratios.

The electron distribution in the electron cooler is, as described in section 2.2.2, not equal to that of a thermal plasma. To compare the measured rate coefficients to thermal rate coefficients (which is the parameter relevant to plasma physics), the cross-section must first be unfolded from the electron cooler velocity distribution and then reconvoluted with a thermal electron distribution; that is, we must find σ from $\langle v\sigma \rangle_{\text{cooler}}$ and then calculate $\alpha = \langle v\sigma \rangle_{\text{thermal}}$.

In practice, we compare the measured rate coefficients with model cross-sections that

Figure 4.3: Measured rate coefficients for CO_2^+ .Figure 4.4: Measured rate coefficients for CO_2^+ .

have been convoluted with the known electron cooler velocity distribution. This yields the following cross-sections (see Fig. 4.5 for the CO_2^+ data):

$$\begin{aligned}\sigma_{\text{CO}_2^+}(E) &= 4 \cdot 10^{-16} \frac{1}{(E[\text{eV}])^{1.3}} \text{ cm}^2 \\ \sigma_{\text{CO}_2^{2+}}(E) &= 1.5 \cdot 10^{-15} \frac{1}{(E[\text{eV}])} \text{ cm}^2.\end{aligned}\tag{4.5}$$

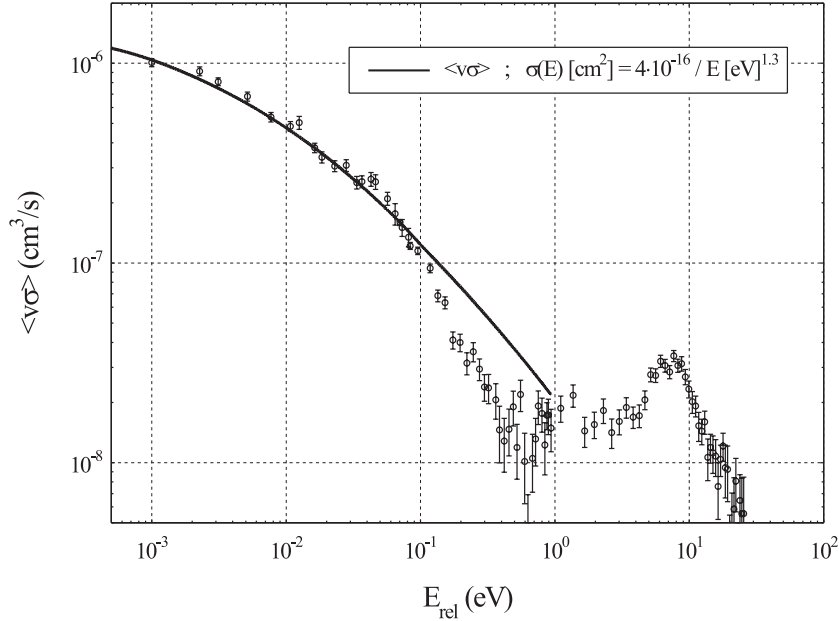


Figure 4.5: Model cross-section convoluted with the electron cooler velocity distribution compared with measured $\langle v\sigma \rangle$ for CO_2^+ . Measured data show good overlap with model cross-section in the energy range from 10^{-3} to 10^{-1} eV.

This allows us to extract a thermal DR rate coefficient in accordance with the relation [174] (this equation is derived in App. C.2):

$$\alpha(T) = \frac{8\pi m_e}{(2\pi m_e kT)^{3/2}} \int_0^\infty \sigma(E) e^{-E/kT} E dE.\tag{4.6}$$

Using the cross-sections given in Eq. 4.5, this integral can be calculated analytically, yielding the following rate coefficients:

$$\begin{aligned}\text{CO}_2^+ &: (6.5 \pm 2.6) \times 10^{-7} \times \left(\frac{300}{T[\text{K}]}\right)^{0.8} \text{ cm}^3\text{s}^{-1} \\ \text{CO}_2^{2+} &: (6.2 \pm 3.1) \times 10^{-7} \times \left(\frac{300}{T[\text{K}]}\right)^{0.5} \text{ cm}^3\text{s}^{-1}\end{aligned}\tag{4.7}$$

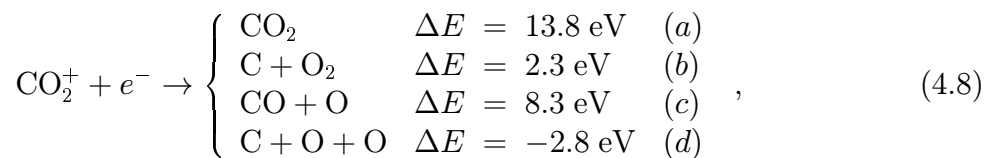
This is to our knowledge the first measurement of the DR rate coefficient for the CO_2 dication. The DR rate coefficient for the monocation has, however, been measured before. Our result compares to previous stationary and flowing afterglow results as listed in Table 4.1. It can be seen that the present data are almost a factor of 2 higher than

Method	Thermal rate coefficient	Reference
Microwave afterglow	(3.8 ± 0.5)	[175] (1967)
Microwave afterglow	(4.0 ± 0.5)	[176] (1973)
FALP	(3.1 ± 0.6)	[177] (1991)
FALP	(3.5 ± 0.5)	[178] (1997)
Storage ring	(6.5 ± 2.6)	[179] (present work)

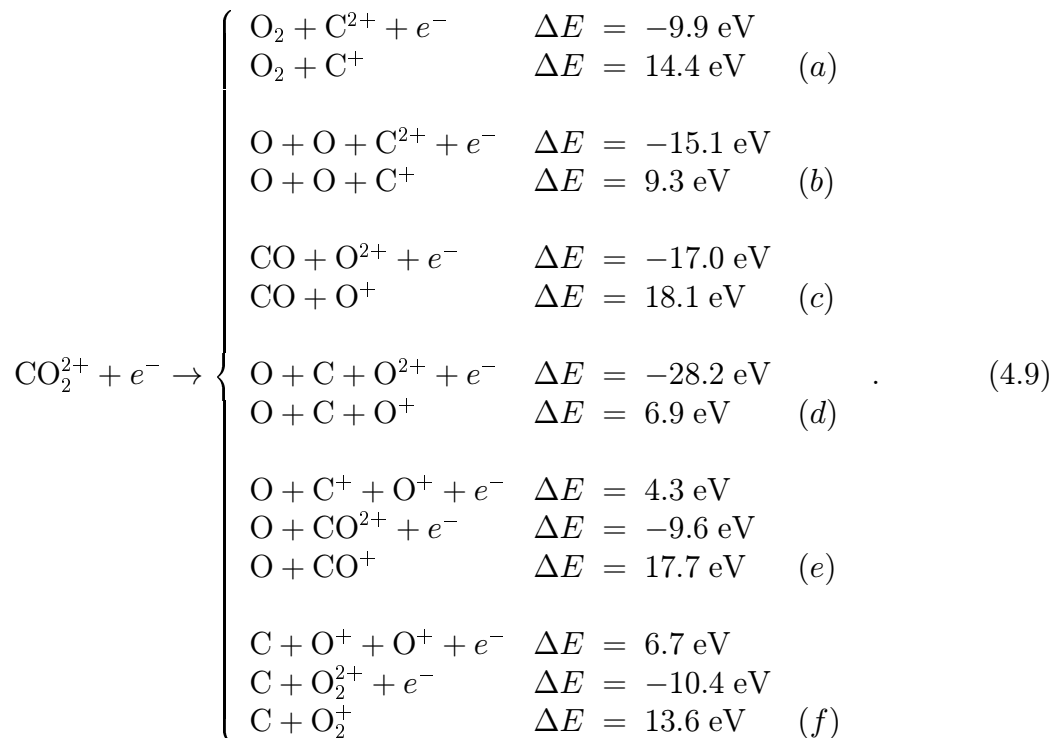
Table 4.1: Thermal rate coefficient ($\times 10^{-7} \text{ cm}^3\text{s}^{-1}$) at $T = 300 \text{ K}$ for DR of CO_2^+ .

previous measurements, yet we are still well within a two standard-deviation range of these results.

The possible outcome of the electron scattering process is different for the two ions. For CO_2^+ , the following channels may be considered at $E_{rel} = 0$:



where ΔE is the kinetic energy release for production of ground-state fragments. Note that the three-particle break-up channel (d) is energetically closed. For CO_2^{2+} , the situation is somewhat different. As with CO_2^+ , we only observe single capture of electrons which - contrary to the monocation - leaves charged fragments. Further, several dissociative excitation channels are energetically allowed even at $E_{rel} = 0$:



As expected, DR of a doubly-charged system releases on average more kinetic energy than the singly-charged equivalent.

A branching ratio analysis has been made using the grid technique. The individual peaks overlapped somewhat in the SSD spectrum for CO_2^+ , and the signal in each peak

was thus found by fitting Gaussian functions to the SSD peaks. The result for $E_{rel} = 0$ is given in Table 4.2.

a	b	c
$(4 \pm 3) \%$	$(9 \pm 3) \%$	$(87 \pm 4) \%$

Table 4.2: Result of branching ratio analysis for CO_2^+ at $E_{rel} = 0$.

The branching ratios clearly show that channel c (CO + O break-up) is dominant at low energy with a minor contribution from channel b . This is interesting, because the linear O-C-O molecule thus may break up into an O_2 molecule. The recombination energy of CO_2^+ is much more than the dissociation energy of the molecule, and thus channel a is believed to be 0. This is consistent with the present result within the error-bars. Furthermore, non-dissociative recombination has to our knowledge so far never been observed in any experiment.

For CO_2^{2+} , the peaks from the SSD were so well-resolved that we could use our standard data acquisition system (using single-channel analyzers) to count the signal events in all peaks. This allowed us to calculate branching ratios as a function of the relative collision energy. The branching ratios are seen in Fig. 4.6. The DR process appears to result in mainly two channels; c (CO production) and e (O production). The latter dominates at all energies but it abruptly increases to almost 100% just below 10 eV. As seen in Eq. 4.9, this could be the result of the opening of the $\text{O} + \text{CO}_2^{2+}$ dissociative excitation channel.

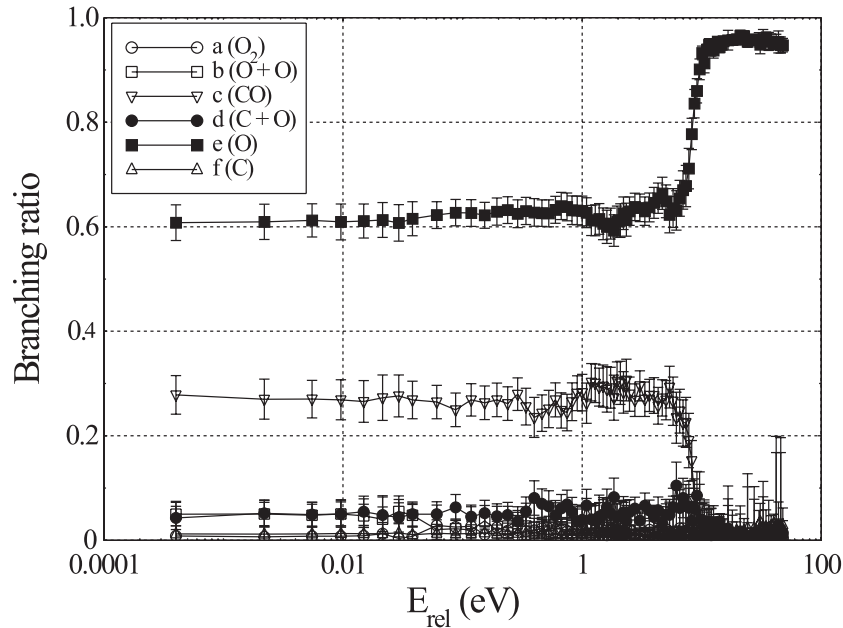


Figure 4.6: Dissociative recombination and dissociative excitation branching ratios for electron scattering on CO_2^{2+} .

4.3.2 N_2^+

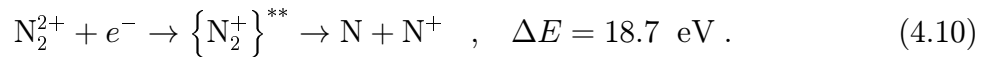
The N_2 molecule is believed to be quite abundant in the interstellar medium, and like CO_2 it is believed to be a major solid component of frozen grain mantles [171]. Clearly,

ionized states of this molecule is of great interest to plasma physics and the physics and chemistry of the atmosphere of Earth. The N_2^{2+} dication is known to play a role in high-energy atmospheric environments such as the ionosphere, and it has been the most studied of all dications, both experimentally and theoretically.

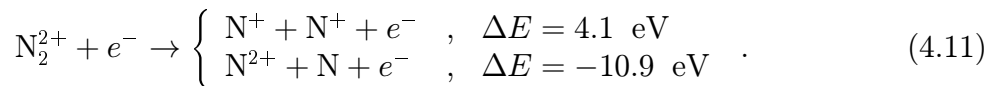
N_2^{2+} ions were produced from an $^{14}\text{N}^{15}\text{N}$ gas in a Nielsen type ion source, and ion currents of about 200 nA were extracted. The ions were stored in ASTRID at an energy of 9.87 MeV, resulting in a beam with a lifetime of about 1.5 seconds. The absolute current was measured using the current transformer, which revealed that about 125 to 150 nA of N_2^{2+} current was successfully stored in the ring.

We chose the $^{14}\text{N}^{15}\text{N}^{2+}$ isotope to make certain that we could distinguish between N_2^{2+} and N^+ ions in the magnetic analysis, since both ions have a mass-to-charge ratio of 14, if the naturally most abundant ^{14}N isotope is used. Also, the $^{14}\text{N}^{15}\text{N}^{2+}$ isotope is more radiatively active than the $^{14}\text{N}_2^{2+}$ ion, and this will allow the stored beam to decay to lower degrees of excitation before measurements commence.

The dissociative recombination of N_2^{2+} may be written as:



Dissociative excitation of N_2^{2+} may result in two different channels:



The SSD spectrum shows two peaks corresponding to ^{14}N and ^{15}N , and the absolute rate coefficient is shown in Fig. 4.7 as a function of the relative energy.

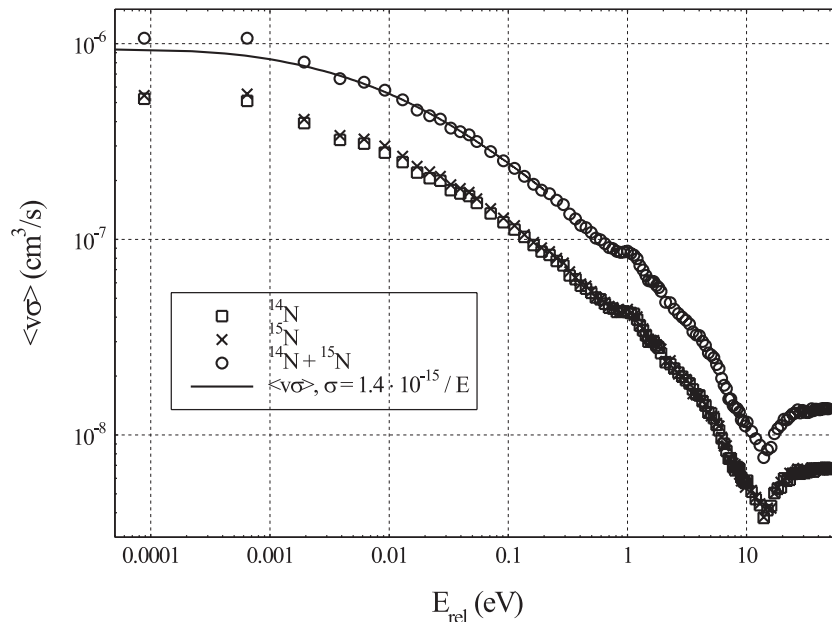


Figure 4.7: Measured absolute rate coefficients $\langle v\sigma \rangle$ for N_2^{2+} as a function of the relative energy. The solid curve is the calculated rate coefficient for $\sigma [\text{cm}^2] = 1.4 \cdot 10^{-15} \cdot \frac{1}{E[\text{eV}]}$.

The rate coefficient is observed to drop two orders of magnitude up to a center-of-mass energy of approximately 14 eV. A small resonance structure is seen at approximately 1 eV. This structure could be explained by the DR process proceeding through an electronically

excited state. In the figure, three different rate coefficients are seen. By only looking at the signal in one of the peaks in the SSD spectrum, we can individually determine the rate coefficient of reactions resulting in a neutral ^{14}N fragment or an ^{15}N fragment, respectively. We have also combined the signal in the two peaks, which in turn gives us the total rate coefficient. As can be seen in the figure, the rate coefficients for the two isotopes of N are identical within the uncertainties, and from this we conclude that no isotope effects are involved in the DR process

Notice that this experiment does not distinguish between the DR reactions of Eq. 4.10 and the DE reactions of Eq. 4.11. The first DE reaction will not give a signal because no neutral fragments are created, while the second reaction will give a signal similar to that of the DR process. This latter channel will, however, be closed at energies below 10.9 eV. Above this energy, an increase is observed which may be due to DE.

By comparing to model cross-sections convoluted with the electron cooler velocity distribution, we find:

$$\sigma(E) = 1.4 \cdot 10^{-15} \frac{1}{(E[\text{eV}])} \text{ cm}^2, \quad (4.12)$$

which is also plotted in Fig. 4.7. This yields a thermal DR rate coefficient of:

$$\alpha_{\text{N}_2^+} = (5.8 \pm 2.9) \times 10^{-7} \times \left(\frac{300}{T[\text{K}]} \right)^{0.5} \text{ cm}^3 \text{ s}^{-1}. \quad (4.13)$$

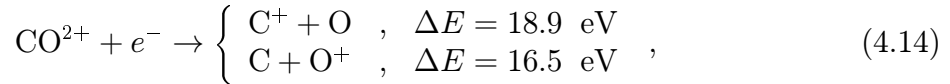
4.3.3 CO^{2+}

Besides H_2 , CO is the most abundant molecule in the universe, and is known to exist in many astrophysical environments. Any CO^+ produced such places will normally react with H_2 to form HCO^+ , but in regions where H_2 is ionized or dissociated by energetic photon, CO^+ may survive [180]. Possibly, CO_2^{2+} may also be created in these regions. Due to the flux of energetic photons, the density of free electrons must be high, and CO^+ and CO_2^{2+} ions are likely to be destroyed by dissociative recombination. While DR of CO^+ has received considerable attention [181, 182, 183], the only work done on CO_2^{2+} has to our knowledge been conducted at ASTRID.

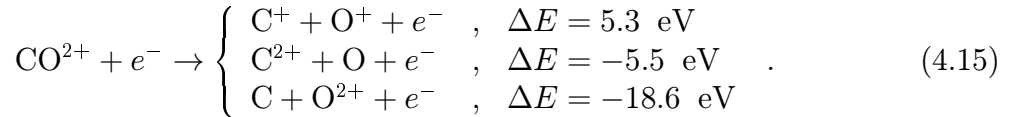
A few years ago, we published results on the DR rate coefficient for CO^{2+} [184, 185]. The experimental circumstances of that work were similar to the present. The CO^{2+} current was quite low, though; only about 100 nA was extracted from the ion source, and even less was successfully stored in the ring. This was too low for a BCM measurement of the ion current, and therefore we used the spectrum-analyzer (as described on page 64) to measure the absolute current.

After publication of the CO^{2+} results in 1999 we discovered a missing correction in the conversion of the spectrum-analyzer signal to ion currents, related to the relative ion velocities of the calibration beam and the CO^{2+} ion beam. The two ion beams were not stored with the same velocities, and this gave a natural shift in the spectrum-analyzer signal. The absolute calibration of the rate coefficient was thus too low. Since then, we have repeated the CO^{2+} measurement twice using the correct calibration formula. This new result will be presented in this section.

The DR of CO^{2+} may lead to two different channels:



while the DE process has one open channel at $E_{rel} = 0$ and two more channels opening up at higher energies:



The $^{13}\text{C}^{16}\text{O}^{2+}$ ions were produced in a Nielsen type ion source, and about 330 nA were extracted. The specific isotope was chosen to avoid contamination from N^{+} and N_2^{2+} ions. The beam was stored at 9.866 MeV, and the absolute rate coefficient was measured at two different relative collision energies. The result was used to recalibrate the previously measured data.

Though more current was extracted from the ion source during this experiment, an attempt to measure the stored current using the current transformer failed. Instead, the current was measured with the spectrum analyzer, and the final DR rate coefficient for CO^{2+} is presented in Fig. 4.8. The rate coefficient follows a smooth featureless curve, dropping two orders of magnitude from 10^{-3} eV to 10 eV. After a characteristic dip near 15 eV, it appears to be quite constant in the range from 25 to 80 eV.

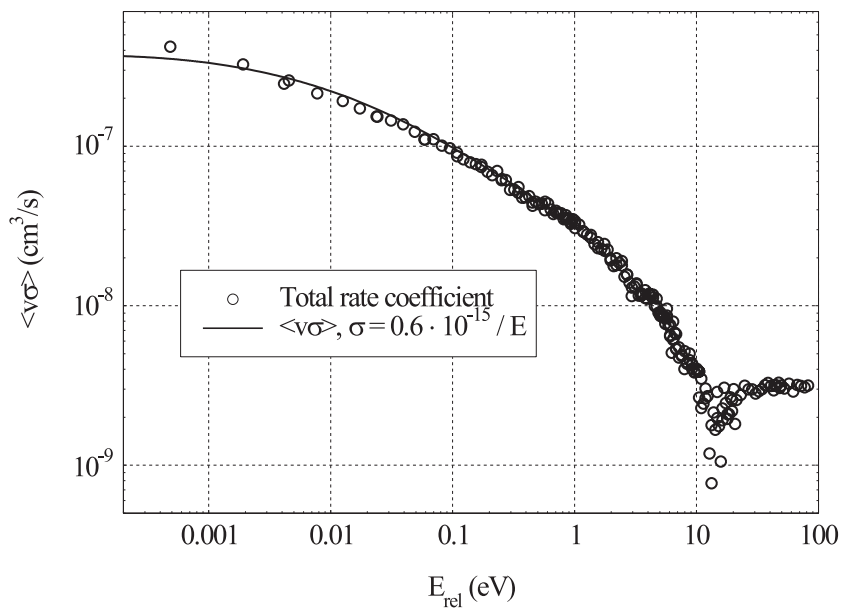


Figure 4.8: Measured absolute rate coefficients $\langle v\sigma \rangle$ for CO^{2+} as a function of the relative energy. The solid curve is the calculated rate coefficient for $\sigma [\text{cm}^2] = 0.6 \cdot 10^{-15} \cdot \frac{1}{E[\text{eV}]}$.

Again we have compared the measured rate coefficient to a model cross-section convoluted with the known electron cooler velocity distribution, yielding:

$$\sigma(E) = 6 \cdot 10^{-16} \frac{1}{(E[\text{eV}])} \text{ cm}^2. \quad (4.16)$$

Inserting this into Eq. 4.6, we find a thermal rate coefficient of

$$\alpha_{\text{CO}^{2+}} = (3.0 \pm 1.5) \times 10^{-7} \times \left(\frac{300}{T[\text{K}]} \right)^{0.5} \text{ cm}^3\text{s}^{-1}, \quad (4.17)$$

which is more than a factor of 3 higher than what was published earlier. Since this work only recalibrates the absolute scale of the CO^{2+} rate coefficient, further discussion about the CO^{2+} rate coefficient is referred to our previous article in Refs. [184, 185].

4.3.4 Comparison of monocation and dication results

At present, three ions have been studied as both singly and doubly-charged species, namely CO^{n+} , CO_2^{n+} and N_2^{n+} ($n = 1, 2$). The rate coefficients of these three dications and that of CO_2^+ have been measured at the ASTRID storage ring [179, 184, 185], while the rate coefficients for N_2^+ and CO^+ have been measured at CRYRING [181, 186]. The results of all these measurements are summarized in Table 4.3.

Molecule	Mono-cation	Di-cation
CO	$2.8 \times \left(\frac{300}{T[\text{K}]} \right)^{0.55}$	$3.0 \times \left(\frac{300}{T[\text{K}]} \right)^{0.5}$
CO_2	$6.5 \times \left(\frac{300}{T[\text{K}]} \right)^{0.8}$	$6.2 \times \left(\frac{300}{T[\text{K}]} \right)^{0.5}$
N_2	$1.8 \times \left(\frac{300}{T[\text{K}]} \right)^{0.3}$	$5.8 \times \left(\frac{300}{T[\text{K}]} \right)^{0.5}$

Table 4.3: Comparison of rate coefficients measured at storage rings; all are tabulated as $10^{-7} \text{ cm}^3\text{s}^{-1}$. We estimate the error bars to be about 50 percent for the dications and a little lower for the monocations.

Though the results of Table 4.3 clearly show that the rate coefficients are of similar magnitude, the error-bars of the absolute measurements prevent us from definitively concluding whether the dication rate coefficients are generally larger than the rate coefficients of the corresponding monocations.

It is particularly interesting to compare the temperature dependencies of the rate coefficients. It can be seen that all dications obey a $\sqrt{1/T}$ dependency, while the monocations diverge somewhat from this, being of the form $\propto T^b$, where b runs from -0.3 to -0.8. This temperature dependency is determined by the energy dependency of the cross-section. Solving Eq. 4.6 analytically for a cross-section $\sigma(E) \propto 1/E^a$, we find that the thermal rate coefficient obeys a temperature dependence of the form $\propto T^{0.5-a}$.

The ions CO^+ , CO_2^+ and N_2^+ are observed to have DR rate coefficient cross-sections proportional to $1/E^{1.05}$, $1/E^{1.3}$ and $1/E^{0.8}$, respectively. All dications have cross-sections proportional to $1/E$. This $1/E$ dependency of the neutral fragment production indicates that dissociative excitation is not important to electron scattering on dications at low energies since, in general, DE is expected to increase with increasing energy. Furthermore, this dependency is a typical sign that the DR mechanism is of the *direct* type [146].

4.4 Conclusion

In conclusion, dissociative recombination rate coefficients have been measured for CO_2^+ and CO_2^{2+} in the energy range from 10^{-3} eV to 10^1 eV. This is to our knowledge the first measurement of the DR rate coefficient for the CO_2 dication. From the data, thermal

rate coefficients of similar magnitudes are extracted. Furthermore, product branching ratios have been measured for CO_2^+ near zero center-of-mass energy, and for the CO_2^{2+} ion in the energy range from 10^{-3} eV to 50 eV. $\text{CO} + \text{O}$ breakup is dominant for DR of CO_2^+ , while neutral O is the main product of dissociative excitation and recombination of CO_2^{2+} . The measured thermal rate coefficient for DR of CO_2^{2+} has recently been applied in calculations predicting a CO_2^{2+} ion layer in the atmosphere of Mars [125, 126].

The DR rate coefficient has been measured for N_2^{2+} in the energy range from 10^{-3} eV to 50 eV. From these data, a thermal rate coefficient of $(5.8 \pm 1.7) \times 10^{-7} \text{ cm}^3\text{s}^{-1}$ was extracted. The $^{14}\text{N}^{15}\text{N}^{2+}$ ion was chosen because we thus avoid contamination from N^+ ions in the beam, and because of its improved ability compared to $^{14}\text{N}_2^{2+}$ to radiatively decay to the ground-state before the experiment. No isotope effects are observed. Furthermore, measurements on the CO_2^+ ion have been redone. Previously published results were calibrated to an absolute scale which was too low.

Finally, all known thermal rate coefficients measured for dications are summarized and compared to the corresponding monocation. The ions CO^+ , CO_2^+ and N_2^+ are observed to have dissociative recombination cross-sections proportional to $1/E^{1.05}$, $1/E^{1.3}$ and $1/E^{0.8}$, respectively. All dications have cross-sections proportional to $1/E$.

Chapter 5

Installation and test of ETRAP - an electron target for ELISA

This chapter describes preliminary test results obtained with the ETRAP electron target at ELISA. The storage ring was described in Chapter 2, which also contained an introduction to ETRAP and the experimental methods involved in measurements. This chapter will contain further details on the ETRAP design, and the first results from actual experiments are presented.

5.1 Introduction

In keeping with the structure of the previous chapters, this section includes both a general and a historical introduction.

5.1.1 General introduction

ETRAP has already been introduced in Chapter 2, and this section will instead describe some of the science, which is possible with the new electron target.

Following the discovery of X-rays by Röntgen, Becquerel investigated fluorescent materials to see if they also emitted X-rays. During the work he left a sample of uranium salt (pitchblende) on top of a photographic plate in a drawer, and later he noticed a faint image of the pitchblende. He had, by chance, discovered radioactivity. Marie Curie decided to study the “Becquerel rays” for her doctoral thesis topic, and together with her husband Pierre Curie, she discovered other materials that emitted radioactive radiation. The dangerous effects of radioactivity were unknown at the time, and Becquerel and the Curies all worked with no radiation protection. Marie Curie, especially, suffered from radiation disease, from which she later died.

The damage induced by ionizing radiation in living cells occurs via a series of reactions, which are initiated by the interaction of fast primary particles. Energy deposition by the latter particles has been fairly well understood for some time. Today, such data is particularly effective in calculating patient doses in radiotherapy. There existed for some time, however, a large gap of knowledge between our understanding of these primary events, which determine doses, and the slower chemical events which describe the products of ionizing radiation and causes of tissue damage.

A missing key element to bridge this crucial gap was the action of secondary electrons, which are created in large numbers and with low energies by ionizing radiation. Radiation

damage of biomolecules has been studied intensively by the group of Léon Sanche in Canada, who has found that most of the energy deposited by ionizing radiation in cells is channeled into the production of abundant free secondary electrons with energies between 1 and 20 eV. Genotoxic damage, such as single and double strand breaks in DNA, is not produced by the mere impact of direct primary high-energy radiation. Instead, the group has shown that the secondary electrons can induce substantial damage to biomolecular species [187, 188, 189], which challenges the traditional notion that electrons can only induce damage at energies above the onset of ionization.

The study of low-energy electron-impact on biomolecular systems are thus of fundamental interest to radiation health science, and the combination of ELISA and ETRAP is ideal for such studies.

5.1.2 Historical overview

The ETRAP electron target was designed and constructed as a part of the PhD project of Marie J. Jensen, my predecessor as a PhD student in the research group. Marie started planning the electron target in August of 1997. In October 2000, ETRAP had been finished and initial tests of the electron trap and beam mode could be conducted. After a half year of thorough investigations of the operational parameters of ETRAP, she finished her work which formed the basis of part of her thesis.

In August 2001, ETRAP was installed in ELISA and initial testing measured lifetimes of trapped electrons compared to the previous offline testing. The lifetimes were much lower, which was ascribed to the pressure being higher after installation in ELISA. Next, the effect of an electron beam on a stored ion beam was investigated. Turning the ETRAP solenoids on, immediately resulted in a loss of ions, but by using the electrostatic correction electrodes before and after ETRAP, a new ion beam could be stored, though with a lower lifetime. When a chopped electron beam was turned on, the lifetime of the ion beam was drastically reduced, and this was a significant problem for some time. A solution was found by increasing the anode-cathode distance in the electron gun. Apparently, too short a distance had resulted in some discharge phenomenon which had a destructive effect on the ion beam.

Thus, by October 2001 we were able to store ions simultaneously with a chopped electron beam, and a clear electron-induced signal could be observed on the neutral detector. The following year was spent on further tests and analysis of *e.g.* the ion beam lifetime, which was still too low. In 2002 ETRAP was removed from ELISA for a few months. A new filament was installed, and after re-installation into ELISA, the first measurements on NO_2^- were conducted. Also, what we believe to be the first electron scattering experiment on a negatively charged biomolecule in a storage ring was performed.

Finally, it should be mentioned that storage of biomolecular ions in an electrostatic storage ring has also been demonstrated in Japan and published in 2003 [190]. Singly-charged positive ions of *e.g.* insulin from bovine pancreas (5740 amu) and negative ions of adenosine triphosphate (587 amu) were successfully stored with lifetimes from 10 to 20 seconds. Moreover, electron scattering experiments have been performed at *e.g.* the University of Southern Denmark [191, 192, 193].

5.2 The electron target

The electron target has two modes of operation, beam mode and trap mode. In beam mode, an electron beam crosses the ion beam at a 90 degree angle. This mode of operation may be used for collision experiments of relative energies from a few eV and upwards. As described in Eq. 2.32, the crossed-beams setup does not permit zero relative energy, but if heavy biomolecules are studied, the ion beam contribution to the relative energy will typically be only a fraction of an eV, and the limiting factor is density of electron which is negligible below about 5 eV.

A schematic diagram of ETRAP is shown in Fig. 5.1.

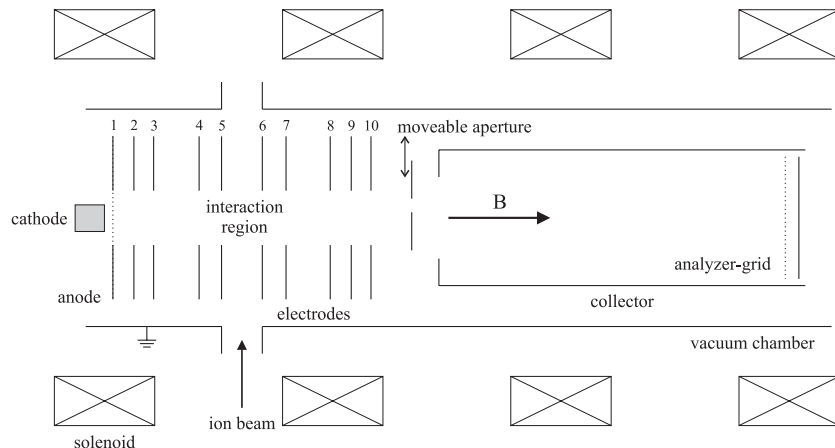


Figure 5.1: Schematic diagram of ETRAP. Except for the movable aperture, all parts of ETRAP are cylindrically symmetric. The numbers 1 to 10 are assigned to the anode and the confining electrodes between the electron emitting filament and the electron collector. The drawing is not to scale.

Electrons are delivered by a 15 mm diameter BaO coated tungsten cathode of the same type as the one mounted in the electron cooler at ASTRID. A negative acceleration voltage is applied to the cathode, which will then accelerate the thermally emitted electrons towards the grounded anode grid. A negative chopper voltage can be added to anode, which thus allows us to chop the electron beam.

A stack of 9 disc-shaped electrodes with central orifices are positioned in the region between the anode grid and the electron collector. The electron beam is confined in the interaction region by a ≈ 200 Gauss magnetic field supplied by four individually controlled solenoids, which guides the electrons from the anode through the holes of the electrode stack and into the collector. The electrode stack is used to supply the trapping potential for when ETRAP is operated in trap mode. In beam mode, all these electrodes are grounded. A photo of the electron gun and electrode stack is shown in Fig. 5.2.

The magnetic field of ETRAP will influence the ion beam, which it crosses at a 90 degree angle. Even a small magnetic field will cause a stored ion beam to be lost, and to correct for this, two pairs of small electrostatic deflector plates are positioned in the ELISA beamline right before and after ETRAP. A photo of ETRAP installed in ELISA is shown in Fig. 5.3.

Neutral fragments created in ETRAP are detected after the bending electrodes following the electron target. Another detector is located after the second bending electrode, and this can be utilized to monitor the beam current used for signal normalization. This

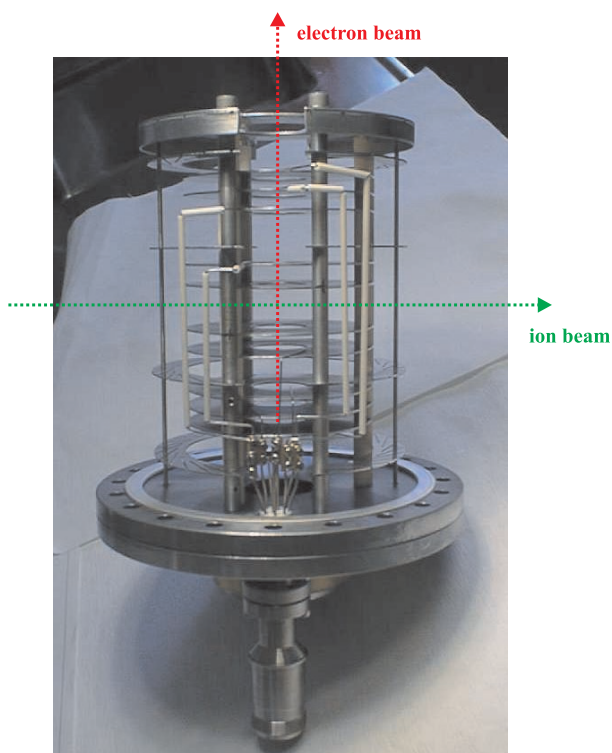


Figure 5.2: Photograph of the electron gun and electrode section of ETRAP. Ion and electron beams are indicated.

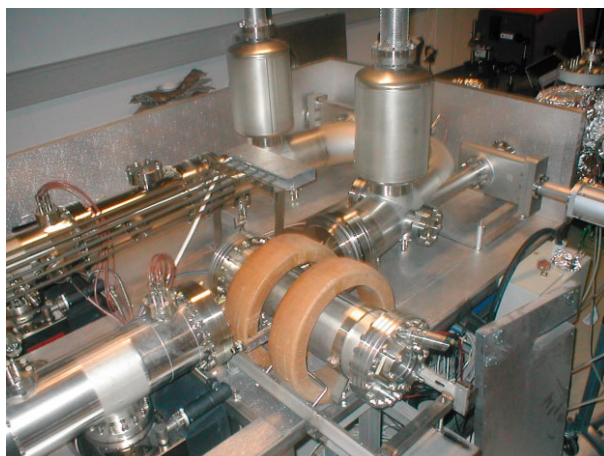


Figure 5.3: Picture of the electron target installed in ELISA. Only two of the four magnets are installed in this picture. The cathode is placed in the end pointing towards the middle of ELISA.

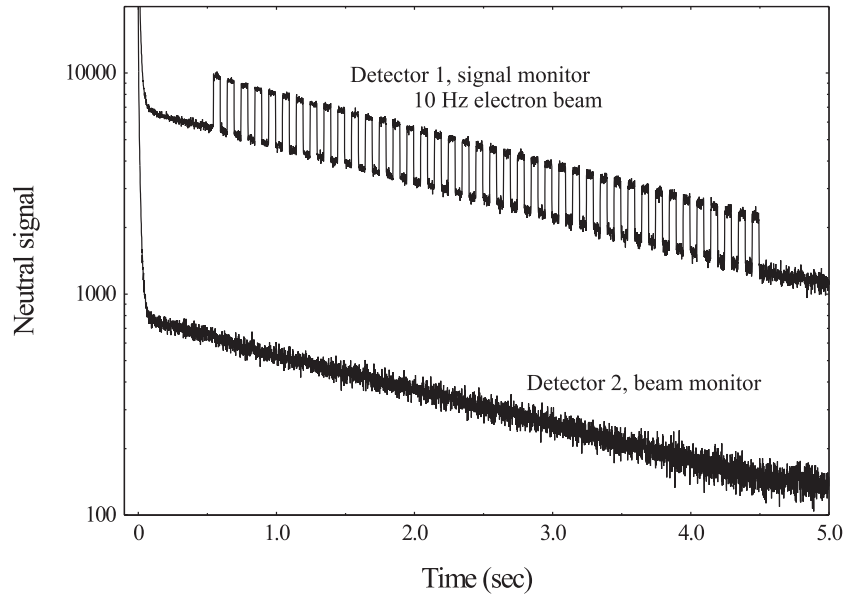


Figure 5.4: Electron-induced signal from ETRAP. Electrons are chopped at 10 Hz for 4 seconds.

is shown in Fig. 5.4, where a 10 Hz chopped electron beam has been scattered on a stored beam of CN^- ions. The electron-induced signal is very clear in this figure.

As described in section 2.3.2, the ions will traverse the entire range of different longitudinal electron energies induced by the space charge potential. In a simple approximation, we replace this correction with an effective space charge constant, K_{eff} , found from the experimental data.

As described in App. A, the space charge potential is calculated from the radii of the electron beam and the grounded stainless steel vacuum chamber. If we repeat this calculation for the ETRAP electrode configuration, we encounter the problem that the ETRAP chamber does not consist of smooth cylindrical wall concentric with the electron beam, since the electrons move through the center openings of the electrode stack. Instead of performing an exact electrostatic calculation of the space charge potential, we will be satisfied with an estimate of K_{eff} , which will finally be determined experimentally.

The inner orifices of the 9 grounded electrodes have a radius of 1.5 cm, which to a first approximation can be considered the wall of a virtual grounded vacuum chamber. Inserting this into the space charge calculation we get $K_{sp}(0) \approx 36$. However, the effective wall of the virtual chamber is probably a bit larger than the radius of the inner orifice. If *e.g.* we choose a radius of 2.5 cm, we get a space charge factor on the electron beam axis of $K_{sp}(0) \approx 52$. Thus, we might expect the effective space charge potential to be in the neighborhood of these values. An experimental value will be extracted below.

5.3 Results

To determine the effective space charge constant, and thereby to calibrate the axis of relative energies in an experiment, we initially performed an electron scattering experiment on a system, which was known from ASTRID experiments. Following this, we performed the first measurement of electron scattering on a biomolecular system.

NO_2^-

The NO_2^- ion has previously been studied at ASTRID, as described in Chapter 3. This ion is particularly well-suited for a comparison between ASTRID and ELISA, because the energy scale can be calibrated using both the detachment threshold and two resonance positions.

The ions were produced in a CCIS discharging in atmospheric air. The detachment cross-section was measured from 3 to 48 eV, and this is shown in Fig. 5.5 together with the data from ASTRID.

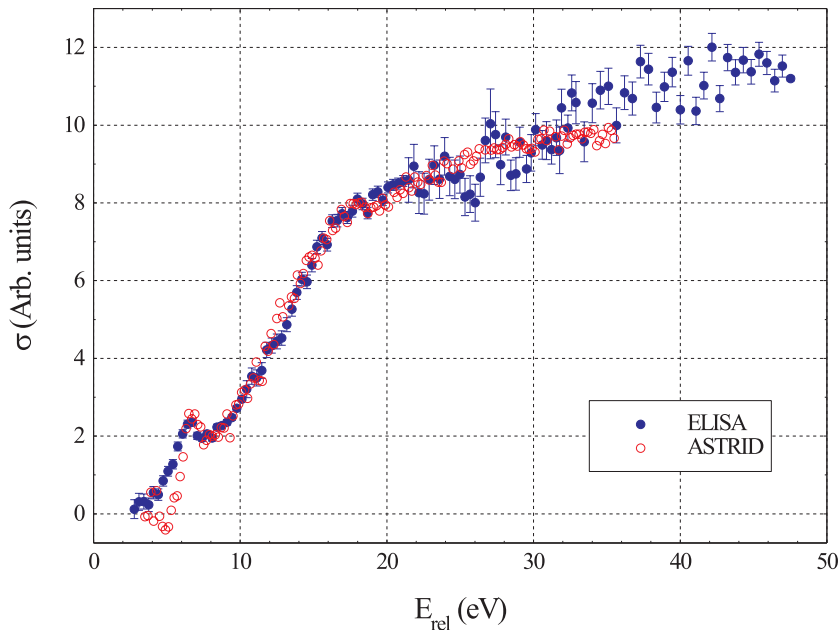


Figure 5.5: The cross-section for electron scattering on NO_2^- measured at ELISA and compared to the ASTRID data of Fig. 3.8.

Clearly, very good agreement is found and as expected the resonances appear wider in the ELISA data due to the lower resolution of the ETRAP setup.

The space charge constant has been found by analyzing the data with different values of K_{eff} . We have applied a special acceleration technique of the electrons, where we vary the anode potential instead of having it grounded. The electrons will thus only experience a part of the acceleration voltage V_{acc} between the cathode and the anode. If *e.g.* the cathode is on $V_{acc} = -40$ V, and the anode is on -30 V, the electrons are only accelerated to 10 eV (neglecting space charge contribution) between the cathode and the anode. After the anode, however, the electrons still experience a ground potential which further accelerates the electrons, and the final electron energy is the full 40 eV expected from the acceleration voltage.

This has an important consequence: the electron beam follows Child's Law as described by Eq. 2.2, but applied to the cathode-anode potential difference. Thus, by applying a bias voltage to the anode grid, we can produce two beams of different electron currents at the same final acceleration voltage, without changing any other parameters of the electron beam. We are then able to measure the cross-section in overlapping energy intervals, but with different electron currents (and thus different space charge correction). By analyzing the data for several values of K_{eff} , we find the effective space charge constant for which the overlapping cross-section scans converge.

This is demonstrated in Fig. 5.6, where three energy scans from the NO_2^- data have been analyzed using two different space charge constants.

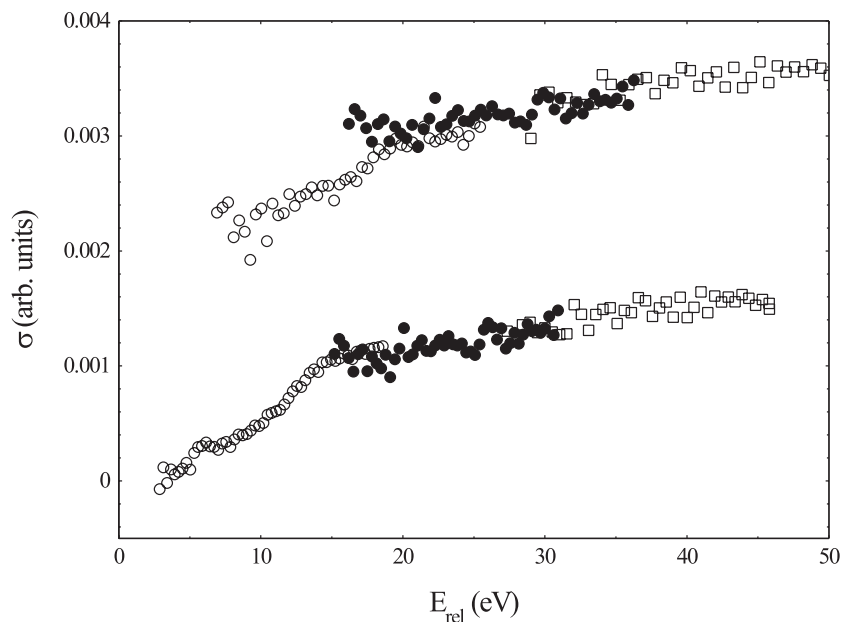


Figure 5.6: Experimental determination of K_{eff} from overlapping scans with different space charge corrections. Upper curve (which is offset 0.002 for clearness) is calculated with $K_{eff} = 35$ and the lower curve with $K_{eff} = 60$.

A more thorough analysis using more scans have determined K_{eff} to be around 50.

In the NO_2^- data, a small acceleration voltage offset of about 2 V will have to be applied to achieve overlap between ASTRID and ELISA data. This offset had also been found in other test systems, and it appears to be a machine dependent constant. It is also observed in energy analysis of the electron beam, where a retarding potential is applied to the analyzer-grid in the collector (see Fig. 5.1). The full understanding of this offset is yet unclear, but most likely the offset is due to contact potentials or work function effects in the cathode. Further energy calibrations are planned in future experiments.

AMP⁻

The *in vitro* environment of biomolecules is typically that of a solution, but gas-phase investigations of biomolecules may add significant knowledge about these important species. ELISA has been constructed with the study of heavy biomolecules as one of the primary objectives, and the combination of the electrospray ion source and the ELISA storage ring has proven a very valuable tool [56]. So far, several photoabsorption studies have been performed with great success [194, 195], and many more are being planned, because the technique will reveal detailed understanding of intrinsic molecular properties, and comparisons with the solution phase behavior may elucidate the role of the solvent.

The first biomolecule chosen for an electron scattering experiment at ELISA was adenosine 5'-monophosphate (AMP). AMP is an intermediary substance formed during the human body's process of creating energy in the form of adenosine 5'-triphosphate (ATP) from food, and it is thus an essential component in the chemistry life. The molecule has previously been studied at ELISA in laser absorption measurements [196] making it an obvious choice for the first experiment.

The anion ion of AMP was created from a solution in the electrospray ion source. The very nature of the electrospray process will cause this molecule to detach a proton instead of attaching an electron, and the ion studied is subsequently called the *deprotonated* AMP anion. The electron scattering cross-section has been measured in the energy range from 4 to 140 eV, and this is presented in Fig. 5.7.

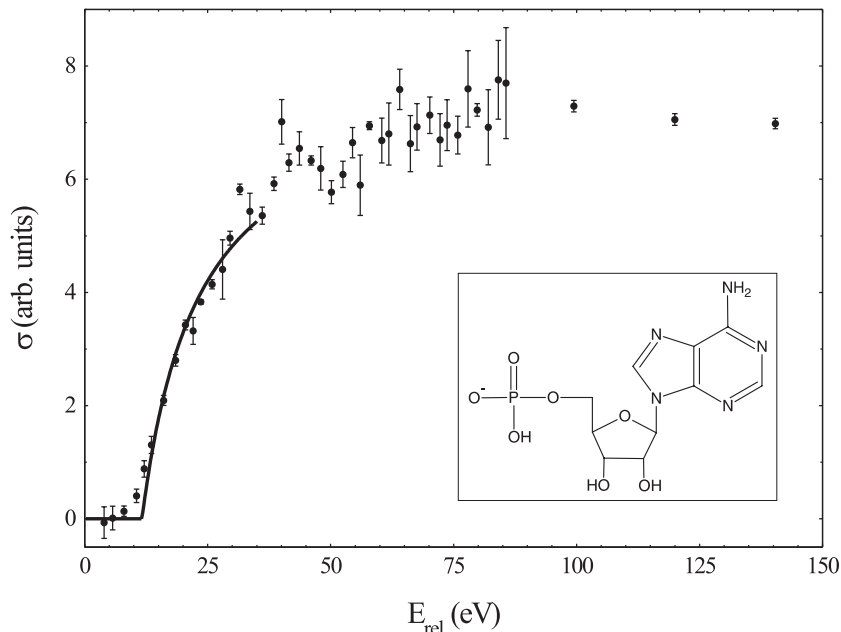


Figure 5.7: The cross-section for electron scattering on AMP^- measured at ELISA. Inset shows the molecular structure of the AMP^- ion.

The data have been calculated using a space charge constant of $K_{\text{eff}} = 47$ and a 2 eV offset. The cross-section is zero at low energies, and it then begins to increase above energies of 10 eV. It increases to a maximum somewhere between 70 to 90 eV, and the begins to decrease slowly again. This is the same cross-section shape found for previously studied systems (Chapter 3).

The classical detachment model used successfully on small atomic and diatomic systems is also fitted to the AMP^- data, which show a very good agreement in the threshold region. A threshold of 11.6 eV is found, and this corresponds to about 2.2 times the EA of the AMP molecule (which is 5.2 eV according to a calculation by the GAUSSIAN-98 software). This is particularly interesting, because the deviation from the classical model of Eq. 3.6 is no larger than that of the small polyatomic ions present in this thesis. More studies of electron scattering on biomolecules are necessary to investigate this further.

5.4 Conclusion

The electron target at ELISA has now proved able to measure electron scattering reactions using the cross-beams setup, and measurements of electron-impact detachment of NO_2^- has allowed us to compare results between ASTRID and ELISA. Moreover, electron-impact detachment of AMP^- has been performed, and this is to our knowledge the first electron scattering experiment on a large negative biomolecular system in a storage ring.

Many future experiments using ELISA to study biomolecules are being planned. Biomolecular photoabsorption experiments are ongoing at present, and the ETRAP is con-

tinously being developed and further tested. More test systems known from ASTRID as well as other biomolecular systems have already been measured. Further study of the 2 eV offset in the energy calibration is ongoing.

In future experiments, the imaging detector could be used as a position-sensitive detector, where a camera takes pictures of the particle impacts on the phosphorus screen. This may yield a distribution of fragment distances, which in turn is a measure of the kinetic energy release in particle break-up reactions. This can *e.g.* be used to extract branching ratios from electron scattering experiments at ELISA, something that at ASTRID is done with the energy-sensitive SSD. The imaging technique has, however, previously been applied at ASTRID experiments also [124], but the crossed-beams setup at ELISA does offer one advantage over ASTRID; the distance on the detector between neutral fragments, which is used to extract the kinetic energy release, is dependent on the known distance from the interaction region to the detector. The merged-beams setup at ASTRID is characterized by a large interaction region, and this has the implication that distribution of distances is smeared considerably. In ETRAP, the interaction region is only the size of the diameter of the electron gun cathode, and this much more localized source of neutral fragments result in a significant improvement of the resolution.

Chapter 6

Summary

The present thesis describes experimental investigations of gas-phase ionic species. Both negative and positive ions are studied using heavy-ion storage rings.

Relative cross-sections for electron scattering on a number of negatively charged ions have been measured in the energy range from 0 to about 50 eV. All cross-sections exhibit a well-defined onset at some threshold energy, which is significantly larger than the electron affinity of the corresponding molecule. This is consistent with a classical reaction model.

The relative detachment cross-sections have been measured for the atomic ions Cl^- and S^- . The Cl^- threshold has also been measured at CRYRING, and a deviation from the classical prediction of the threshold position is ascribed the relatively large tunneling contribution near the threshold. The choice of energy interval that is used for the theoretical fit, appears to have a significant effect on the extracted threshold. Other atomic ions exhibit less tunneling contribution, and the agreement with the classical threshold prediction is better.

Absolute detachment cross-sections have been measured for the isoelectronic diatomic ions CN^- and BO^- . A resonance is seen in the CN^- cross-section, but not in the BO^- cross-section. It is not clear why this is the case. Relative cross-sections have been measured for the four polyatomic ions, O_3^- , NO_2^- , NO_3^- and SO_2^- , and only the NO_2^- result is calibrated to an absolute scale. The cross-sections exhibit a good agreement with the classical model. Two resonances are observed for NO_2^- and one resonance for NO_3^- .

The dominating channel for molecular break-up is the pure detachment channel, except for O_3^- below relative energies of 13 eV, where the $\text{O}_2 + \text{O}^-$ channel dominates. All ions exhibit negligible three- and four-particle break-up.

We plan to extend the study of negative ions to anions clustered with water molecules. We can thereby investigate the border between negative gas-phase ions and anions in solution, where polarization interactions can help to stabilize the formation of doubly-charged anions. These experiments are planned for both ASTRID and ELISA.

For positive ions, the rate coefficients have been measured for CO_2^+ and CO_2^{2+} in the energy range from 10^{-3} eV to 10^1 eV, and thermal rate coefficients of similar magnitudes are extracted. $\text{CO} + \text{O}$ break-up is dominant for DR of CO_2^+ , while neutral O is the main product of dissociative excitation and recombination of CO_2^{2+} . The measured thermal rate coefficient for DR of CO_2^{2+} has recently been applied in calculations predicting a CO_2^{2+} ion layer in the atmosphere of Mars [125, 126].

The DR rate coefficient has been measured for N_2^{2+} in the energy range from 10^{-3} eV to 50 eV. From these data, a thermal rate coefficient of $(5.8 \pm 1.7) \times 10^{-7} \text{ cm}^3\text{s}^{-1}$ was

extracted. Also, measurements on the CO^{2+} ion have been redone in order to re-calibrated previously published data. We have finally compared all known thermal rate coefficients to those of the corresponding monocations. Presently, no more dication measurements are planned at ASTRID.

As illustrated by the ASTRID experiments presented in this thesis, storage rings in combination with the merged-beams technique are very well-suited for studies of electron-ion interactions. However, the technique employed at ASTRID is limited to studies of ions of masses below about 90 amu. Above this mass, it is difficult to produce electrons at near-zero relative energy, and the energy-sensitive solid-state detectors cannot resolve the neutral fragments peaks. When one wishes to study very heavy ions, the electrostatic low-energy storage ring ELISA is very suited. Preliminary results of electron scattering on NO_2^- and AMP^- ions have been presented.

Chapter 7

Dansk resumé

Såfremt læseren af denne afhandling ikke har den nødvendige faglige baggrund for at forstå indholdet, så har han eller hun måske for længst opgivet at følge med i teksten, og måske er lysten til at rive denne afhandling i stykker blevet stadig større i takt med sidetallenes skiften. Hvad er alle disse molekyler og atomer for nogen, og hvorfor har forfatteren brugt så mange år på at studere dem? Bare rolig! I dette kapitel vil jeg prøve at forklare afhandlingens indhold, så alle kan følge med.

Lad os først antage, at læseren virkelig river afhandlingen i stykker (jeg håber, at vi lader dette forblive et tankeeksperiment). Spørgsmålet er nu, om man til evig tid kan fortsætte med at rive papiret over, og derved lave mindre og mindre papirstykker - eller kommer man til et tidspunkt, hvor man sidder med det *mindste* stykke papir, der findes? Det vil sige, er papir opbygget af små mini-papirenheder, som alt andet papir er opbygget af, og som i sig selv ikke kan deles i to?

Svaret er ja! Papir - og alle andre materialer - er faktisk opbygget af meget små byggesten, som ikke kan deles i mindre enheder. Disse byggesten kaldes atomer og molekyler, og de udgør de mindste byggesten, som alt andet her på Jorden er opbygget af. Helt grundlæggende så findes der 92 slags atomer frit i naturen, og ud fra alle disse atomer kan man så opbygge hele den verden, vi lever i til daglig. Læseren kender formentlig navnene på nogen af disse atomer, for eksempel brint, ilt, kvælstof og kulstof.

Der findes dog ikke noget papir-atom, og det er netop her vi har brug for *molekyler*. Et molekyle er en lille sammensat gruppe af atomer, som udgør byggestenene for de fleste af de materialer, vi omgiver os af. For eksempel er vandmolekylet den mindste mængde vand, der findes, og dette molekyle er sammensat af 2 brintatomer og et iltatom (H_2O). Tilsvarende er et iltmolekyle (O_2) opbygget af to iltatomer, mens kuldioxid (CO_2) er opbygget af et kulstofatom og to iltatomer. Papir består hovedsagligt af nogle meget lange molekyler kaldet cellulose, der igen er opbygget af kulstofatomer, brintatomer og iltatomer. Cellulose er også en vigtig bestanddel af planter, og det er netop derfor vi kan fremstille papir ud fra træer.

Allerede de gamle grækere gjorde sig tanker om stoffets mindste byggesten, og ordet atom stammer faktisk fra det græske *átomos*, som betyder *udelt*. I dag ved vi dog godt, at også atomer kan opdeles i mindre dele, idet et atom er opbygget af en kerne af positive protoner og neutrale neutroner, der er omgivet af negative elektroner. Når vi kommer så langt ind i stoffets struktur, så kan vi dog slet ikke genfinde egenskaberne fra de ting, vi omgiver os af i hverdagen, såsom vand og luft. Der findes vandmolekyler, men der findes ikke vandatomer, vandelektroner og vandprotoner. Så når man studerer molekyler, så studerer man nogle af naturens mest grundlæggende byggesten, og enhver viden om

molekyler kan hjælpe os til bedre og bedre at forstå den verden, vi lever i.

Vores egen atmosfære består hovedsageligt af ilt (O_2) og kvælstof (N_2) molekyler, men der findes også en lang række af andre molekyler som for eksempel CO_2 (kuldioxid), NO_2 , SO_2 (svovldioxid) og O_3 (ozon). Om dagen vil solens lys påvirke disse molekyler, og resultatet er ofte, at en eller flere elektroner løsriver fra molekylerne, hvorved der dannes en positiv *ion* og en fri elektron. Denne blanding af ioner og elektroner kaldes et *plasma*. Om natten vil solens lys mangle, og elektroner og ioner har mulighed for at samles igen - rekombinere - til neutrale molekyler. Ofte vil molekylet under rekombinationen gå i stykker, en proces der kaldes *dissociativ rekombination*.

Det er dog ikke kun positive ioner, der findes i et plasma. Der er også mange negative ioner, hvor molekylet har bundet en ekstra elektron fast til sig. Også disse negative ioner vil kolliderer med elektroner, og hvis kollisionensenergi er stor nok, så vil den negative ion miste sin overskydende elektron og blive neutral. Ofte vil molekylet endda samtidig gå i stykker (dissociere) til to eller flere fragmenter.

Disse processer finder ikke bare sted i vores egen atmosfære, men også i atmosfærerne på andre planeter samt i interstellart stof, gaståger langt ude i universet. I stedet for at rejse ud til Mars for at studere kemien i atmosfæren eller at rejse langt ud i galaksen for at studere universets molekylære sammensætning, så har vi mulighed for at studere mange af disse processer i laboratoriet. Dette gør vi med en såkaldt *lagerring*.

En lagerring er et apparat, der kan lagre elektrisk ladede partikler som for eksempel negative elektroner eller positive og negative ioner. Dette gøres i lagringen ASTRID (se Fig. 2.1) ved hjælp af magnetiske felter og i lagringen ELISA (se Fig. 2.11) ved hjælp af elektriske felter. I de to lagringe har vi mulighed for at udføre kollisioner mellem elektroner og ioner. I ASTRID foregår forsøgene ved, at en stråle af elektroner overlappes med ionstrålen i lagringen over et område på ca. 1 meter. Ved at ændre hastigheden af elektronerne for en fast ionhastighed, så kan vi studere reaktionerne for forskellige kollisionensenergi. Når elektronerne og ionerne bevæger sig med samme hastighed, så er kollisionensenergi 0, og når elektronerne bevæger sig hurtigere, så er kollisionensenergi større end 0. I ELISA har vi en lidt anden opstilling, hvor elektron- og ionstrålen skærer hinanden i en vinkel på 90 grader, men grundidéen er den samme: Ladede ioner og elektroner kolliderer under kontrollerede forhold, og vi kan i ro og mag studere udfaldet. Med en lagring kan vi altså sidde i vores laboratorium og studere processer, der foregår både i den øverste del af Jordens atmosfære og langt ude i verdensrummet! Det tekniske apparatur, der er blevet anvendt i arbejdet, er præsenteret i kapitel 2.

Når elektronen er kollideret med ionen, så vil der typisk skabes en mængde neutrale partikler. Disse neutrale partikler vil bevæge sig ud af lagringen, som jo kun kan holde på ladede partikler. Vi sørger så for at placere en detektor, der identificere de neutrale partikler, der skabes. I praksis kommer der også en masse neutrale fragmenter ud fra lagringen, selv om elektronstrålen er slukket. Dette giver et *baggrundssignal*, som skyldes, at ionerne i lagringen kolliderer med forskellige restmolekyler, der findes i vacuumkammeret. Vi sørger derfor for at tænde og slukke for elektronstrålen meget hurtigt, hvorved vi kan skelne mellem rigtigt signal og baggrundssignal. Et signal fra vores detektor kan for eksempel ses i Fig. 2.9.

Den parameter vi måler kaldes et *reaktionstværsnit*. Tværsnittet er et mål for, hvor sandsynlig en given reaktion er, og i teorien er denne størrelse ganske simpel at måle. Man tager sin ion og beskyder den med elektroner, og så tæller man, hvor mange af de indkommende elektroner, der forårsager en reaktion. Forholdet mellem antallet af reaktioner per sekund og mængden af indkommende elektroner er så vores ønskede tværsnit. Helt præcist

måler man mængden af indkommende elektroner ved at gange antal elektroner per kubikcentimeter sammen med elektronernes hastighed, og derved bliver enheden for tværsnit faktisk kvadratcentimeter. Og det er selvfølgelig derfor, man kalder det et tværsnit i stedet for en reaktionsandsynlighed.

I denne afhandling har jeg præsenteret resultater fra to typer af eksperimenter: Kollisioner mellem elektroner og dobbeltladede positive ioner samt kollisioner mellem elektroner og enkeltladede negative ioner. Tværsnittene for de to processer er vidt forskellige. Negative ioner (kapitel 3) har et tværsnit på 0 ved lave kollisionsenergier, og ved en given tærskel vokser tværsnittet så op. Dette kan forklares ganske intuitivt, for ved lav kollisionsenergi har den indkommende elektron slet ikke nok energi til at løsrive den negative ions overskydende ladning. Den negative ion og den negative elektron vil nemlig frastøde hinanden, og vi ser dermed ingen reaktioner, og det målte tværsnit er følgelig 0. Jeg har i afhandlingen vist, at positionen af tærskelen i tværsnittet kan findes ved hjælp af en bemærkelsesværdigt simpel teori. Teorien er ganske god for meget små ioner, men den passer mindre godt for større ioner. Dette er i overensstemmelse med vores forventninger.

I kapitel 4 præsenteres resultater fra kollisioner mellem elektroner og positivt ladede ioner. Mere specifikt drejer det sig om dobbeltladede molekyllære ioner, altså molekyler der har mistet to af sine elektroner. For disse positive ioner ser tværsnittet helt anderledes ud. Her er reaktionstværsnittet højest ved lavest energi, og så falder det ellers kraftigt, når kollisionsenergien vokser. Så vidt vides er dette de første målinger af tværsnit for dobbeltladede, positive molekyllioner. Alle tidligere målinger har fokuseret på enkeltladede ioner, og i afhandlingen har jeg netop udvalgt tre forskellige molekyler, hvis enkeltladede reaktionstværsnit sammenlignes med det dobbeltladede tværsnit.

I denne afhandling præsenteres ikke kun målinger af reaktionstværsnit. Vi har også studeret, hvilke fragmenter molekylerne bliver til, når de går i stykker. Som eksempel kan en negativ ozon-ion (O_3^-), der kolliderer med en elektron, gå i stykker til både ($O_2 + O$) og ($O + O + O$). Vi anvender en særlig teknik, der gør det muligt for os at skelne mellem de forskellige *kanaler*, som de mulige reaktionsprodukter kaldes. For negative ioner ser vi tydeligt, at den vigtigste kanal er en ren løsrivelse af elektronen uden at molekylet går i stykker. For ozon betyder det, at O_3^- primært bliver til $O_3 + e^-$. Ydermere ser vi, at hvis molekylerne endelig går i stykker, så vil det typisk kun dreje sig om to fragmenter, hvorimod kanaler med tre fragmenter er meget små.

I kapitel 5 har jeg beskrevet elektronkanonen i lagerringen ELISA. Denne elektronkilde er udviklet i vores gruppe, og jeg har været med til at installere den i ELISA og lave de første forsøg. I ELISA har vi mulighed for at lagre tunge biomolekyler, og det forsøg, hvor vi beskyder et negativt ladet biomolekyle med elektroner, er så vidt vides det første af sin slags i verden. Mens dette skrives, er mine kollegaer i gruppen allerede godt i gang med at lave flere forsøg af samme slags, og fremtiden ser meget spændende ud inden for dette felt.

Appendix A

Space charge potential

This appendix presents a thorough derivation of the space charge potential for a beam of electrons (Eq. 2.6).

The space charge of the electrons already in the interaction region cannot be ignored when calculating the electron energy in the cooler. The electron beam can be described as a cylinder of uniform charge density ρ_0 with radius a , coaxial with the grounded stainless steel vacuum chamber of radius R :

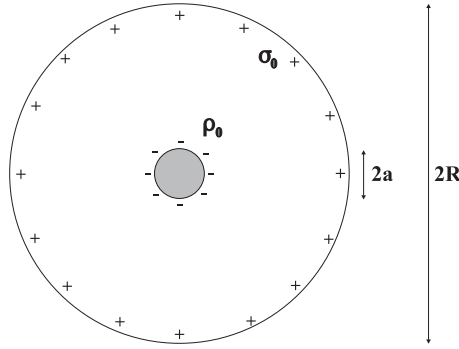


Figure A.1: Schematic diagram of the electron beam inside the grounded stainless steel vacuum chamber.

As indicated in Fig. A.1, the negative electrons induce a positive surface charge density σ_0 on the inside of the beam pipe, thus allowing the beam pipe to be on the ground potential. This is satisfied only if:

$$\pi a^2 \rho_0 + 2\pi R \sigma_0 = 0 \Leftrightarrow \sigma_0 = -\frac{a^2 \rho_0}{2R}. \quad (\text{A.1})$$

The electric potential V must obey the Poisson Equation:

$$\nabla^2 V = \begin{cases} -\frac{\rho_0}{\epsilon_0} & \text{for } 0 \leq r \leq a \\ 0 & \text{for } a \leq r \leq R \end{cases}. \quad (\text{A.2})$$

In cylindrical coordinates, the Laplace-operator takes the form:

$$\nabla^2 = \frac{1}{r} \frac{\partial}{\partial r} \left(r \frac{\partial}{\partial r} \right) + \frac{1}{r^2} \frac{\partial^2}{\partial \phi^2} + \frac{\partial^2}{\partial z^2}, \quad (\text{A.3})$$

but since the partial derivatives with respect to ϕ and z vanishes, we are left with the following simple differential equation:

$$\frac{1}{r} \frac{\partial}{\partial r} \left(r \frac{\partial}{\partial r} \right) V(r) = \begin{cases} -\frac{\rho_0}{\epsilon_0} & \text{for } 0 \leq r \leq a \\ 0 & \text{for } a \leq r \leq R \end{cases}, \quad (\text{A.4})$$

which has the following complete solution:

$$V(r) = \begin{cases} k_1 \ln r + k_2 - \frac{\rho_0}{4\epsilon_0} r^2 & \text{for } 0 \leq r \leq a \\ k_3 \ln r + k_4 & \text{for } a \leq r \leq R \end{cases}. \quad (\text{A.5})$$

The constants k_i can be determined by boundary conditions. The electric field at $r = R$ can be determined from the following Gauss surface:

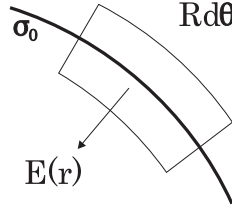


Figure A.2: Gauss surface used to determine the electric field at $r = R$.

The total charge inside the surface is $dQ = \sigma_0 R d\theta dz$, and Gauss' Law gives the following relation:

$$E(R) R d\theta dz = -\frac{\sigma_0}{\epsilon_0} R d\theta dz, \quad (\text{A.6})$$

from which we can determine the electric field in combination with Eq. A.1:

$$E(R) = -\frac{\sigma_0}{\epsilon_0} = \frac{\rho_0 a^2}{2\epsilon_0 R}. \quad (\text{A.7})$$

This makes it possible to determine k_3 :

$$\begin{aligned} E(R) = -\left(\frac{dV}{dr}\right)_{r=R} &\Rightarrow \frac{\rho_0 a^2}{2\epsilon_0 R} = -\frac{k_3}{R} \\ &\Rightarrow k_3 = -\frac{\rho_0 a^2}{2\epsilon_0} \end{aligned} \quad (\text{A.8})$$

Further, at $r = R$, the potential is zero due to the grounding of the beam pipe:

$$\begin{aligned} V(R) = k_3 \ln R + k_4 = -\frac{\rho_0 a^2}{2\epsilon_0} \ln R + k_4 = 0 \\ \Rightarrow k_4 = \frac{\rho_0 a^2}{2\epsilon_0} \ln R. \end{aligned} \quad (\text{A.9})$$

This leaves us with the following expression for $V(r)$:

$$V(r) = -\frac{\rho_0 a^2}{2\epsilon_0} \ln r + \frac{\rho_0 a^2}{2\epsilon_0} \ln R = -\frac{\rho_0 a^2}{2\epsilon_0} \ln \left(\frac{r}{R} \right) \quad \text{for } a \leq r \leq R. \quad (\text{A.10})$$

We now demand $V(r)$ and $E(r)$ to be continuous at $r = a$:

$$\begin{aligned} V(a) &= -\frac{\rho_0 a^2}{2\epsilon_0} \ln \left(\frac{a}{R} \right) = k_1 \ln a + k_2 - \frac{\rho_0}{4\epsilon_0} a^2 \\ E(r) &= \left(-\frac{dV}{dr} \right)_{r=a} = \frac{\rho_0 a^2}{2\epsilon_0 a} = -\frac{k_1}{a} + \frac{\rho_0 a}{2\epsilon_0} \end{aligned}, \quad (\text{A.11})$$

which yields:

$$\begin{aligned} k_1 &= 0 \\ k_2 &= -\frac{\rho_0 a^2}{4\epsilon_0} \left(2 \ln \frac{a}{R} - 1 \right). \end{aligned} \quad (\text{A.12})$$

The potential thus takes the final form:

$$V(r) = -\frac{\rho_0 a^2}{4\epsilon_0} \begin{cases} \left(\frac{r}{a} \right)^2 + 2 \ln \left(\frac{a}{R} \right) - 1 & \text{for } 0 \leq r \leq a \\ 2 \ln \left(\frac{r}{R} \right) & \text{for } a \leq r \leq R \end{cases}. \quad (\text{A.13})$$

This is the space charge potential of the electron beam. Instead of using the electron charge density ρ_0 , it is better to use the magnitude of the electron current I_e and the laboratory energy E_e^{lab} :

$$(-I_e)dt = dQ = \rho_0 \left(\pi a^2 \sqrt{\frac{2E_e^{lab}}{m}} dt \right) \quad (\text{A.14})$$

$$(\text{A.15})$$

$$\Rightarrow \rho_0 a^2 = -\frac{I_e}{\pi} \sqrt{\frac{m}{2E_e^{lab}}}, \quad (\text{A.16})$$

Inserting this into the space charge potential yields:

$$V(r) = 15.154 \times I_e[\text{mA}] \times \left(E_e^{lab}[\text{eV}] \right)^{-\frac{1}{2}} \times \begin{cases} \left(\frac{r}{a} \right)^2 + 2 \ln \left(\frac{a}{R} \right) - 1 & \text{for } 0 \leq r \leq a \\ 2 \ln \left(\frac{r}{R} \right) & \text{for } a \leq r \leq R \end{cases} \quad (\text{A.17})$$

For typical parameters of $a = 0.5$ cm and $R = 5$ cm, we get:

$$V(0) = -84.938 \times I_e[\text{mA}] \times \left(E_e^{lab}[\text{eV}] \right)^{-\frac{1}{2}} \quad (\text{A.18})$$

$$(\text{A.19})$$

$$V(a) = -69.785 \times I_e[\text{mA}] \times \left(E_e^{lab}[\text{eV}] \right)^{-\frac{1}{2}}. \quad (\text{A.20})$$

The space charge potential gives rise to a dependence of electron energy on position relative to the beam axis. Therefore, apart from decelerating the electrons, the space charge will further contribute to the energy spread of the electron beam.

Appendix B

Toroid correction

This appendix derives Eq. 2.23 regarding the relative energies encountered within the toroid regions of the ASTRID electron cooler.

B.1 The relative energy in the toroid regions

Relative velocities in the toroid region:

$$\begin{aligned}v_{rel}^{\perp} &= v_e \sin \theta \\v_{rel}^{\parallel} &= v_i - v_e \cos \theta\end{aligned}\tag{B.1}$$

From this the relative energy in the toroid region can be found:

$$\begin{aligned}E_{rel}^{tor}(z) &= E_{rel}^{\perp} + E_{rel}^{\parallel} \\&= \frac{1}{2}m_e(v_{rel}^{\perp})^2 + \frac{1}{2}m_e(v_{rel}^{\parallel})^2 \\&= \frac{1}{2}m_e \left[v_e^2 \sin^2 \theta + v_i^2 + v_e^2 \cos^2 \theta - 2v_i v_e \cos \theta \right] \\&= \frac{1}{2}m_e v_e^2 + \frac{1}{2}m_e v_i^2 - m_e v_i v_e \cos \theta \\&= E_e^{lab} + \frac{m_e}{M_{ion}} E_{ion} - 2 \sqrt{\frac{m_e}{M_{ion}} E_{ion} E_e^{lab}} \cos \theta\end{aligned}\tag{B.2}$$

From trigonometry one finds the following relation concerning θ :

$$\sin \theta = \frac{z}{R_T}\tag{B.3}$$

where R_T is the radius of curvature of the toroid magnets. This means that:

$$\cos \theta = \cos \left(\arcsin \left(\frac{z}{R_T} \right) \right) = \frac{\sqrt{R_T^2 - z^2}}{R_T}\tag{B.4}$$

One can now use the following relation:

$$\begin{aligned}
E_{rel} &= \frac{1}{2}m_e(v_i - v_e)^2 \\
&= \left[\sqrt{\frac{m_e}{M_{ion}}E_{ion}} - \sqrt{E_e^{lab}} \right]^2 \\
&= \frac{m_e}{M_{ion}}E_{ion} + E_e^{lab} - 2\sqrt{\frac{m_e}{M_{ion}}E_{ion}E_e^{lab}}
\end{aligned} \tag{B.5}$$

to modify equation B.2:

$$\begin{aligned}
E_{rel}^{tor}(z) &= E_e^{lab} + \frac{m_e}{M_{ion}}E_{ion} - 2\sqrt{\frac{m_e}{M_{ion}}E_{ion}E_e^{lab}} \cos \theta \\
&= E_{rel} + 2\sqrt{\frac{m_e}{M_{ion}}E_{ion}E_e^{lab}} (1 - \cos \theta) \\
&= E_{rel} + 2\sqrt{E_{cool}E_e^{lab}} \left(1 - \frac{\sqrt{R_T^2 - z^2}}{R_T} \right)
\end{aligned} \tag{B.6}$$

Appendix C

Rate coefficients

This appendix derives Eq. 2.25 regarding the absolute rate coefficient extracted from the merged beams setup at ASTRID, and Eq. 4.6 regarding the thermal rate coefficient extracted from electron-cation collision cross-sections.

C.1 The absolute rate coefficient

This section derives the absolute rate coefficient from electron scattering reactions in terms of quantities measurable at the ASTRID storage ring. The expression is found in the thesis as Eq. 2.25.

Imagine initially that only one ion is present in the interaction region. The reaction cross section, σ , can then be measured as:

$$\sigma = \frac{\text{rate of signal events } [s^{-1}]}{\text{incident electron flux } [cm^{-2}s^{-1}]}, \quad (C.1)$$

where the electron flux is to be calculated in the rest frame of the ions. When more than one ion is present, as is the case of an ion beam, the cross section will have to be normalized to the number of ions in the interaction region:

$$\sigma = \frac{\text{rate of signal events}}{\text{incident electron flux}} \times \frac{1}{\text{ions in the interaction region}} [cm^2]. \quad (C.2)$$

The number of ions in the interaction region can now be related to the rate of ions passing through the interaction region, if the velocity of the ions, v_i , and the length of the interaction region, L , are known:

$$N_{ions} = (\text{ions in the interaction region}) \times \frac{v_i}{L} [s^{-1}]. \quad (C.3)$$

The incident electron flux can be calculated from the density, n_e , and velocity, v_e , of the electrons:

$$(\text{incident electron flux}) = n_e v_e [cm^{-2}s^{-1}], \quad (C.4)$$

while the rate of signal events are found from the signal minus background, $N_s - N_b f$, normalized to the detector efficiency, ϵ :

$$(\text{rate of signal events}) = \frac{N_s - N_b f}{\epsilon} [s^{-1}] \quad (C.5)$$

where f is the ion beam lifetime correction factor. By combining Eqs. C.3, C.4, and C.5 with Eq. C.2, we get the final expression for the absolute rate coefficient (as given in Eq. 2.25):

$$\langle v\sigma \rangle = \frac{N_s - N_b f}{N_{ion}} \frac{v_i}{n_e L \epsilon}. \quad (\text{C.6})$$

C.2 The thermal rate coefficient

This section derived an expression for the thermal rate coefficient $\alpha(T)$ corresponding to a temperature T and a cross-section $\sigma(E)$ (Eq. 4.6).

For a given temperature, the thermal rate coefficient is defined as the rate coefficient $\langle v_e \sigma \rangle$ obtained when the velocity distribution of the electrons is described by a thermal (Maxwellian) function:

$$f(\mathbf{v}_e, T) d\mathbf{v}_e = \left(\frac{m_e}{2\pi kT} \right)^{3/2} e^{-m_e \mathbf{v}_e^2 / 2kT} d\mathbf{v}_e. \quad (\text{C.7})$$

Changing variables from electron velocity \mathbf{v}_e to electron speed v_e :

$$f(v_e, T) dv_e = 4\pi \left(\frac{m_e}{2\pi kT} \right)^{3/2} v_e^2 e^{-m_e v_e^2 / 2kT} dv_e, \quad (\text{C.8})$$

and then to electron energy $E = \frac{1}{2} m_e v_e^2$, the Maxwellian energy distribution at the temperature T is found:

$$f(E, T) dE = \frac{2\pi}{(\pi kT)^{3/2}} \sqrt{E} e^{-E/kT} dE. \quad (\text{C.9})$$

The thermal rate coefficient can be found from the cross-section $\sigma(E)$ through the equation:

$$\alpha(T) = \langle v_e \sigma \rangle = \int_0^\infty v_e \sigma(E) f(E, T) dE. \quad (\text{C.10})$$

Inserting the electron energy distribution yields the thermal rate coefficient as described by Eq. 4.6:

$$\alpha(T) = \frac{8\pi m_e}{(2\pi m_e kT)^{3/2}} \int_0^\infty \sigma(E) e^{-E/kT} E dE. \quad (\text{C.11})$$

Appendix D

List of abbreviations

This appendix contains a list of the abbreviations that can be found in the thesis.

ACAP - Aarhus Center for Atomic Physics

AMP - Adenosine 5'-MonoPhosphate

ANIS - Aarhus Negative Ion Source

ASTRID - Aarhus STorage RIng Denmark

BCM - Beam Charge Monitor

CCIS - Cold Cathode Ion Source

CRM - Charge Residue Model

CRYRING - CRYogenic ion source RING

DE - Dissociative Excitation

DESIREE - Double Electrostatic Storage Ion Ring ExpEriment

DR - Dissociative Recombination

EA - Electron Affinity

EBIS - Electron Beam Ion Source

ELISA - ELectrostatic Ion Storage ring Aarhus

ESI - ElectroSpray Ionization

FALP - Flowing Afterglow - Langmuir Probe

FWHM - Full Width at Half Maximum

MCP - Multi Channel Plate

MSP - Multi Sphere Plate

RCB - Repulsive Coulomb Barrier

RF - Radio Frequency

SSD - Solid-State Detector

VUV - Vacuum Ultra-Violet

List of Figures

1	Outline of thesis	v
1.1	The road towards complexity.	2
2.1	The ASTRID storage ring	7
2.2	ASTRID electron target	8
2.3	Electron current as a function of acceleration voltage	9
2.4	Adiabatically expanding field	13
2.5	Electron densities at ASTRID	14
2.6	Electron energy distribution at ASTRID	16
2.7	Toroid region of ASTRID electron cooler	16
2.8	Toroid contribution to cross-sections	18
2.9	SSD spectrum from O_3^- experiment	19
2.10	ASTRID timing	20
2.11	The ELISA storage ring	23
2.12	Calculated longitudinal energy distribution in ETRAP	26
2.13	Sputter source	27
2.14	Cold cathode ion source	29
2.15	Electrospray ion source (ESI)	32
2.16	Comparison of two SSD spectra.	34
2.17	Schematic diagram of the Aarhus tandem accelerator.	35
2.18	Tandem analysis of ion beam	36
3.1	Dianion potential	42
3.2	S^- detachment cross-section	44
3.3	Cl^- detachment cross-section	44
3.4	Absolute cross-section measurement for CN^-	46
3.5	CN^- and BO^- detachment cross-section	46
3.6	O_3^- cross-sections	48
3.7	O_3^- branching ratios	49
3.8	NO_2^- detachment cross-section	50
3.9	Total NO_3^- cross-section	51
3.10	SO_2^- detachment cross-section	53
3.11	Non-resonant model cross-sections for NO_3^- , SO_2^- and O_3^-	55
3.12	Anion detachment thresholds	55
4.1	Direct and indirect DR mechanisms	61
4.2	Tunneling DR mechanism	63
4.3	Measured rate coefficients for CO_2^+	65
4.4	Measured rate coefficients for CO_2^{2+}	65

4.5	Model cross-section comparison to CO_2^+ data	66
4.6	Branching ratios for CO_2^{2+}	68
4.7	Absolute rate coefficients for N_2^{2+}	69
4.8	Absolute rate coefficients for CO^{2+}	71
5.1	Electron target for ELISA	77
5.2	Picture of ETRAP electrodes	78
5.3	Picture of ETRAP installed in ELISA	78
5.4	Electron-induced signal from ETRAP	79
5.5	NO_2^- cross-section measured at ELISA	80
5.6	Experimental determination of K_{eff}	81
5.7	AMP^- cross-section measured at ELISA	82
A.1	Diagram of beam charge distribution	91
A.2	Gauss surface for space charge derivation	92

List of Tables

2.1	Ions produced by cold cathode ion source	30
2.2	Comparison of ion sources	33
3.1	GAUSSIAN-98 anion calculations	43
3.2	NO ₃ ⁻ branching ratios	52
4.1	Thermal rate coefficients for CO ₂ ⁺	67
4.2	CO ₂ ⁺ branching ratios	68
4.3	Comparison of rate coefficients measured at storage rings	72

Bibliography

- [1] C. Kenty, “*The recombination of argon ions and electrons*”, Phys. Rev. **32**, 624 (1928).
- [2] M. A. Biondi and S. C. Brown, “*Measurement of electron-ion recombination*”, Phys. Rev. **76**, 1697 (1949).
- [3] J. N. Bardsley and M. A. Biondi, “*Dissociative recombination*”, Adv. At. Mol. Phys. **6**, 1 (1970).
- [4] A. Canosa, J. C. Gomet, B. R. Rowe, J. B. A. Mitchell, and J. L. Queffelec, “*Further measurements of the H ($\nu=0,1,2$) dissociative recombination rate coefficient*”, J. Chem. Phys. **97**, 1028 (1992).
- [5] B. Benderson, H. Malamud, and J. Hammer, “*Elastic scattering of electrons by atomic hydrogen*”, Bull. Am. Phys. Soc. Ser. II **2**, 172 (1957).
- [6] R. L. F. Boyd and G. W. Green, “*Electron ionization cross sections using chopped beams*”, Proc. Phys. Soc. **71**, 351 (1958).
- [7] B. Davis and A. H. Barnes, “*The capture of electrons by swiftly moving alpha-particles*”, Phys. Rev. **34**, 152 (1929).
- [8] S. M. Trujillo, R. H. Neynaber, and E. W. Rothe, “*Merging beams, a different approach to collision cross section measurements*”, Rev. Sci. Instrum. **37**, 1655 (1966).
- [9] L. P. Theard, “*Studies of dissociative electron-ion neutralization with superimposed beams*”, in *Sixth international conference on the physics of electronic and atomic collisions, abstracts of papers*, page 1042, MIT Press, 1969.
- [10] D. Auerbach, R. Cacak, R. Caudano, T. D. Gaily, C. J. Keyser, J. W. McGowan, J. B. A. Mitchell, and S. F. J. Wilk, “*Merged electron-ion beam experiments. I. Method and measurements of $(e-H_2^+)$ and $(e-H_3^+)$ dissociative-recombination cross sections*”, J. Phys. B: At. Mol. Opt. Phys. **10**, 3797 (1977).
- [11] R. A. Phaneuf, C. C. Havener, G. H. Dunn, and A. Müller, “*Merged-beams experiments in atomic and molecular physics*”, Rep. Prog. Phys. **62**, 1143 (1999).
- [12] H. Poth, “*Electron cooling: Theory, experiment, application*”, Phys. Rep. **196**, 135 (1990).
- [13] T. W. Hänsch and A. L. Schawlow, “*Cooling of gases by laser radiation*”, Opt. Comm. **13**, 68 (1975).

- [14] D. Zajfman, J. B. A. Mitchell, D. Schwalm, and B. R. Rowe, editors, *Dissociative recombination: Theory, experiment and applications III*, World Scientific, Singapore, 1996.
- [15] M. Larsson, “Atomic and molecular physics with ion storage rings”, Rep. Prog. Phys. **58**, 1267 (1995).
- [16] J. A. Sauer, M. D. Barrett, and M. S. Chapman, “Storage ring for neutral atoms”, Phys. Rev. Lett. **87**, 270401 (2001).
- [17] F. M. H. Cromptvoets, H. L. Bethlem, R. T. Jonkma, and G. Meijer, “A prototype storage ring for neutral molecules”, Nature **411**, 174 (2001).
- [18] S. P. Møller, “ASTRID - A storage ring for ions and electrons”, in *Proceedings of the 1991 IEEE particle accelerator conference*, page 2811, San Francisco, 1991.
- [19] S. P. Møller, “ASTRID - A small multi-purpose storage ring”, in *Proceedings of the 3rd European particle accelerator conference*, Berlin, 1992.
- [20] S. P. Møller, “Recent developments in small storage rings”, in *Proceedings from the 4th European particle accelerator conference*, page 173, London, 1994.
- [21] J. S. Nielsen and S. P. Møller, “New developments at the ASTRID storage ring”, in *Proceedings from 6th European particle accelerator conference*, Stockholm, 1998.
- [22] Private communication, Niels Hertel, Department of Physics and Astronomy, University of Aarhus, Denmark.
- [23] J. R. Pierce, “Rectilinear electron flow in beams”, J. App. Phys. **11**, 548 (1940).
- [24] J. R. Pierce, “The theory and design of electron beams”, Van Nostrand, New York, 2nd edition, 1954.
- [25] L. H. Andersen, J. Bolko, and P. Kvistgaard, “State-selective dielectronic-recombination measurements for He- and Li-like carbon and oxygen ions”, Phys. Rev. A **41**, 1293 (1990).
- [26] A. V. Aleksandrov, R. Calabrese, N. S. Dikanskii, V. Guidi, N. C. Kot, V. I. Kudelainen, V. A. Lebedev, P. V. Logachov, and L. Tecchio, “Electron cooling: Theory, experiment, application”, Europhys. Lett. **18**, 151 (1992).
- [27] M. Sedlaček, H. Poth, D. Krämer, L. Tecchio, and H. O. Meyer, “Electron cooling in storage rings”, Phys. Script. T **22**, 204 (1988).
- [28] H. Danared, “Fast electron cooling with a magnetically expanded electron beam”, Nucl. Instrum. Meth. A **335**, 397 (1993).
- [29] H. Danared, G. Andler, L. Bagge, C. J. Herrlander, J. Hilke, J. Jeansson, A. Källberg, A. Nilsson, A. Paál, K.-G. Rensfelt, U. Rosengård, J. Starker, and M. af Ugglas, “Electron cooling with an ultracold electron beam”, Phys. Rev. Lett. **72**, 3775 (1994).

- [30] V. I. Kudelainen, V. A. Lebedev, I. N. Meshkov, V. V. Parkhomochuk, and B. N. Sukhina, “*Temperature relaxation in a magnetized electron beam*”, *Sov. Phys. JETP* **56**, 1191 (1982).
- [31] A. V. Aleksandrov, N. S. Dikansky, N. C. Kot, V. I. Kudelainen, V. A. Lebedev, and P. V. Logachov, “*Temperature relaxation and adiabatic acceleration at magnetized electron flux*”, in *Proceedings of the workshop on electron cooling and new cooling techniques*, page 279, Singapore, 1991, World Scientific.
- [32] H. Danared, “*Simulation of relaxation processes in electron beams at high magnetic fields*”, *Hyperfine Interactions* **115**, 61 (1998).
- [33] O. Habs, J. Kramp, P. Krause, K. Matl, R. Neumann, and D. Schwalm, “*Ultracold ordered electron beam*”, *Phys. Script. T* **22**, 269 (1988).
- [34] A. Lampert, A. Wolf, D. Habs, J. Kenntner, G. Kilgus, D. Schwalm, M. S. Pindzola, and N. R. Badnell, “*High-resolution measurement of the dielectronic recombination of fluorinelike selenium ions*”, *Phys. Rev. A* **53**, 1413 (1996).
- [35] S. P. Møller, “*ELISA, an electrostatic storage ring for atomic physics*”, *Nucl. Instrum. Meth. A* **394**, 281 (1997).
- [36] S. P. Møller and U. V. Pedersen, “*Small electrostatic storage rings; also for highly charged ions*”, *Phys. Script. T* **92**, 105 (2001).
- [37] U. V. Pedersen, M. Hyde, S. P. Møller, and T. Andersen, “*Lifetime measurement of He^- utilizing an electrostatic ion storage ring*”, *Phys. Rev. A* **64**, 012503 (2001).
- [38] M. J. Jensen, U. V. Pedersen, and L. H. Andersen, “*Stability of the ground state vinylidene anion H_2CC^-* ”, *Phys. Rev. Lett.* **84**, 1128 (2000).
- [39] T. Tanabe, K. Chida, K. Noda, and I. Watanabe, “*An electrostatic storage ring for atomic and molecular science*”, *Nucl. Instrum. Meth. A* **482**, 595 (2002).
- [40] D. Zajfman, O. Heber, L. Vejby Christensen, I. Ben Itzhak, M. Rappaport, R. Fishman, and M. Dahan, “*Electrostatic bottle for long-time storage of fast ion beams*”, *Phys. Rev. A* **55**, R1577 (1997).
- [41] D. Strasser, O. Heber, S. Goldberg, and D. Zajfman, “*Self-bunching induced by negative effective mass instability in an electrostatic ion beam trap*”, *J. Phys. B: At. Mol. Opt. Phys.* **36**, 953 (2003).
- [42] M. H. Holzscheiter, “*A brief history in time of ion traps and their achievements in science*”, *Phys. Script. T* **59**, 69 (1995).
- [43] R. Schuch, “*Storage rings for low-energy experiments*”, *Phys. Script. T* **59**, 77 (1995).
- [44] R. Middleton and C. T. Adams, “*A close to universal negative ion source*”, *Nucl. Instrum. Meth.* **118**, 329 (1974).
- [45] H. H. Andersen and P. Tykesson, “*A PIG sputter source for negative ions*”, *IEEE Trans. Nucl. Sci.* **NS-22**, 1632 (1975).

- [46] P. Tykesson, H. H. Andersen, and J. Heinemeier, “*Further investigations of ANIS (the aarhus negative-ion source)*”, IEEE Trans. Nucl. Sci. **NS-23**, 1104 (1976).
- [47] J. Heinemeier and H. H. Andersen, “*Production of C^- directly from CO_2 using the ANIS sputter source*”, Radiocarbon **25**, 761 (1983).
- [48] V. E. Krohn, “*Emission of negative ions from metal surfaces bombarded by positive cesium ions*”, J. Appl. Phys. **33**, 3523 (1962).
- [49] R. Middleton, “*A review of ion sources for accelerator mass spectrometry*”, Nucl. Instrum. Meth. B **5**, 193 (1984).
- [50] K. O. Nielsen, “*The development of magnetic ion sources for an electromagnetic isotope separator*”, Nucl. Instrum. Meth. **1**, 289 (1957).
- [51] O. Almé and K. O. Nielsen, “*Systematic investigation of a magnetic ion source for an electromagnetic isotope separator*”, Nucl. Instrum. Meth. **1**, 302 (1957).
- [52] J. Zeleny, “*Instability of electrified liquid surfaces*”, Phys. Rev. **10**, 1 (1917).
- [53] M. Dole, L. L. Mach, R. L. Hines, R. C. Mobley, L. D. Ferguson, and M. B. Alice, “*Molecular beams of macroions*”, J. Chem. Phys. **49**, 2240 (1968).
- [54] J. B. Fenn, M. Mann, C. K. Meng, S. F. Wong, and C. M. Whitehous, “*Electrospray ionization for mass spectrometry of large biomolecules*”, Science **246**, 64 (1989).
- [55] M. Yamashita and J. B. Fenn, “*Electrospray ion source. Another variation on the free-jet theme*”, J. Phys. Chem. **88**, 4451 (1984).
- [56] J. U. Andersen, P. Hvelplund, S. B. Nielsen, S. Tomita, H. Wahlgreen, S. P. Møller, U. V. Pedersen, J. S. Forster, and T. J. D. Jørgensen, “*The combination of an electrospray ion source and an electrostatic storage ring for lifetime and spectroscopy experiments on biomolecules*”, Rev. Sci. Instrum. **73**, 1284 (2002).
- [57] P. Kebarle and M. Peschke, “*On the mechanisms by which the charged droplets produced by electrospray lead to gas phase ions*”, Anal. Chim. Acta **406**, 11 (2000).
- [58] B. M. Smirnov, “*Negative ions*”, McGraw-Hill Inc., 1982.
- [59] J. Kalcher and A. X. Sax, “*Gas phase stabilities of small anions: theory and experiment in cooperation*”, Chem. Rev **94**, 2291 (1994).
- [60] D. E. Nelson, R. G. Korteling, and W. R. Stott, “*Carbon-14: Direct detection at natural concentrations*”, Science **198**, 507 (1977).
- [61] C. L. Bennett, R. P. Beukens, M. R. Clover, H. E. Gove, R. B. Liebert, A. E. Litherland, K. H. Purser, and W. E. Sondheim, “*Radiocarbon dating using electrostatic accelerators: Negative ions provide the key*”, Science **198**, 508 (1977).
- [62] R. E. M. Hedges and J. A. J. Gowlett, “*Accelerating carbon dating*”, Nature **308**, 403 (1984).
- [63] J. J. Thomson, “*Rays of positive electricity and their application to chemical analysis*”, Longmans, Green and Co. Ltd., London, 1st edition, 1913.

- [64] F. W. Aston, *“Isotopes”*, Edward Arnold & Co., 1923.
- [65] L. M. Branscomb and W. L. Fite, *“Photodetachment of the hydrogen negative ion (abstract)”*, Phys. Rev. **93**, 651 (1954).
- [66] L. M. Branscomb and S. J. Smith, *“Experimental cross section for photodetachment of electrons from H^- and D^- ”*, Phys. Rev. **98**, 1028 (1955).
- [67] L. M. Branscomb, D. S. Burch, S. J. Smith, and S. Geltman, *“Photodetachment cross section and the electron affinity of atomic oxygen”*, Phys. Rev. **11**, 504 (1958).
- [68] H. Hotop and W. C. Lineberger, *“Binding energies in atomic negative ions”*, J. Phys. Chem. Ref. Data **14**, 731 (1985).
- [69] G. Tisone and L. M. Branscomb, *“Detachment of electrons from H^- by electron impact”*, Phys. Rev. Lett. **17**, 236 (1966).
- [70] D. F. Dance, M. F. A. Harrison, and R. D. Rundel, *“A measurement of the cross-section for detachment of electrons from H^- by electron impact”*, Proc. R. Soc. London Ser. A **299**, 525 (1967).
- [71] G. Tisone and L. M. Branscomb, *“Detachment of electrons from H^- and O^- negative ions by electron impact”*, Phys. Rev. **170**, 169 (1968).
- [72] B. Peart, D. S. Walton, and K. T. Dolder, *“Electron detachment from H^- ions by electron impact”*, J. Phys. B: At. Mol. Opt. Phys. **3**, 1346 (1970).
- [73] B. Peart, R. Forrest, and K. T. Dolder, *“Measurements of cross sections for detachment of electrons from C^- and O^- ions by electron impact”*, J. Phys. B: At. Mol. Opt. Phys. **12**, 847 (1979).
- [74] B. Peart, R. Forrest, and K. T. Dolder, *“Measurements of detachment from F^- by electron impact tests of classical scaling for electron impact detachment cross sections”*, J. Phys. B: At. Mol. Opt. Phys. **12**, L115 (1979).
- [75] L. H. Andersen, T. Andersen, H. K. Haugen, N. Hertel, P. Hvelplund, S. P. Möller, and W. W. Smith, *“Storage of negative keV ions in a heavy-ion storage ring”*, Phys. Lett. A **162**, 336 (1992).
- [76] L. H. Andersen, D. Mathur, H. T. Schmidt, and L. Vejby-Christensen, *“Electron-impact detachment of D^- : Near-threshold behaviour and the nonexistence of D^{2-} resonances”*, Phys. Rev. Lett. **74**, 892 (1995).
- [77] T. Tanabe, I. Katayama, H. Kamegaya, K. Chida, T. Watanabe, Y. Arakaki, M. Yoshizawa, Y. Haruyama, M. Saito, T. Honma, K. Hosono, K. Hatanaka, F. J. Currell, and K. Noda, *“Search for H^{2-} resonances in the detachment of H^- by electron impact with a high-resolution cooler ring”*, Phys. Rev. A **54**, 4069 (1996).
- [78] K. Andersson, D. Hanstorp, A. Neau, S. Rosén, H. Schmidt, R. Thomas, M. Larsson, J. Semaniak, F. Österdahl, H. Danared, and A. Le Padellec, *“Electron impact single detachment on the F^- ions using the heavy ion storage ring CRYRING: Cross-section determination”*, Eur. Phys. J. D **13**, 323 (2001).

- [79] L. Vejby-Christensen, D. Kella, D. Mathur, H. B. Pedersen, H. T. Schmidt, and L. H. Andersen, “*Electron-impact detachment from negative ions*”, Phys. Rev. A **53**, 2371 (1996).
- [80] H. B. Pedersen, N. Djurić, M. J. Jensen, D. Kella, C. P. Safvan, H. T. Schmidt, L. Vejby-Christensen, and L. H. Andersen, “*Electron collisions with diatomic anions*”, Phys. Rev. A **60**, 2882 (1999).
- [81] L. H. Andersen, R. Bilodeau, M. J. Jensen, S. B. Nielsen, C. P. Safvan, and K. Seiersen, “*Coulomb and centrifugal barrier bound dianion resonances of NO₂*”, J. Chem. Phys. **114**, 147 (2001).
- [82] A. Le Padellec, F. Rabilloud, D. Pegg, A. Neau, F. Hellberg, R. Thomas, H. T. Schmidt, M. Larsson, H. Danared, A. Källberg, K. Andersson, and D. Hanstorp, “*Electron-impact detachment and dissociation of C₄⁻ ions*”, J. Chem. Phys. **115**, 10671 (2001).
- [83] R. Middleton and J. Klein, “*Experimental verification of the existence of the gas-phase dianions BeF₄²⁻ and MgF₄²⁻*”, Phys. Rev. A **60**, 3515 (1999).
- [84] K. H. Chang, R. D. McKeown, R. G. Milner, and J. Labrenz, “*Search for long-lived doubly charged negative atomic ions*”, Phys. Rev. A **35**, 3949 (1987).
- [85] R. C. Dougherty, “*Negative-ion mass spectrum of benzol[cd],-pyrene-6-one. Evidence for a doubly charged negative ion in the gas phase*”, J. Chem. Phys. **50**, 1896 (1969).
- [86] S. N. Schauer, P. Williams, and R. N. Compton, “*Production of small doubly charged negative carbon cluster ions by sputtering*”, Phys. Rev. Lett. **65**, 625 (1990).
- [87] M. K. Scheller, R. N. Compton, and L. S. Cederbaum, “*Gas-phase multiply charged anions*”, Science **270**, 1160 (1995).
- [88] M. K. Scheller and L. S. Cederbaum, “*Existence of doubly-negative charged ions and relation to solids*”, J. Phys. B: At. Mol. Opt. Phys. **25**, 2257 (1992).
- [89] M. K. Scheller and L. S. Cederbaum, “*Stability of MX₃⁻² ions in the gas phase and when do ionic molecules have large ionization potentials*”, J. Chem. Phys. **99**, 441 (1993).
- [90] H.-G. Weikert and L. S. Cederbaum, “*Free doubly negative tetrahalides*”, J. Chem. Phys. **99**, 8877 (1993).
- [91] H. Gnaser, “*Molecular anions sputtered from fluorides*”, Nucl. Instrum. Meth. B **197**, 49 (2002).
- [92] A. Dreuw and L. S. Cederbaum, “*Multiply charged anions in the gas phase*”, Chem. Rev. **102**, 181 (2002).
- [93] F. Robicieux, “*Electron impact detachment of weakly bound negative ions*”, Phys. Rev. Lett. **82**, 707 (1999).

- [94] F. Robicheaux, “*Electron-impact detachment of weakly bound negative ions: threshold and scaling laws*”, *Phys. Rev. A* **60**, 1206 (1999).
- [95] J. M. Rost, “*Threshold detachment of negative ions by electron impact*”, *Phys. Rev. Lett.* **82**, 1652 (1999).
- [96] J. T. Lin, T. F. Jiang, and C. D. Lin, “*Coulomb trajectory effects on electron-impact detachment of negative ions and on mutual neutralization cross sections*”, *J. Phys. B: At. Mol. Opt. Phys.* **29**, 6175 (1996).
- [97] M. S. Pindzola and F. J. Robicheaux, “*Time-dependent close-coupling calculations for the electron-impact ionization of helium*”, *Phys. Rev. A* **61**, 052707 (2000).
- [98] M. S. Pindzola and F. J. Robicheaux, “*Ejected-energy differential cross sections for the electron-impact detachment of H^-* ”, *J. Phys. B: At. Mol. Opt. Phys.* **33**, L427 (2000).
- [99] A. Le Padellec, G. F. Collins, H. Danared, A. Källberg, F. Hellberg, A. Neau, K. Fritioff, D. Hanstorp, and M. Larsson, “*Relative cross sections for the electron impact single detachment on Li^-* ”, *J. Phys. B: At. Mol. Opt. Phys.* **35**, 3669 (2002).
- [100] V. N. Ostovsky and K. Taulbjerg, “*Quantum tunnelling and classical above-barrier transitions in electron detachment from negative ions by negatively charged projectiles*”, *J. Phys. B: At. Mol. Opt. Phys.* **29**, 2573 (1996).
- [101] G. J. Schulz, “*Resonances in electron impact on atoms*”, *Rev. Mod. Phys.* **45**, 378 (1973).
- [102] A. Dreuw and L. S. Cederbaum, “*Nature of the repulsive Coulomb barrier in multiply charged negative ions*”, *Phys. Rev. A* **63**, 049904 (2001).
- [103] L. H. Andersen, P. Hvelplund, D. Kella, P. H. Mokler, H. B. Pedersen, H. T. Schmidt, and L. Vejby-Christensen, “*Resonance structure in the electron-impact detachment cross section of C_2^- caused by the formation of C_2^{2-}* ”, *J. Phys. B: At. Mol. Opt. Phys.* **29**, L643 (1996).
- [104] H. B. Pedersen, N. Djurić, M. J. Jensen, D. Kella, C. P. Safvan, L. Vejby-Christensen, and L. H. Andersen, “*Doubly charged negative ions of B_2 and C_2* ”, *Phys. Rev. Lett.* **81**, 5302 (1998).
- [105] A. Le Padellec, K. Andersson, D. Hanstorp, F. Hellberg, M. Larsson, A. Neau, S. Rosén, H. T. Schmidt, R. Thomas, J. Semaniak, D. J. Pegg, F. Østerdahl, H. Danared, and A. Källberg, “*Electron scattering on CN^-* ”, *Phys. Script.* **64**, 467 (2001).
- [106] L. H. Andersen, J. Bak, S. Boyé, M. Clausen, M. Hovgaard, M. J. Jensen, A. Lapierre, and K. Seiersen, “*Resonant and nonresonant electron impact detachment of CN^- and BO^-* ”, *J. Chem. Phys.* **115**, 3566 (2001).
- [107] K. Andersson, D. Hanstorp, A. Neau, S. Rosén, H. Schmidt, J. Semaniak, R. Thomas, M. Larsson, F. Hellberg, A. Le Padellec, and D. J. Pegg, “*Electron scattering on negative ions in a storage ring*”, in *Photonic, Electronic and Atomic Collisions, XXII International Conference*, Santa Fe, New Mexico, 2001.

- [108] GAUSSIAN 98, Revision A.7, M.J. Frisch *et al.*, Gaussian, Inc., Pittsburg, PA, 1998.
- [109] W. C. Lineberger and B. W. Woodward, “*High resolution photodetachment of S^- near threshold*”, Phys. Rev. Lett. **25**, 424 (1970).
- [110] C. Blondel, “*Recent experimental achievements with negative ions*”, Phys. Script. T **58**, 31 (1995).
- [111] U. Berzinsh, M. Gustafsson, D. Hanstorp, A. Klinkmüller, U. Ljungblad, and A.-M. Mårtensson-Pendrill, “*Isotope shift in the electron affinity of chlorine*”, Phys. Rev. A **51**, 231 (1995).
- [112] K. Fritioff, J. Sandström, D. Hanstorp, A. Ehlerding, M. Larsson, G. F. Collins, D. J. Pegg, H. Danared, A. Källberg, and A. Le Padellec, “*Electron-impact detachment from Cl^-* ”, Phys. Rev. A **68**, 012712 (2003).
- [113] A. I. Boldyrev, M. Gutowski, and J. Simons, “*Small multiply charged anions as building blocks in chemistry*”, Acc. Chem. Res. **29**, 497 (1996).
- [114] T. Sommerfeld, “*Resonance states of atomic di-anions*”, Phys. Rev. Lett. **85**, 956 (2000).
- [115] F. Abildskov and S. P. Møller, “*Bunched-beam measurement of very small currents at ASTRID*”, in *Beam Instrumentation: Proceedings of the Seventh Workshop*, edited by A. H. Lumpkin and C. E. Eyberger, page 536, American Institute of Physics, New York, 1997.
- [116] D. W. Arnold, C. S. Xu, E. H. Kim, and D. M. Neumark, “*Study of low-lying electronic states of ozone by anion photoelectron spectroscopy of O_3^-* ”, J. Chem. Phys. **101**, 912 (1994).
- [117] P. C. Cosby, J. T. Moseley, J. R. Peterson, and J. H. Ling, “*Photodissociation spectroscopy of O_3^-* ”, J. Chem. Phys. **69**, 2771 (1978).
- [118] M. J. Jensen, R. C. Bilodeau, C. P. Safvan, K. Seiersen, and L. H. Andersen, “*Dissociative recombination of H_3O^+ , HD_2O^+ , and D_3O^+* ”, Astrophys. J. **543**, 764 (2000).
- [119] H. S. W. Massey, “*Negative ions*”, Cambridge University Press, 1976.
- [120] A. Weaver, D. W. Arnold, S. E. Bradforth, and D. M. Neumark, “*Examination of the $^2A'_2$ and $^2E''$ states of NO_3 by ultraviolet photoelectron spectroscopy of NO_3^-* ”, J. Chem. Phys. **94**, 1740 (1991).
- [121] M. R. Nimlos and G. B. Ellison, “*Photoelectron spectroscopy of SO_2^- , S_3^- , and S_2O^-* ”, J. Phys. Chem. **90**, 2574 (1986).
- [122] H. B. Pedersen, R. Bilodeau, M. J. Jensen, I. V. Makassiouk, C. P. Safvan, and L. H. Andersen, “*Electron collisions with the diatomic fluorine anion*”, Phys. Rev. A **63**, 032718 (2001).

- [123] S. S. Prasad and D. R. Furman, “*On the importance of doubly charged ions in the auroral ionosphere*”, J. Geophys. Res. **80**, 1360 (1975).
- [124] D. Kella, P. J. Johnson, H. B. Pedersen, L. Vejby-Christensen, and L. H. Andersen, “*The source of green light emission determined from a heavy-ion storage ring experiment*”, Science **276**, 1530 (1997).
- [125] O. Witasse, O. Dutuit, J. Lilensten, R. Thissen, J. Zabka, C. Alcaraz, P.-L. Blelly, S. W. Bougher, S. Engel, L. H. Andersen, and K. Seiersen, “*Prediction of a CO_2^+ layer in the atmosphere of Mars*”, Geophys. Res. Lett. **29**, 1263 (2002).
- [126] O. Witasse, O. Dutuit, J. Lilensten, R. Thissen, J. Zabka, C. Alcaraz, P.-L. Blelly, S. W. Bougher, S. Engel, L. H. Andersen, and K. Seiersen, “*Correction to ‘Prediction of a CO_2^+ layer in the atmosphere of Mars’*”, Geophys. Res. Lett. **30**, 1360 (2003).
- [127] E. Murad and S. Lai, “*Effect of dissociative electron-ion recombination on the propagation of critical ionization discharges*”, J. Geophys. Res. **91**, 13745 (1986).
- [128] D. Smith, “*The ion chemistry of interstellar clouds*”, Chem. Rev. **92**, 1473 (1992).
- [129] A. Sternberg and A. Dalgarno, “*Chemistry in dense photon-dominated regions*”, Astrophys. J. Sup. **99**, 565 (1995).
- [130] E. Herbst and H.-H. Lee, “*New dissociative recombination product branching fractions and their effect on calculated interstellar molecular abundances*”, Astrophys. J. **485**, 689 (1997).
- [131] R. J. Oliverson, N. Doane, F. Scherb, W. M. Harris, and J. P. Morgenthaler, “*Measurements of $[C\ I]$ emission from Comet Hale-Bopp*”, Astrophys. J. **581**, 770 (2002).
- [132] J. B. A. Mitchell, “*The dissociative recombination of molecular ions*”, Phys. Rep. **186**, 215 (1990).
- [133] M. Larsson, “*Dissociative recombination with ion storage rings*”, Annu. Rev. Phys. Chem. **48**, 151 (1997).
- [134] S. D. Price, “*Interactions of molecular doubly charged ions with atoms, molecules and photons*”, J. Chem. Soc., Faraday Trans. **93**, 2451 (1997).
- [135] S. Leach, “*The formation and destruction of doubly-charged polycyclic aromatic hydrocarbon cations in the interstellar medium*”, J. Electron Spectrosc. Relat. Phenom. **41**, 427 (1986).
- [136] E. L. O. Bakes, A. G. G. M. Tielens, and C. W. Bauschlicher, Jr., “*Theoretical modeling of infrared emission from neutral and charged polycyclic aromatic hydrocarbons. I.*”, Astrophys. J. **556**, 501 (2001).
- [137] P. F. Dittner, S. Datz, P. D. Miller, C. D. Moak, P. H. Stelson, C. Bottcher, W. B. Dress, G. D. Alton, N. Neskovic, and C. M. Fou, “*Cross sections for dielectronic recombination of B^{2+} and C^{3+} via $2s\text{-}j2p$ excitation*”, Phys. Rev. Lett. **51**, 31 (1983).
- [138] D. Mathur, “*Multiply charged molecules*”, Phys. Rep. **225**, 193 (1993).

- [139] M. Larsson, “*Structure and dynamics of doubly charged molecular ions*”, *Com. At. mol. Phys.* **29**, 39 (1993).
- [140] W. W. Campbell, “*Note on the spectrum of the aurora borealis*”, *Astrophys. J.* **2**, 162 (1895).
- [141] J. C. McLennan and J. H. McLeod, “*On the wave-length of the green auroral line in the oxygen spectrum*”, *Proc. R. Soc. London Ser. A* **115**, 515 (1927).
- [142] J. Kaplan, “*The light of the night sky*”, *Phys. Rev.* **38**, 1048 (1931).
- [143] H. S. W. Masey, “*Dissociation, recombination and attachment processes in the upper atmosphere - I*”, *Proc. R. Soc. London Ser. A* **163**, 542 (1937).
- [144] D. R. Bates, R. A. Buckingham, H. S. W. Masey, and J. J. Unwin, “*Dissociation, recombination and attachment processes in the upper atmosphere II. The rate of recombination*”, *Proc. R. Soc. London Ser. A* **170**, 322 (1939).
- [145] D. R. Bates and H. S. W. Masey, “*The basic reactions in the upper atmosphere II. The theory of recombination in the ionized layers*”, *Proc. R. Soc. Lond. Ser. A* **192**, 1 (1947).
- [146] D. R. Bates, “*Dissociative recombination*”, *Phys. Rev.* **78**, 492 (1950).
- [147] J. N. Bardsley, “*The theory of dissociative recombination*”, *J. Phys. B: At. Mol. Opt. Phys.* **1**, 365 (1968).
- [148] F. W. Aston, “*The mass-spectra of chemical elements*”, *Phil. Mag.* **39**, 611 (1920).
- [149] F. W. Aston, “*The mass-spectra of chemical elements (part 2)*”, *Phil. Mag.* **40**, 628 (1920).
- [150] J. J. Thomson, “*Rays of positive electricity and their application to chemical analysis*”, Longmans, Green and Co. Ltd., London, 2nd edition, 1921.
- [151] R. Conrad, “*Über das Auftreten von doppelt positiv geladenen Molekülen im Kanalstrahl*”, *Phys. Zeit.* **31**, 888 (1930).
- [152] A. L. Vaughan, “*Mass spectrograph analyses, and critical potentials for the production of ions by electron impact, in nitrogen and carbon monoxide*”, *Phys. Rev.* **38**, 1687 (1931).
- [153] E. Friedländer, H. Kallmann, W. Lasareff, and B. Rosen, “*Über den Stoß langsamer Elektronen in Gasen. III.*”, *Z. Phys.* **76**, 70 (1932).
- [154] H. D. Hagstrum and J. T. Tate, “*Ionization and dissociation of diatomic molecules by electron impact*”, *Phys. Rev.* **59**, 354 (1941).
- [155] P. K. Carroll, “*A new transition in molecular nitrogen*”, *Can. J. Phys.* **36**, 1585 (1958).
- [156] R. W. Wetmore and R. K. Boyd, “*Theoretical investigation of the dication of molecular nitrogen*”, *J. Phys. Chem.* **90**, 5540 (1986).

- [157] H. R. Koslowski, H. Lebius, V. Staemmler, R. Fink, K. Wiesemann, and B. A. Huber, “*Collisions of doubly charged nitrogen molecules with rare gas atoms*”, J. Phys. B: At. Mol. Opt. Phys. **24**, 5023 (1991).
- [158] G. Dawber, A. G. McConkey, L. Avaldi, M. A. MacDonald, G. C. King, and R. I. Hall, “*Threshold photoelectrons coincidence spectroscopy of doubly-charged ions of nitrogen, carbon monoxide, nitric oxide and oxygen*”, J. Phys. B: At. Mol. Opt. Phys. **27**, 2191 (1994).
- [159] M. Hochlaf, R. I. Hall, F. Penent, H. Kjeldsen, P. Lablanquie, M. Lavollée, and J. H. D. Eland, “*Threshold photoelectrons coincidence spectroscopy of N_2^{2+} and CO^{2+} ions*”, Chem. Phys. **207**, 159 (1996).
- [160] L. H. Andersen, J. H. Posthumus, O. Vahtras, H. Ågren, N. Elander, A. Nunez, A. Scrinzi, M. Natiello, and M. Larsson, “*Very slow spontaneous dissociation of CO^{2+} observed by means of a heavy ion storage ring*”, Phys. Rev. Lett. **71**, 1812 (1993).
- [161] D. Mathur, L. H. Andersen, P. Hvelplund, D. Kella, and C. P. Safvan, “*Long-lived doubly charged diatomic and triatomic molecular ions*”, J. Phys. B: At. Mol. Opt. Phys. **28**, 3415 (1995).
- [162] J. S. Wright, D. J. Carpenter, A. B. Alekseyev, H.-P. Liebermann, R. Lingott, and R. J. Buenker, “*Thermodynamically stable diatomic dications: potential curves and radiative lifetimes for $CaCl^{2+}$ including relativistic effects*”, Chem. Phys. Lett. **266**, 391 (1997).
- [163] E. P. Wigner, “*On the behavior of cross sections near thresholds*”, Phys. Rev. **73**, 1002 (1948).
- [164] A. Giusti, “*A multichannel quantum defect approach to dissociative recombination*”, J. Phys. B: At. Mol. Opt. Phys. **13**, 3867 (1980).
- [165] F. B. Yousif and J. B. A. Mitchell, “*Recombination and excitation of HeH^+* ”, Phys. Rev. A **40**, 4318 (1989).
- [166] T. Tanabe, I. Katayama, N. Inoue, K. Chida, Y. Arakaki, T. Watanabe, M. Yoshizawa, S. Ohtani, and K. Noda, “*Dissociative recombination of HeH^+ at large center-of-mass energies*”, Phys. Rev. Lett. **70**, 422 (1993).
- [167] M. Larsson, “*Experimental studies of the dissociative recombination of H_3^+* ”, Phil. Trans. R. Soc. Lond. Ser. A **358**, 2433 (2000).
- [168] S. L. Guberman, “*Dissociative recombination without a curve crossing*”, Phys. Rev. A **49**, R4277 (1994).
- [169] T. Tanabe, I. Katayama, N. Inoue, K. Chida, Y. Arakaki, T. Watanabe, M. Yoshizawa, M. Saito, Y. Haruyama, K. Hosono, T. Honma, K. Noda, S. Ohtani, and H. Takagi, “*Origin of the low-energy component and isotope effect on dissociative recombinations of HeH^+ and HeD^+* ”, Phys. Rev. A **49**, R1531 (1994).
- [170] J. J. Sakurai, “*Modern quantum mechanics*”, chapter 7.2, Addison-Wesley, Massachusetts, revised edition, 1995.

- [171] S. A. Sandford, M. P. Bernstein, L. J. Allamandola, D. Goorvitch, and T. C. V. S. Teixeira, “*The abundances of solid N_2 and gaseous CO_2 in interstellar dense molecular clouds*”, *Astrophys. J.* **548**, 836 (2001).
- [172] D. Talbi and E. Herbst, “*The gas-phase destruction of interstellar carbon dioxide: Calculations on the reactions between CO_2 and H_2 and between CO_2 and H* ”, *Astron. Astrophys.* **386**, 1139 (2002).
- [173] A. S. Newton and A. F. Sciamanna, “*Metastable state of the doubly charged carbon dioxide ion*”, *J. Chem. Phys.* **40**, 718 (1964).
- [174] P. M. Mul, J. W. McGowan, P. Defrance, and J. B. A. Mitchell, “*Merged electron-ion beam experiments. V. Dissociative recombination of OH^+ , H_2O^+ , H_3O^+ and D_3O^+* ”, *J. Phys. B: At. Mol. Opt. Phys.* **16**, 3099 (1983), the cross-sections in this paper are to be divided by a factor of 2.
- [175] C. S. Weller and M. A. Biondi, “*Measurements of dissociative recombination of CO_2^+ ions with electrons*”, *Phys. Rev. Lett.* **19**, 59 (1967).
- [176] R. A. Gutcheck and E. C. Zipf, “*Excitation of the CO fourth positive system by the dissociative recombination of CO_2^+ ions*”, *J. Geophys. Res.* **78**, 5429 (1973).
- [177] M. Geoghegan, N. G. Adams, and D. Smith, “*Determination of the electron-ion dissociative recombination coefficients for several molecular ions at 300 K*”, *J. Phys. B: At. Mol. Opt. Phys.* **24**, 2589 (1991).
- [178] T. Gougousi, M. F. Golde, and R. Johnsen, “*Electron-ion recombination rate coefficient measurements in a flowing afterglow plasma*”, *Chem. Phys. Lett.* **265**, 399 (1997).
- [179] K. Seiersen, A. Al-Khalili, O. Heber, M. J. Jensen, I. B. Nielsen, H. B. Pedersen, C. P. Safvan, and L. H. Andersen, “*Dissociative recombination of the cation and dication of CO_2* ”, *Phys. Rev. A* **68**, 022708 (2003).
- [180] H. Störzer, J. Stutzki, and A. Sternberg, “ *CO^+ in the Orion Bar, M17 and S140 star-forming regions*”, *Astron. Astrophys.* **296**, L9 (1995).
- [181] S. Rosén, R. Peverall, M. Larsson, A. Le Padellec, J. Semaniak, Å. Larson, C. Strömholm, W. J. van der Zande, H. Danared, and G. H. Dunn, “*Absolute cross sections and final-state distributions for dissociative recombination and excitation of CO^+ ($\nu = 0$) using an ion storage ring*”, *Phys. Rev. A* **57**, 4462 (1998).
- [182] J. B. A. Mitchell and H. Hus, “*The dissociative recombination and excitation of CO^+* ”, *J. Phys. B: At. Mol. Opt. Phys.* **18**, 547 (1985).
- [183] S. Laubé, L. Lehfaoui, B. R. Rowe, and J. B. A. Mitchell, “*The dissociative recombination of CO^+* ”, *J. Phys. B: At. Mol. Opt. Phys.* **31**, 4181 (1998).
- [184] C. P. Safvan, M. J. Jensen, H. B. Pedersen, and L. H. Andersen, “*Dissociative recombination of the CO^{2+} dication*”, *Phys. Rev. A* **60**, R3361 (1999).
- [185] C. P. Safvan, M. J. Jensen, H. B. Pedersen, and L. H. Andersen, “*Erratum: Dissociative recombination of the CO^{2+} dication*”, *Phys. Rev. A* **62**, 019901(E) (2000).

- [186] J. R. Peterson, A. Le Padellec, H. Danared, G. H. Dunn, M. Larsson, A. Larsson, R. Peverall, C. Strömholm, S. Rosén, M. af Ugglas, and W. J. van der Zande, “*Dissociative recombination and excitation of NN_2^+ : Cross sections and product branching ratios*”, J. Chem. Phys. **108**, 1978 (1998).
- [187] B. Boudaïffa, P. Cloutier, D. Hunting, M. A. Huels, and L. Sanche, “*Resonant formation of DNA strand breaks by low-energy (3 to 20 eV) electrons*”, Science **287**, 1658 (2000).
- [188] H. Abdoul-Carime, P.-C. Dugal, and L. Sanche, “*Damage induced by 1-30 eV electrons on thymine- and bromouracil-substituted oligonucleotides*”, Rad. res. **153**, 23 (2000).
- [189] H. Abdoul-Carime, M. A. Huels, E. Illenberger, , and L. Sanche, “*Sensitizing DNA to secondary electron damage: resonant formation of oxidative radicals from 5-halouracils*”, J. Am. Chem. Soc. **123**, 5354 (2001).
- [190] T. Tanabe and K. Noda, “*Storage of bio-molecular ions in the electrostatic storage ring*”, Nucl. Instrum. Meth. A **496**, 233 (2003).
- [191] R. A. Zubarev, D. M. Horn, E. K. Fridriksson, N. L. Kelleher, N. A. Kruger, M. A. Lewis, B. K. Carpenter, and F. W. McLafferty, “*Electron capture dissociation for structural characterization of multiply charged protein cations*”, Anal. Chem. **72**, 563 (2000).
- [192] B. A. Budnik, K. F. Haselmann, and R. A. Zubarev, “*Electron detachment dissociation of peptide di-anions: an electron-hole recombination phenomenon*”, Chem. Phys. Lett. **342**, 299 (2001).
- [193] F. Kjeldsen, K. F. Haselmann, B. A. Budnik, F. Jensen, and R. A. Zubarev, “*Dissociative capture of hot (3-13 eV) electrons by polypeptide polycations: an efficient process accompanied by secondary fragmentation*”, Chem. Phys. Lett. **356**, 201 (2002).
- [194] L. H. Andersen, A. Lapierre, S. B. Nielsen, I. B. Nielsen, S. U. Pedersen, U. V. Pedersen, and S. Tomita, “*Chromophore of the green fluorescent protein studied in the gas phase*”, Eur. Phys. J. D **20**, 597 (2002).
- [195] S. Boyé, H. Krogh, I. B. Nielsen, S. B. Nielsen, S. U. Pedersen, U. V. Pedersen, L. H. Andersen, A. F. Bell, X. He, and P. J. Tonge, “*Vibrationally resolved photoabsorption spectroscopy of red fluorescent protein chromophore anions*”, Phys. Rev. Lett. **90**, 118103 (2003).
- [196] S. B. Nielsen, J. U. Andersen, J. S. Forster, P. Hvelplund, B. Liu, U. V. Pedersen, and S. Tomita, “*Photodestruction of Adenosine 5'-monophosphate (AMP) nucleotide ions in vacuo: statistical versus nonstatistical processes*”, Phys. Rev. Lett. **91**, 048302 (2003).

Index

- abbreviations, list of, 99
acknowledgments, i–ii
adiabatic expansion, 11–13, 15, 24
afterglow, 3–4
 FALP, 4, 67, 99
 flowing afterglow, 4, 64, 66–67, 99
 stationary afterglow, 4, 64, 66–67
- Anions
 AMP⁻, 81, 82
 B⁻, 55
 B₂⁻, 42, 55
 BN⁻, 42, 55
 BO⁻, iii, 35, 36, 45–47, 54, 55, 85
 C⁻, 38, 39
 C₂⁻, 38, 42, 55
 C₃⁻, 38
 C₄⁻, 42
 Cl⁻, 30, 43–45, 47, 54, 55, 85
 CN⁻, iii, 35, 36, 42, 45–47, 54, 55, 79, 85
 D⁻, 55
 F⁻, 39, 55
 F₂⁻, 54, 55
 H⁻, 37–39
 Li⁻, 55
 NO₂⁻, 30, 41, 42, 50, 54, 56, 76, 80–82, 85, 86
 NO₃⁻, iii, 30, 51, 52, 54, 85
 O⁻, 30, 38, 39, 48, 55, 56, 85
 O₂⁻, 5, 30, 38, 43, 54, 55
 O₃⁻, iii, 9, 19, 30, 47–49, 51, 54, 56, 85, 89
 O₄⁻, 53
 OH⁻, 55
 S⁻, 43, 44, 54, 55, 85
 S₂⁻, 53
 SO₂⁻, iii, 17, 18, 30, 53, 54, 85
- Asimov, I. (1920-1992), 1
Aston, F. W. (1877-1945), 38, 59
Becquerel, A. H. (1852-1908), 75
Boersch effect, 13
Bohr, N. (1885-1962), 2
- Cations
 CO⁺, 70, 72, 73
 CO₂⁺, 8, 63–68, 72, 73, 85
 H₃⁺, iii, 62
 HCO⁺, 70
 HeH⁺, 62
 N⁺, 69, 71, 73
 N₂⁺, 72, 73
- Child's Law, 9, 80
crossed beams, 4
Curie, M. (1867-1934), 75
Curie, P. (1859-1906), 75
cyclotron frequency, 11
cyclotron motion, 10, 12, 27
- Dications
 CO²⁺, 34, 59, 60, 70–73, 86
 CO₂²⁺, iii, 34, 59, 63–65, 67, 68, 70, 72, 73, 85
 N₂²⁺, 59, 60, 68, 69, 71, 73, 85
 O₂²⁺, 59
- direct mechanism of DR, 59–62, 72
- equipartition theorem, 11, 15
- Hawking, S. W. (1942-), 1
high energy-density materials, 58
Hubble, E. P. (1889-1953), 1
- imaging detector, 19–20, 26, 83
imaging technique, 24
indirect mechanism of DR, 59, 61–62
ion sources
 Aarhus negative ion sputter source (ANIS), 27–28, 43, 45, 99
 cold cathode ion source (CCIS), 28–30, 50, 51, 53, 80, 99
 comparison, 33
 diagnostics, 33–36

- electrospray ionization (ESI), 31–33,
82, 99
- memory effect, 28, 34
- Nielsen type ion source, 31, 64, 69, 71

- Langmuir probe, 4
- longitudinal-longitudinal relaxation, 12, 13

- magnetron motion, 12, 27
- merged beams, 4–5

- Newton, I. (1642-1727), 1

- outline of thesis, iv–v
- overtaking beams, 4

- perveance, 9, 14
- Pierce shield, 8–9
- pile-up, 20
- Poisson Equation, 91
- publications, list of, iii
- pulse height spectrum, 19, 34, 43, 47, 48,
50

- Rayleigh limit, 31
- Rutherford, E. (1871-1937), 59
- Röntgen, W. K. von (1845-1923), 75

- space charge constant, 10, 15, 80
- space charge potential, 10, 25–26, 79–81,
91–93
- superimposed beams, 4

- Thomson, J. J. (1856-1940), 38, 59
- toroid contribution, 16–18, 95–96
- tunneling mechanism of DR, 62–63